DEVELOPMENT OF SUSPENSIONS FOR THE GEO 600 GRAVITATIONAL WAVE DETECTOR

Calum Iain Eachan Torrie, B.Sc.

Department of Physics and Astronomy

University of Glasgow

Presented as a thesis for the degree of Ph.D.

in the University of Glasgow

Wednesday, 17 November 1999

head *n.* Part of the body containing the eyes, nose, mouth and brain; intellect; individual person or animal.　　　(The Oxford Popular Dictionary)

'Ladies and gentlemen of the class of '99: Wear sunscreen.

If I could offer you only one tip for the future, sunscreen would be it. The long-term benefits of sunscreen have been probed by scientists, whereas the rest of my advice has no basis more reliable than my own meandering experience. I will dispense this advice now.'

Mary Smich and Baz Luhrmann, Everybody's Free (To Wear Sunscreen).

Contents

List of figures

ix

List of tables

Acknowledgements

I would first of all like to thank my supervisor Norna Robertson for the patience, help and encouragement she has given me over the last three years (especially all the afternoons spent going through the equations of motion for a triple pendulum and lately the various chapters) – thanks Norna. I would also like to thank Jim Hough for the assistance that he has given to me throughout my time as a postgraduate and for his advice when I was deciding what to do after my first degree.

My thanks also goes to Ken Strain, for answering my quick questions and to Mike Plissi, for putting up working with me in the laboratory (cheers Mike I have very much appreciated your advice and friendship).

I have studied for the last two years with Matt Husman in which time I have enjoyed reading his Sports Illustrated and our discussions on sport, ranging from US College and NFL Basketball (Stanford and Indianapolis) to Scottish football (Glasgow Rangers).

Alastair Grant also deserves big thanks for keeping me on my toes throughout the course of writing my thesis and for checking every term of every equation in chapter 4.

I also have to mention my office-mates Morag Casey (scary secretary), Sharon Twyford (sexy phone voice secretary) and lately Peter Sneddon (very poor secretary), for putting up with the huge number of phone calls I have received in the last three years. They also deserve a medal for putting up with my awful patter on a daily basis.

I would also like to mention all of the other members of the gravitational waves group here in Glasgow, namely Gavin Newton, Harry Ward, Dave Robertson, Sheila Rowan, Geppo Cagnoli, Ken Skeldon, Paul McNamara, David Clubley, David Palmer and Stephen McIntosh, as well as all of the other members of the GEO 600 collaboration, especially Benno Willke and Harald Lueck in Hannover.

Preface

This thesis is an account of the work carried out between October 1996 and October 1999 towards the development of suspensions for the GEO 600 ground based laser interferometric gravitational wave detector [1+2].

Chapter 1 contains a brief introduction to gravitational waves and an outline of the astrophysical processes that give rise to signals which should be detectable by ground based detectors. The material presented in this chapter is derived from published literature.

In chapter 2 the two main detection schemes for ground based detectors are discussed with emphasis on laser interferometric detectors. The noise sources that are expected to limit the sensitivity of such a detector are also reviewed. The German-British project, GEO 600 is discussed. The noise specification for each test mass mirror is derived and the methods used for isolating these mirrors from seismic noise are introduced. The material presented in this chapter has been obtained from published literature.

Details of the design and testing of the suspension system for auxiliary mirrors used to form the GEO 600 mode-cleaner cavities is given in Chapter 3. The work presented in this chapter was carried out by the author with Dr. Mike Plissi.

In Chapter 4 the modelling of a single pendulum is presented, including all of the geometrical effects due to gravity and the stretching of the wires, for six degrees of freedom. The comparison of the theoretical mode frequencies to those obtained from experiment is outlined. Further investigation of varying the parameters of a pendulum is carried out using the single pendulum model. The equations outlined in this chapter were derived by the author with Dr. Norna Robertson and Matt Husman.

Chapter 5 contains an outline of the extension of a single pendulum model to that of a triple pendulum. A state-space model of a triple pendulum was developed using MATLAB, by the author, to analyse the damping of the normal modes of the pendulum using active control. Details of the modelling and the mechanical design of the GEO 600 main suspension triple pendulum are given. The equations outlined

in this chapter were derived by the author with Dr. Norna Robertson and Matt Husman. The addition of the active control to the pendulum was carried out by the author with Dr. Ken Strain.

A discussion of the various experiments conducted on the prototype main suspension in Glasgow for GEO 600, including measurements of the vertical and horizontal transfer functions of the various isolation stages, is presented in Chapter 6. A description of the cantilever spring blades used in GEO 600 is given. These tests were carried out by the author with Matt Husman and Dr. Mike Plissi.

In Chapter 7 the conclusions drawn from the work presented in this thesis are given. Several suggestions of work that could, and is, being taken up for future detectors are also discussed. These discussions have arisen from meetings with Prof. Jim Hough and Dr. Ken Strain.

Appendix A contains the equations of motion of a single pendulum, outlined in Chapter 4. The use of MATLAB and state space modelling for solving the matrices produced by the coupled equations of motion followed from discussions with Matt Husman.

In Appendix B the various parameters of the Glasgow prototype suspension and the main suspension for GEO 600 are given along with two figures showing the various parameters in detail.

Appendix C includes an outline of the various input parameters, the equations of motion for all the degrees of freedom, and files which show how the local control is added to the triple pendulum. The modelling, using MATLAB, of the triple pendulum, was carried out by the author with Dr. Ken Strain and Matt Husman.

Appendix D contains a tutorial for the various pendulum files in Appendix C

Appendix E contains an investigation into the possibility of taking advantage of the improved isolation obtained at the centre of percussion of a compound pendulum. The derivations were done with Dr. Norna Robertson.

Summary

DEVELOPMENT OF SUSPENSIONS FOR THE GEO 600 GRAVITATIONAL WAVE DETECTOR

Einstein, in his 1916 Theory of General Relativity, predicted the existence of gravitational waves. These can be thought of as ripples or waves in the curvature of space-time. So far there has only been indirect evidence of the existence of gravitational waves. Scientists around the world are working on a number of gravitational wave detectors. The direct detection of gravitational waves will provide information about astrophysical processes and sources that produce them.

Gravitational waves are quadrupole in nature and produce a tidal strain in space. However their interaction with matter is very weak, making them difficult to detect. Gravitational waves emitted by violent astrophysical events are predicted to produce strains at the Earth of the order of 10^{-21} to 10^{-22} at frequencies accessible to ground based detectors (~ 10 Hz to a few kHz). One method for detecting these strains in space is based on the Michelson interferometer.

The gravitational waves group at the University of Glasgow led by Prof. J. Hough is working with collaborators from the Max-Planck-Institut für Quantenoptik at Hannover and Garching, the University of Hannover, the University of Cardiff and the Albert-Einstein-Institut at Potsdam on a project called GEO 600 to build a laser interferometer with 600 m arm length. The GEO 600 gravitational wave detector is currently in an advanced stage of construction in Germany.

The GEO 600 (German-British) detector is designed to operate down to 50 Hz. The sensitivity limit at this frequency is set by the thermal noise from the internal modes of the fused silica test masses. The strain sensitivity limit from thermal noise is expected to be $2\text{x}10^{-22}$ $\big/ \sqrt{\text{Hz}}$ at a frequency of 50 Hz. The design goal for the seismic isolation system is to achieve a noise level a factor of 10 lower than this.

To ensure that the detector sensitivity is not limited by seismic noise above 50 Hz a significant degree of isolation has to be provided for each test mass. It is expected

that this level of isolation can be obtained with a combination of several elements in series: a two-layer isolation stack consisting of one active and one passive stage, and a triple pendulum, the final stage of which is the test mass which will be made from fused silica (mass ~ 6 kg). The triple pendulum will incorporate two stages of cantilever springs in order to enhance the vertical isolation and will use fused silica fibres in the lower pendulum stage in order to minimise thermal noise from the pendulum modes.

The work contained in this thesis covers the design, modelling, construction and testing of various aspects of suspension systems for isolating optical components in ground based interferometric gravitational wave detectors, and in particular for GEO 600.

The first suspension system considered was for the subsidiary mirrors that form the mode-cleaner cavities. These take the form of high finesse Fabry-Perot cavities used to reduce the geometry perturbations of the laser beam which is used to illuminate the interferometer. The mode-cleaner optics have less stringent requirements for seismic isolation; they therefore do not require the extra vertical isolation provided by the cantilever spring stages. Further work in this thesis involved the design and testing of the various stages of this suspension system. This includes the modelling of a suitable platform from which to suspend the various optics, the construction and testing of a double pendulum, and the testing of a two-layer passive isolation stack. The various isolation stages, for the mode-cleaner, were installed at the GEO 600 site in the summer of 1999.

As stated above, for the main test mirrors a triple pendulum is required. In order to understand the mechanics of such a pendulum it was necessary firstly to model a single pendulum by calculating the equations of motion for six degrees of freedom. A theoretical model of a triple pendulum was obtained, again by writing down the equations of motion. MATLAB was used to predict, for example, the resonant mode frequencies, and the response of the triple pendulum to the application of control for active damping. Using this analysis the design of a well-damped triple pendulum with good coupling between the various stages can be achieved.

A prototype triple pendulum was set-up in Glasgow in order to verify the predictions from the model. Further experiments on the individual stages of the overall suspension system in Glasgow, including the testing of the cantilever blades, indicated that a seismic noise level which is a factor of ~ 4 lower than the thermal noise level at 50 Hz should be achievable with the current design. At the time of writing the main suspension systems were beginning to be installed in the GEO 600 detector.

Chapter 1

The Nature, Sources and Detection of Gravitational Waves.

1.1 Introduction

Einstein, in his 1916 Theory of General Relativity [3], predicted the existence of gravitational waves. The solutions to the linearised Einstein Field Equations show that the effect of gravity propagates as a wave at the speed of light. However it was not until the 1960's that the world-wide interest in detecting gravitational waves started, as a result of the suggestion by Weber that they could be detected and his subsequent experimental work he carried out [4].

In 1993 Hulse [5] and Taylor [6] were awarded the Nobel Prize for Physics for their discovery of the binary pulsar PSR 1913+16 and subsequent observations of the orbit, providing indirect evidence of the existence of gravitational waves. These observations showed that the orbital period was decreasing with time. Using a model based on Einsteins Theory of General Relativity they showed that this decrease in orbital period would be accounted for if the energy loss was attributed to gravitational waves.

Today there are a number of collaborations around the world working towards the challenging goal of the direct detection of gravitational waves. The detection of gravitational waves is important for several reasons. Firstly it will allow some of the predictions of General Relativity to be tested. Secondly it will provide new information on astrophysical events in the universe, for example, the collapse of stars

and the birth and interactions of black holes, thereby generating a whole new field of astronomy.

The nature (section 1.2) and sources (section 1.3) of gravitational waves will be described briefly. The various methods for detecting gravitational waves are discussed (section 1.4). In particular, an overview of ground based laser interferometric gravitational wave detectors is given. There are a number of noise sources that limit the possible sensitivity of such detectors. These are considered in section 1.5.

1.2 The Nature of Gravitational Waves

What are gravitational waves? In order to answer this question it is useful to compare them to electromagnetic waves. Electromagnetic waves are produced by the acceleration of charge whereas gravitational waves are produced by the acceleration of mass.

The conservation of energy and therefore mass, for gravity, is equivalent to conservation of charge in electromagnetism. This implies that there can be no monopole gravitational radiation. Further because of conservation of momentum there can be no dipole gravitational radiation. The lowest order of gravitational radiation must be therefore quadrupole in nature, implying that only non-axisymmetric accelerations of mass will produce gravitational waves.

Gravitational waves produce ripples or waves in the curvature of space-time. Thus they can be considered as a tidal strain in space. The waves, arriving at the Earth from a distant source, can be split into two independent polarisations h_+ and h_x. The effect of the strain on a ring of test particles of diameter L is shown, for both polarisations, in figure (1.1). If the wave is incident perpendicular to the plane of the page the ring of particles is stretched in one direction by an amount ΔL and compressed in the other direction by ΔL. A suitably polarised gravitational wave of amplitude h will produce a strain given by

$$h = \frac{2\Delta L}{L}.$$
(1.1)

Gravity is the weakest of the four forces of nature. The effect of a gravitational wave is, therefore, only significant when very large masses and accelerations are considered i.e. on an astrophysical scale.
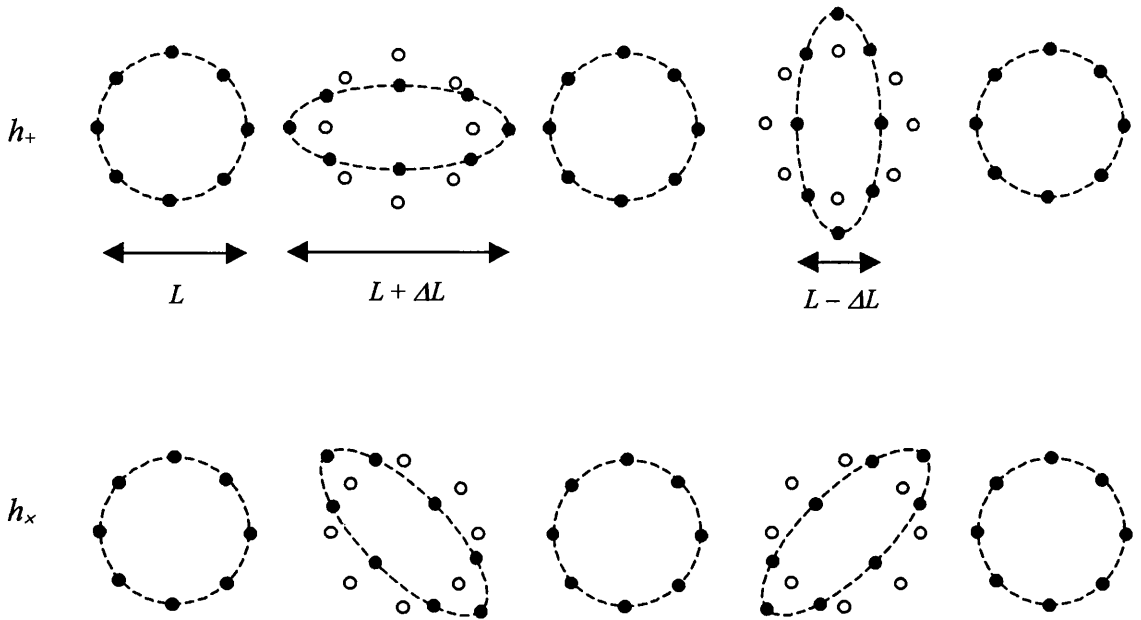
Figure (1.1): - *The effect of one cycle of a gravitational wave on a ring of test particles, the wave is incident at right angles to the plane of the page.*

1.3 Sources of Gravitational Waves

1.3.1 Introduction

Gravitational waves in the frequency range of a few tens of Hz to a few kHz are expected to be detected by ground based gravitational wave detectors. The frequency range given is limited due to various noise sources, as discussed later. Possible sources of waves in this frequency range are summarised in the following sections.

1.3.2 Burst sources

Supernovae

The rapid brightening of a star, to ~ 1 billion times the luminosity of the sun, followed by its gradual decay is one of the most striking events to occur in the sky.

Supernovae can be classified as either Type I or Type II supernovae [7]. Type I supernovae are thought to occur when a white dwarf in a binary system has gained enough mass from its companion to exceed the Chandrasekhar limit ($M_{Ch} = 1.4M_\odot \approx 3\times10^{30}$ kg) and cause the white dwarf to collapse, triggering a stellar explosion. Type II supernovae are thought to occur when the iron core of a massive star collapses triggering a stellar explosion. If the collapse is perfectly symmetrical no gravitational waves will be produced. However if the collapse is asymmetric, due to a significant amount of angular momentum in the core of the star, then there is a possibility that strong gravitational waves will be produced.

Schutz [8] approximates the strain amplitude, h, expected from supernovae as

$$h \approx 5 \times 10^{-22} \left(\frac{E}{10^{-3}M_\odot c^2} \right)^{\frac{1}{2}} \left(\frac{15 \text{ Mpc}}{r} \right) \left(\frac{1 \text{ kHz}}{f} \right) \left(\frac{1 \text{ ms}}{\tau} \right)^{\frac{1}{2}}, \qquad (1.2)$$

where E is the total energy radiated, $M_\odot$ is the mass of the sun, c is the speed of light, f is the frequency of the gravitational signal, τ is the time taken for the collapse to occur and r is the distance to the source.

The event rate for both Type I and Type II supernovae, out to the VIRGO cluster at a distance of ~ 15 Mpc, has been estimated as several per month [9].

Coalescing binaries

A compact binary system consists of two high-density stars (neutron stars or black holes) rotating about their common centre of mass. As already mentioned for the case of PSR 1913+16, the orbital period of a compact binary system decays as the system inspirals due to a loss of energy in the form of gravitational waves. As the two stars approach each other the amplitude and the frequency of the emitted gravitational

waves increase. A few seconds before the two stars coalesce the amplitude and frequency reach values that are expected to be observable by ground based detectors.

Schutz [10] approximates the strain amplitude, h, expected from coalescing neutron stars as

$$h \approx 1 \times 10^{-23} \left(\frac{100 \text{ Mpc}}{r} \right) \left(\frac{M_b}{1.2M_\odot} \right)^{\frac{5}{3}} \left(\frac{f}{200 \text{ Hz}} \right)^{\frac{2}{3}}, \qquad (1.3)$$

where $M_b = (M_1 M_2)^{3/5} / (M_1 + M_2)^{1/5}$ is the mass parameter of the binary, M_1 and M_2 are the masses of the two stars and the other symbols are as defined for equation (1.2). The timescale, τ, over which the frequency changes is [10]

$$\tau \approx \left(\frac{1.2M_\odot}{M_b} \right)^{\frac{5}{3}} \left(\frac{200 \text{ Hz}}{f} \right)^{\frac{8}{3}}. \qquad (1.4)$$

Schutz has shown that the product of h and τ is independent of mass. If h, f and τ are detected by several detectors then both the distance and position of the source can be obtained. The accuracy will depend on the number of detectors and their respective sensitivities and signal to noise ratios.

Of the hundreds of pulsars now known, a few are located in binary systems. The number of pulsars existing in binary systems along with the estimated pulsar birth rate can be used to estimate the event rate of coalescing binary systems; an event rate of 3 per year out to 200 Mpc is implied [11].

1.3.3 Periodic sources

Rotating neutron stars and white dwarfs are possible sources of continuous periodic gravitational waves. A single detector can detect such a source. For the case of an interferometer the sensitivity can be increased, once the frequency of the source is known, by using signal recycling to reduce the bandwidth of the detector (see section 2.2.2). Some possible sources of continuous periodic gravitational waves, detectable by ground based detectors, are outlined below.

Pulsars

The spin of a pulsar must be non-axisymmetric for it to emit gravitational waves. A typical pulsar emits gravitational waves at twice its rotational frequency, f_{rot}. An estimate of the likely amplitude from a such a source is [12]

$$h \approx 6 \times 10^{-25} \left(\frac{f_{rot}}{500 \text{ Hz}}\right)^2 \left(\frac{1 \text{ kpc}}{r}\right) \left(\frac{\varepsilon}{10^{-6}}\right), \qquad (1.5)$$

where ε, the equatorial ellipticity, is a measure of how non-symmetrical the star is.

The Crab pulsar is expected to be emitting gravitational waves at ≈ 60 Hz. An upper limit of the signal from the Crab Pulsar of $h \sim 10^{-24}$ is calculated for a $\varepsilon \approx 7 \times 10^{-4}$, $r \approx 1.8$ kpc and $f_{rot} = 30$ Hz [12].

Wagoner stars

If as a result of accretion a neutron star with high angular momentum reaches the Chandrasekhar-Friedman-Schutz instability point, the neutron star will become non-axisymmetric and produce gravitational waves [13]. Due to the fact that the rate of accretion of angular momentum is proportional to the rate of accretion of mass, the gravitational wave luminosity is therefore proportional to its X-ray luminosity. Recent discoveries by the Rossi X-ray timing Explorer [14] suggest that the gravitational wave signal strength of the X-ray source SCO X-1 could be $h \sim 2 \times 10^{-26}$ at 500 Hz, at the surface of the Earth.

1.3.4 Stochastic sources

It is expected that a random background of gravitational waves will exist, as a result of the superposition of signals from many sources. This may contain information about processes connected with the creation of the Universe. One possible prediction of background radiation, from the cosmic string scenario for galaxy formation, produces an amplitude given by [15]

$$h \approx 2.4 \times 10^{-25} \left(\frac{H_o}{75 \text{ kms}^{-1} \text{ Mpc}^{-1}}\right) \left(\frac{\Omega_{gw}}{10^{-8}}\right)^{\frac{1}{2}} \left(\frac{f}{100 \text{ Hz}}\right)^{-\frac{3}{2}} \left(\frac{B}{2 \text{ Hz}}\right)^{\frac{1}{2}} \qquad (1.6)$$

in a bandwidth B about a frequency f where Ω_{gw} is the energy density per logarithmic frequency interval required to close the Universe and H_o is the present value of Hubble's Constant.

The stochastic background will be difficult to distinguish from other sources of Gaussian noise in one detector. However it will be identical in two different detectors. Therefore, by cross-correlating the data from several detectors, it should be possible to separate the stochastic background from the random noise associated with each detector.

For periodic sources such as pulsars and Wagoner stars and for stochastic sources the signal to noise ratio can be increased by integrating over a long observation time. For example consider a detector with a sensitivity limit of $10^{-22}/\sqrt{\text{Hz}}$ at 100 Hz. After an integration time of 10^7 seconds, ~ 1 year, the equivalent sensitivity level would be $\sim 3 \times 10^{-26}$.

1.4 Gravitational Wave Detectors

In order to detect gravitational waves it is necessary to measure extremely small strains, h, produced in space by the wave. There are two types of ground based detectors currently being developed: -

- resonant bar detectors (section 1.4.1) and

- laser interferometers (section 1.4.2).

As already mentioned ground based detectors are designed to operate in the frequency range from a few tens of hertz to a few kilohertz.

If a laser interferometer is put into space, it is possible to detect gravitational waves at lower frequencies (section 1.4.3).

Other methods of detecting gravitational waves include the Doppler tracking of spacecraft and pulsar timing. The relative separation of the Earth and a spacecraft will be affected by a passing gravitational wave. This could be detected from the Doppler

shift in the frequency of the radio signals used to follow the spacecraft. The CASSINI mission to Saturn could measure a signal of amplitude $h \sim 5 \times 10^{-17}$ at 2×10^3 Hz from December 2001 [16]. Pulsar timing is similar to the Doppler tracking of a spacecraft, except that it is the radio signals from the pulsar that are used [17]. This technique is sensitive down to frequencies of the order $\sim 10^{-8}$ Hz.

1.4.1 Resonant bar detectors

The original bar detector was developed by Weber [4] in the 1960's. Such a detector consists of a large cylinder, typically with a mass of several tonnes. If a gravitational wave of the same frequency as the fundamental longitudinal mode of the cylinder (typically ~ 1 kHz) is incident on such a detector it will cause the cylinder to vibrate, inducing a mechanical strain which can be measured using a transducer and amplifier. The signal will be proportional to the gravitational wave amplitude.

The effects of seismic and acoustic noise are reduced on a resonant bar detector by suspending the cylinder from vibration isolation stages and placing the bar under vacuum. The sensitivity is then limited by both the thermal noise of the cylinder and the noise from the sensors. A reduction in the level of thermal noise is achieved by cooling the detector to temperatures of a few Kelvin and by constructing the cylinder from a material of low loss, or high quality factor, Q, at low temperatures typically aluminium or niobium. Using a material with a high Q also ensures that once the cylinder is excited it will continue to oscillate for long time, which has the effect of increasing the bar's sensitivity.

Resonant bar detectors have been developed by groups in Stanford, Louisiana State University (ALLEGRO), Rome (NAUTILUS), CERN (EXPLORER), Padua (AURIGA) and Perth, Western Australia (NIOBE). Strain sensitivities of $h \approx 6 \times 10^{-19}$ at ~ 1 kHz [18] at temperatures of ~ 4 K have been achieved. Recently, groups in Italy and the USA have developed techniques to improve the strain sensitivity by cooling the bars down to temperatures of ~ 50 mK [19+20]. A further increase in the sensitivity of a resonant bar detector can be achieved by increasing the mass of the detector and one way of doing this is by using a 'spherical' bar. Firstly a 'spherical' bar is more massive than a cylindrical bar of the same resonant frequency and,

therefore, the effect of thermal noise is reduced. Secondly a sphere has five usable quadrupole modes compared to one in a bar (essentially producing five detectors from one). As a gravitational wave passes through the bar the ratio of the amplitudes of the five modes can be used to determine the direction and polarisation of the wave. There have been several proposals for such detectors; currently there is one, called MiniGRAIL, seeking funding in Leiden in Holland [21].

1.4.2 Ground-based laser interferometric gravitational wave detector

A simple laser interferometer detector is, in principle, a Michelson interferometer whose mirrors are suspended as pendulums. The first work on laser interferometers was done by Forward [22] and by Weiss [23] in the 1970's.

An outline of a Michelson interferometer is shown in figure (1.2). Light from a laser is incident on a beamsplitter where the light beam is partially reflected and partially transmitted into the two arms each of length L. The light is then reflected from a mirror at the end of each arm back to the beamsplitter. The combined interference pattern is then detected at the photodetector. A gravitational wave would cause a change in the intensity of this interference pattern due to the relative motion of the mirrors. The mirrors are suspended as pendulums under vacuum to isolate them from noise sources such as ground vibrations or air pressure fluctuations.
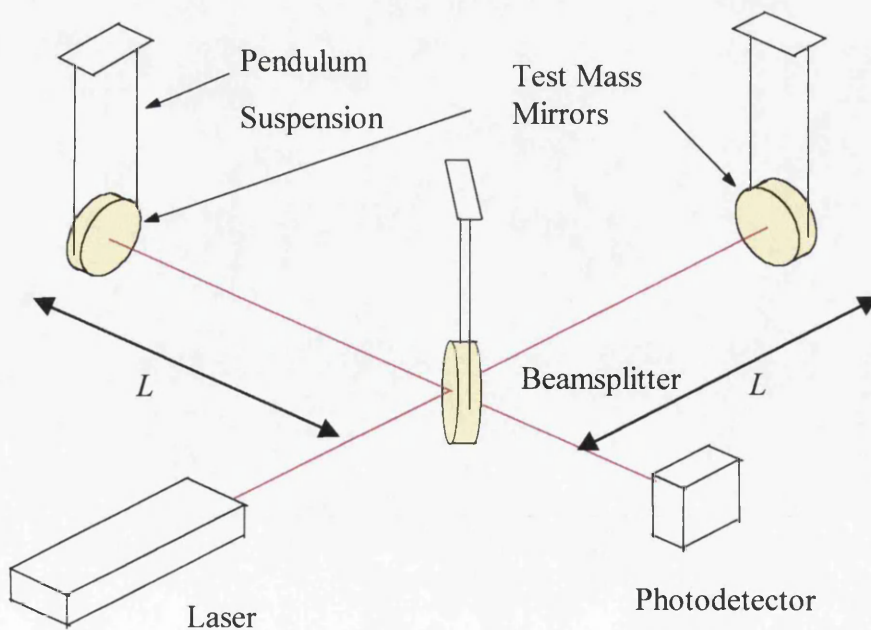
Figure (1.2): - *Diagram of a simple Michelson interferometer.*

The effect of a gravitational wave on a ring of particles is shown in figure (1.1). The orthogonal arms of a Michelson interferometer therefore provide an ideal set-up for detecting the differential change in length caused by the quadrupole nature of gravitational waves. For example, a wave of amplitude $\frac{\Delta L}{L}$ propagating in a direction perpendicular to the plane of the arms of the detector will cause one of the arms to be stretched by an amount ΔL and at the same time cause the other arm to be compressed by ΔL. The result is a differential change in arm length of $2\Delta L$.

As the arm length, L, is increased so too does the relative size of ΔL and this, in turn, produces a more sensitive detector, so long as the other noise sources are not also increased. It can be shown that, if the sensitivity is limited by the statistical fluctuations in the number of photons detected, the maximum sensitivity is achieved when the light is stored in the arms for approximately half the period of the gravitational wave [24]. A gravitational wave of frequency 1 kHz corresponds to an arm length, $L = \frac{\lambda_{gw}}{4} \sim 75\,\text{km}$ [24]. Unfortunately it is impractical to build an interferometer on Earth with an arm length of more than ~ 4 km.

It is possible, however, to increase the distance that the light travels by making it travel up and down the arms of the interferometer several times. This effectively increases the arm length and, hence, the storage time of the cavity. The storage time is average time the light spends in the arms of the interferometer. This effective increase in arm length can be achieved using: -

- a delay line or

- a Fabry-Perot cavity.

The delay line interferometer

The delay line interferometer was first proposed by Weiss [23] in the early 1970's. The optical path length in a delay line interferometer is increased by the use of multiple non-overlapping beams that are reflected between two curved mirrors. Each delay line cavity is illuminated via a hole in the mirror close to the beamsplitter. In an

arrangement, such as that developed by the group at the Max-Planck-Institut für Quantenoptik, Garching, Germany [25], the light exits the delay line by the same hole. A simplified schematic diagram of this delay line interferometer is shown in figure (1.3). The strain sensitivity achieved in the 30 m delay line prototype interferometer at Garching was $h \sim 1 \times 10^{-19} \mathrm{m}/\sqrt{\mathrm{Hz}}$ above 1.5 kHz achieved in 1988 [26].
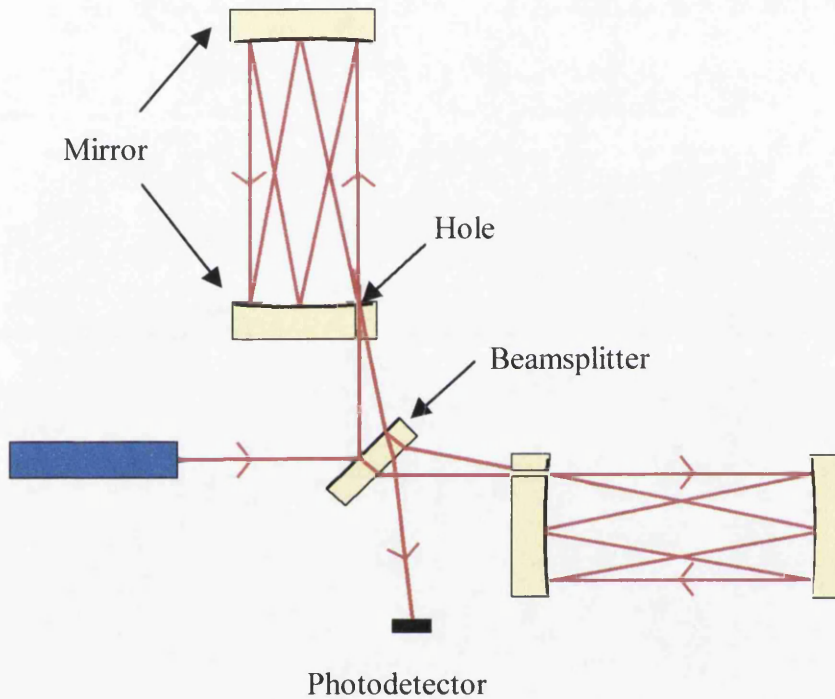
Figure (1.3): - *Schematic of a delay-line interferometer.*

Fabry-Perot interferometer

This method of increasing the storage time inside the interferometer was first developed in Glasgow [27] in the early 1980's. Two Fabry-Perot cavities are built into the arms of the interferometer, as shown in figure (1.4). Each cavity consists of one partially and one fully reflecting mirror, with the reflected beams lying on top of each other.

The cavity is said to be on resonance, and the amount of energy in the cavity is a maximum, if the length of the cavity, L, is tuned to fit an integral number of half wavelengths of the laser light. The cavity is held on resonance using servo control and

under these conditions the differential displacement is increased by a factor F/π where $F = \dfrac{c\pi\tau}{L}$ is the finesse of the cavity and τ is the storage time.

The main advantages of a Fabry-Perot interferometer compared to a delay line interferometer are that it is possible to use much smaller mirrors for operation, since the multiple beams overlap one another, and that the effect of scattered light within the interferometer arms is reduced [25]. The main disadvantage however is the need to obtain and maintain resonance [28].

The strain sensitivity achieved in the kilohertz region by the prototype Fabry-Perot detectors in Glasgow (10 m) is of the order of a few times 10^{-18} [29+30] and Caltech (40 m) is of the order of 10^{-19} for wideband bursts [31].
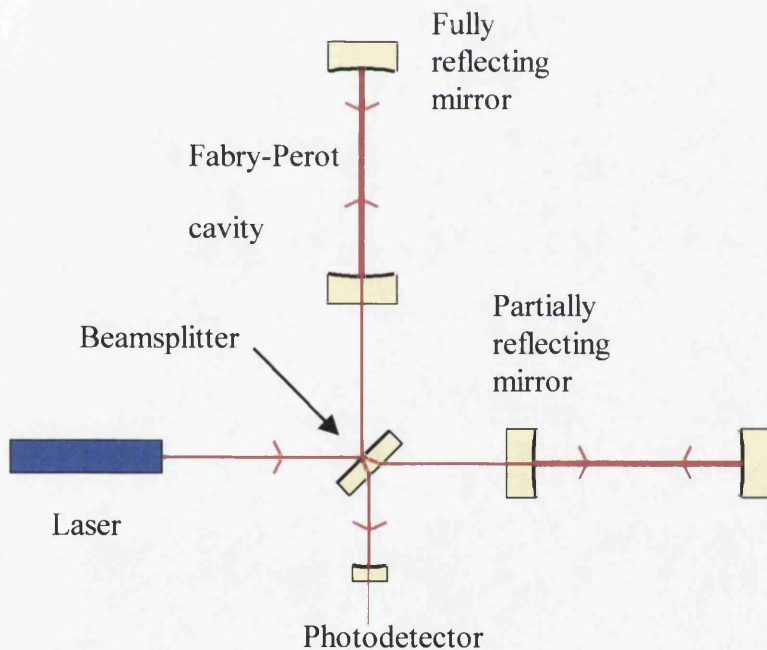
Figure (1.4): - *Schematic of a Fabry-Perot interferometer.*

Laser interferometers around the world

There are several interferometric gravitational wave detectors in advanced stages of construction around the world. LIGO [32] is a project in the USA to build two 4 km detectors one at a site in Livingston, Louisiana and one at Hanford in Washington State. A French-Italian collaboration, VIRGO [33], is constructing a 3 km detector near Pisa in Italy. The Japanese are constructing a 300 m detector , TAMA 300 [34], near Tokyo and they also have plans to build a 3 km detector in a disused mine under a mountain range [35] near Tokyo. AIGO [36] is a proposed Australian project not yet funded, to build a detector at a site near Perth in Western Australia. Initially it would have an arm length of a few hundred meters although these could be extended up to as much as 5 km. The Gravitational Waves Group at the University of Glasgow is collaborating in GEO 600 [1], a joint German-British project with 600 m arms. GEO 600 is in an advanced stage of construction at a site near Hanover in Germany.

1.4.3 Space-borne detectors

LISA (Laser Interferometer Space Antenna) [37] is a space-borne Michelson Interferometer that will observe gravitational waves in the frequency range of 0.1 mHz to 1 Hz. Space-borne detectors have the advantage of not being limited by noise sources which affect ground based detectors at low frequency. Typical sources of gravitational waves are, for example, from interactions of massive black holes and from binary systems with large separations [38]. LISA has been proposed as a cornerstone mission in the Post Horizon 2000 programme in ESA. It will consist of three identical spacecraft positioned in orbit 20° behind the Earth, with the three spacecraft, separated by a distance of 5×10^9 m, forming an equilateral triangle. Each spacecraft contains a test mass and laser transponder (Nd:YAG) allowing the sides of the triangle to form two semi-independent interferometers. A gravitational wave strain sensitivity of $h \sim 10^{-21}/\sqrt{Hz}$ at 0.1 mHz is expected to be achieved. ESA/NASA are currently discussing a joint mission to launch LISA in ~ 2008.

Space-borne detectors will be complementary to ground-based detectors and, as already stated, will extend the frequency range for observations of gravitational waves.

1.5 Noise Sources

The main noise sources that may degrade the sensitivity of ground based laser interferometric gravitational wave detectors are: -

- photon noise

- thermal noise, in the mirror test masses and their suspensions.

- seismic noise due to motions of the Earth.

1.5.1   Photon noise

Photon noise, or photon shot noise, is the statistical fluctuation in the number of photons detected at the output of an interferometer. The signal detected at the output of the interferometer due to N photons will have a $\sqrt{N}$ uncertainty associated with it due to Poisson counting statistics. This uncertainty gives rise to noise at the photodetector that will limit the sensitivity of the detector due to the fact that it is the output intensity that is used to measure the gravitational wave amplitude. For a delay-line the shot noise sensitivity is given as [39]

$$h_{\text{shot}}(f) = \left(\frac{h\lambda}{2\varepsilon I_o c} \right)^{\frac{1}{2}} \frac{f}{\sin(\pi f \tau)} \, \frac{1}{\sqrt{\text{Hz}}}, \tag{1.7}$$

where h is Planck's constant, λ is the light wavelength and ε is the photodetector quantum efficiency. The input power is I_o while c is the speed of light, and τ is the light storage time. From equation (1.7) it can be seen that the shot noise can be minimised by setting the storage time equal to half of the period of the gravitational wave, i.e. $f\tau = \frac{1}{2}$. Furthermore it can be seen that the shot noise sensitivity can be improved by increasing the level of input power. However as the laser power is increased the radiation pressure noise, caused by fluctuations in the number of photons reflecting off the surface of the test mass, is also increased. When the input laser power is optimised, the shot noise equals the effect of radiation pressure noise at a particular frequency. Under these conditions a fundamental noise floor is reached,

the quantum limit [24÷40]. For the interferometers currently under construction (section 1.4.2) the quantum limit is well below other noise sources.

1.5.2 Thermal noise

The random motion of the atoms of the test mass mirrors and their suspensions, which are at a finite temperature and have a number of resonant modes, generates thermal noise. The magnitude of the thermal noise depends on Boltzmann's constant, k_B, and the temperature, T, of the atoms. The sources of thermal noise include the pendulum modes of the suspended test masses, the violin modes of the suspension wires and the internal modes of the test masses. For each mode it is possible to assign $k_B T$ of thermal energy, integrated over all frequencies. However it is the shape of the thermal noise spectrum as a function of frequency that is important in this application. This can be derived using the complex form of Hooke's Law [41]

$$F = - k[1 + i\phi(\omega)]x \tag{1.7}$$

where the imaginary term $\phi(\omega)$ is the phase by which the displacement x lags the applied force F. The quality factor Q of a resonance (where Q is a measure of how small the dissipation is at the resonant frequency) is related to ϕ by $Q = 1/\phi(\omega_o)$ where ω_o is the angular resonant frequency. It is possible to show, using the fluctuation-dissipation theorem, that the power spectral density of thermal motion for a mass, m is given by [41]

$$\tilde{x}^2(\omega) = \frac{4k_B T \omega_o^2 \phi(\omega)}{\omega m[(\omega_o^2 - \omega^2)^2 + \omega_o^4 \phi(\omega)^2]} \tag{1.8}$$

where $\omega_o^2 = k/m$. The maximum thermal motion occurs at the resonant frequency. By designing low loss, high Q suspensions and using high Q materials, it is possible to ensure that the off resonance thermal noise is kept to a minimum. The methods used to minimise thermal noise for the GEO 600 detector are discussed in more detail in section 2.3.

1.5.3 Seismic noise

Seismic noise results from natural phenomena such as ocean waves as well as from artificial effects such as traffic and machinery. The level of seismic noise varies throughout the world and also throughout the day. An approximate seismic noise spectrum of $\left[\dfrac{10^{-7}}{f^2}\right]$ $m/\sqrt{Hz}$, in both the horizontal and vertical directions, has been measured from 20 to 300 Hz [42] at the GEO 600 site near Hanover. Each mirror must be isolated from the seismic motion of the ground over the range of frequencies in which the detector operates. How this is achieved is discussed in section 2.6.

1.5.4 Other noise sources

Gravity gradient noise is a result of the direct coupling of seismic motion to the test masses by, for example, the motion of an isolated body in the vicinity of the detector [43+44]. Vibration isolation systems, such as discussed in section 2.5, cannot reduce the effects of gravity gradient noise as it effectively short-circuits the isolation systems. The noise spectrum resulting from gravity gradient noise is negligible compared to that of the sensitivity of the initial long base-line detectors [43+44] and will therefore not have any observable affect. However as seismic isolation designs improve and other noise sources are reduced, interferometers could be limited by gravity gradient noise at frequencies below ~ 10 Hz.

Associated with the laser are a number of noise sources which must be controlled to reduce their effects to levels that are negligible. Firstly, frequency fluctuations in the laser light can be stabilised by locking the laser frequency to one of the arms of the detectors. Secondly, operating the detector on a dark fringe reduces the effects of intensity fluctuations of the laser. Finally, a mode-cleaning cavity can be used to reduce the geometry perturbations of the laser beam.

In order for the detector to operate there must be control systems that operate at all times. For example, local control systems are used to damp the various modes of the pendulums. It is therefore necessary to ensure that the control noise does not itself induce significant motions in the test mass mirrors.

1.6 Conclusions

Einstein predicted the existence of gravitational waves. Hulse and Taylor have already obtained indirect evidence of their existence. The direct observation of gravitational waves still remains one of the challenging goals of modern day physics. It can be concluded from the theoretical estimates that detectors should aim for a strain sensitivity in the region 10^{-21} to 10^{-22} or better in a bandwidth of several hundred Hz in order to detect gravitational waves on Earth.

There are two types of gravitational wave detectors

- resonant bar detectors and
- laser interferometers.

Laser interferometers are broadband while resonant mass detectors are inherently narrow band in frequency. There are several interferometers currently under construction throughout the world. The University of Glasgow is working in collaboration with others on the GEO 600 detector [2]. This is the topic of chapter 2.

Chapter 2

The German-British Project, GEO 600

2.1 Introduction

GEO 600 is a German-British project to build a 600 m arm length gravitational wave interferometer. A basic description of the interferometer is given and the optical techniques of power and signal recycling are discussed in section 2.2.

The design sensitivity of GEO 600 is based on the assumption that at 50 Hz the dominant noise source will be thermal noise associated with the combined losses of the internal modes of the fused silica test masses [45+46]. A summary of the aspects of thermal noise affecting the test masses and their suspensions is given in section 2.3.

The work contained in this thesis covers various methods of reducing the levels of seismic noise. Seismic noise is one of the most important noise sources that will affect the performance of the detector. In order to isolate against seismic noise it is necessary to design suitable isolation systems. An introduction to seismic isolation is given in section 2.4, and this is followed by a more detailed consideration of the isolation required for GEO 600 (section 2.5) and how this is achieved (section 2.6). A brief consideration of alternative isolation systems is given in section 2.7 The overall sensitivity limit of GEO 600 is presented in section 2.8.

2.2 GEO 600

2.2.1 Basic outline

GEO 600 [1] is a joint German-British project in an advanced stage of construction at a site near Hanover in Germany. The collaboration involves groups from the Max-Planck-Institut für Quantenoptik at Hanover and Garching, the University of Hanover, the University of Glasgow, the University of Cardiff, and the Albert-Einstein-Institut at Potsdam.

The GEO 600 system uses a four-pass Michelson interferometer of arm length 600 m to sense the relative displacements of the test mass mirrors, as shown in figure (2.1). The input laser power of ~ 5 W will be provided by a diode pumped Nd:YAG laser. A mode-cleaner cavity can be used to reduce the geometry perturbations of the laser beam. In GEO 600 two triangular mode-cleaner cavities [47], a simple schematic of which is shown in figure (2.2), are placed in front of the interferometer. A mode-cleaner is a spatial filter designed to pass a pure stable Gaussian mode.

The whole system is entirely closed within a vacuum system. In order to keep the noise from refractive index fluctuations below other noise limits, the target vacuum is $\sim 5 \times 10^{-8}$ mbar for H_2 and 5×10^{-9} mbar for other gases. In order to prevent contamination of the optics from the out-gassing of hydrocarbons all of the materials exposed to the vacuum will be made either from metal, PTFE or ceramic.

In order that the sensitivity of GEO 600 is competitive with that of the 1st stage LIGO and VIRGO detectors, the limitations set by the smaller budget and shorter arm-length of GEO 600 must be overcome.

Test mass mirror

Test mass mirror

Input laser (after
mode-cleaners)

600 m

Compensator

Beamsplitter

Power
recycling
mirror

Test mass mirror

Test mass mirror

Signal recycling mirror

Photodiode
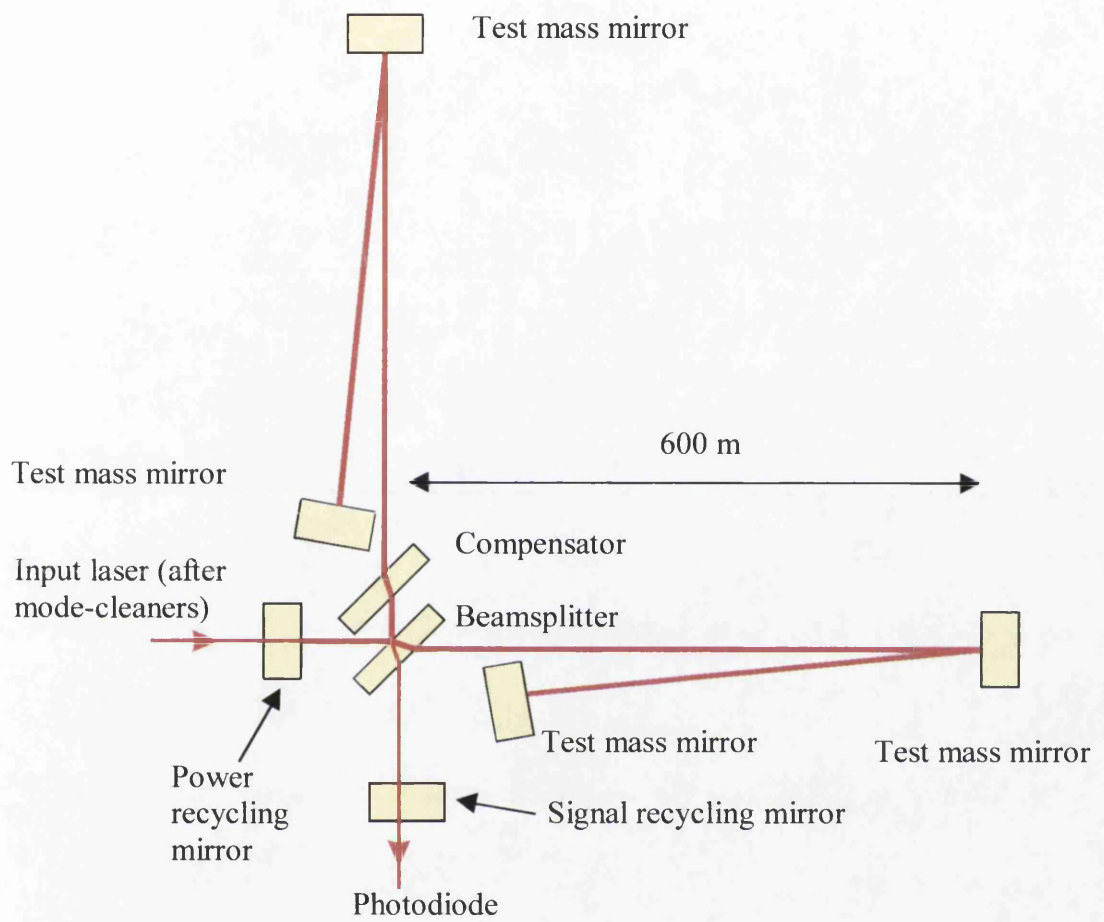
Figure (2.1): - *GEO 600 optical layout.*
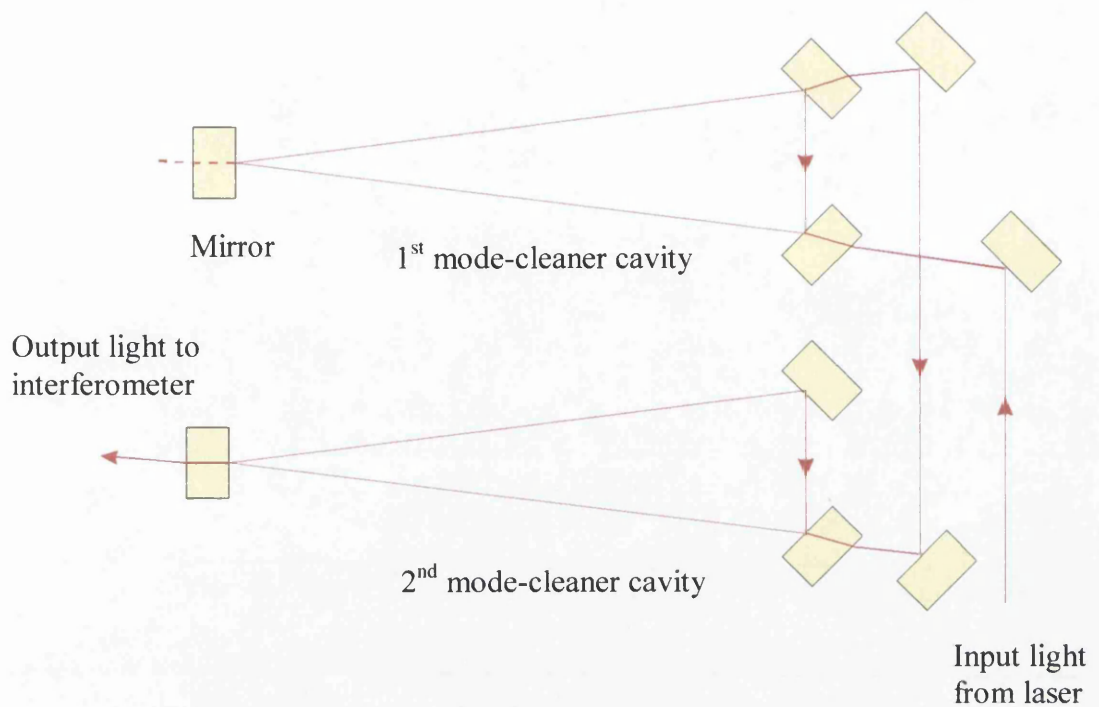
Figure (2.2): - *GEO 600 mode-cleaner layout.*

This is achieved by: -

- using the optical techniques of power recycling [48] and signal recycling [49],

- minimising the thermal noise in the mirror test masses and their suspensions by using all fused silica mirrors and suspensions [50+51].

2.2.2 Power and signal recycling

As already mentioned, the shot noise can be reduced if the input power is increased. When the interferometer is locked on a dark fringe, all of the light coming back from the arms of the interferometer is returned to the laser whilst the side-bands are emitted at the output. An additional partially reflecting mirror, the power recycling mirror, is positioned between the laser and the beamsplitter as shown in figure (2.1) and reflects most of the light back into the interferometer [48]. The mirror forms a cavity resonating at the frequency of the light, f_{light} between the mirror and the interferometer. The optical power is therefore increased and the effect is equivalent

to using a more powerful laser. A power recycling factor ~ 2000 is to be used in GEO 600 compared to a factor of ~ 30 in LIGO.

When implementing signal recycling, a partially reflecting mirror is placed at the output of the interferometer, as shown in figure (2.1). The signal recycling mirror forms a resonant cavity at the frequencies $f_{light} + f_{sig}$ or $f_{light} - f_{sig}$, where f_{sig} is the signal frequency. The sensitivity of the detector is therefore resonantly enhanced at a particular frequency [49], as shown in figure (2.6). For this reason signal recycling will be used to tune to gravitational waves from continuous sources.

2.3 Thermal Noise Aspects

The design sensitivity of GEO 600 is based on the assumption that between approximately 50 Hz and 200 Hz the dominant noise source will be thermal noise associated with the combined losses of the internal modes of the fused silica test masses. Taking a value for the loss of fused silica as $\phi = 2 \times 10^{-7}$ the resultant motion of each mirror is calculated to be approximately 7×10^{-20} m$/\sqrt{\text{Hz}}$ at 50 Hz. For our optical system it can be shown that this gives a strain sensitivity limit of 2×10^{-22} $/\sqrt{\text{Hz}}$ at a frequency, f, of 50 Hz [45,46]. For this to be the dominant noise source, the contribution to the motion of each test mass from the thermal noise of the pendulum suspension is required to be below the above noise level. It can be shown that a loss factor for the pendulum mode of the last stage of the pendulum suspension of $< 1.4 \times 10^{-7}$ at 50 Hz is thus required [52].

The loss factor of the pendulum mode of each suspension $\phi_{pend}(\omega)$ is related to the loss factor of the material of the suspension fibres $\phi_{mat}(\omega)$, by [51]: -

$$\frac{1}{\phi_{\text{pend}}(\omega)} = \frac{1}{\phi_{\text{mat}}(\omega)} \frac{mgl}{4\sqrt{TEI}} \qquad (2.1)$$

where m is the mass of the pendulum, l is the length of pendulum, T is the tension in each suspension fibre, $\omega = 2\pi f$ is the angular frequency, E is the Young's modulus of the fibre material and I is the bending moment of each fibre, ($I = \pi r^4/4$ for

cylindrical fibres of radius r). For the final stage of the main suspension for GEO 600 $\phi_{pend}(\omega) \approx \phi_{mat}(\omega)/150$.

Thus to achieve the necessary low level of pendulum loss factor it is desirable to choose, for the suspension fibres, a material with a suitably low loss factor. Experiments [53,54] indicate that fused silica has a low intrinsic material loss. Measurements performed on fused silica ribbons and fibres produced in the laboratory in Glasgow, by Dr. Sheila Rowan and Dr. Sharon Twyford, show that, in the frequency range between 6 and 160 Hz, material loss factors of the order of 10^{-6} may be repeatably achieved [51].

At the time of writing loss factors for the pendulum mode of the order of ~10^{-8} for a 500g mass [50] and 4 x 10^{-8} on a 3kg mass [55] have been obtained. The latter measurements were carried out with colleagues at the University of Perugia.

Given the low levels of mechanical loss required, it is essential that the fused silica suspension fibres are jointed to the fused silica test masses in a manner which does not add any excess loss to that associated with the pendulum mode of each suspension or with internal modes of the test masses. In the GEO 600 main suspension fused-silica test masses will be suspended from four vertical fused-silica fibres. The fibres are welded on to fused-silica prisms that are hydroxy-catalysis bonded to flat areas polished to the sides of the masses.

Initial measurements [56] suggest that the loss factors of the internal modes of a GEO 600 test mass with fibres welded to it using this technique over an appropriate bond area, would be negligibly degraded by the bonding.

LIGO will initially use steel wires to suspend the test masses, resulting in higher thermal noise. VIRGO are now hoping to adopt a similar suspension to that of the GEO 600 design to suspend their test mass mirrors.

2.4 Seismic Isolation – Introduction to Techniques

Seismic noise is one of the most important noise sources that will affect the detector at low frequencies. Therefore it is necessary to design adequate isolation systems.

A pendulum suspension is one of the simplest of isolation systems. Consider a point mass, m, suspended on a wire of length, l, with negligible mass. The horizontal transfer function between the displacement of the point of suspension, x_0, and the displacement of the mass, x_1, can be shown to be

$$\frac{x_1}{x_0} = \frac{\omega_0^2}{s^2 + \omega_0^2} , \qquad (2.2)$$

assuming no damping and using the Laplace transforms $\dot{x} \rightarrow sx$ and $\ddot{x} \rightarrow s^2 x$ where $s = j\omega$, $\omega = 2\pi f$, $f =$ frequency and $\omega_0 = 2\pi f_0$. The resonant frequency of the pendulum is given by $f_0 = \frac{1}{2\pi}\sqrt{\frac{g}{l}}$ in the horizontal direction. It can be seen that, above the resonant frequency, the transfer function is $\sim \frac{f_0^2}{f^2}$. A 25cm length pendulum with $f_0 = 1$ Hz, in the horizontal direction, provides an isolation factor of 10^4 at 100 Hz.

Introducing a damping force, $F = b(\dot{x}_1 - \dot{x}_0)$ where b is a constant (viscous damping), the transfer function becomes

$$\frac{x_1}{x_0} = \frac{\omega_0^2 + \left(\dfrac{b}{m}\right)s}{s^2 + \left(\dfrac{b}{m}\right)s + \omega_0^2} . \qquad (2.3)$$

For such a system the quality factor, Q, is given by $Q = \frac{\omega_0 m}{b}$ where Q is a measure of how small the dissipation is at the resonant frequency. High Q, low damping (blue) and low Q, high damping (red) curves are shown in figure (2.3). Above the resonant frequency the horizontal transfer function for a high Q system is proportional to $\frac{1}{f^2}$. For a low Q system the horizontal transfer function is proportional to $\frac{1}{f^2}$ up to a frequency $f = f_0 Q$ above which its fall off is proportional

to $\frac{1}{f}$. In the case of gravitational wave detectors the pendulum suspension of the mirrors is designed to have high quality factors in order to keep the off-resonance thermal noise at a sufficiently low level, as previously discussed. As a consequence, however, the pendulum suspension resonantly amplifies seismic noise at its resonant frequencies; these motions have to be actively damped for the operation of the detector. For the case of GEO 600 this is done with sensor and actuators acting on the pendulum. A method of passively damping the modes of a triple pendulum using high-performance magnets has been demonstrated by the TAMA group [57].
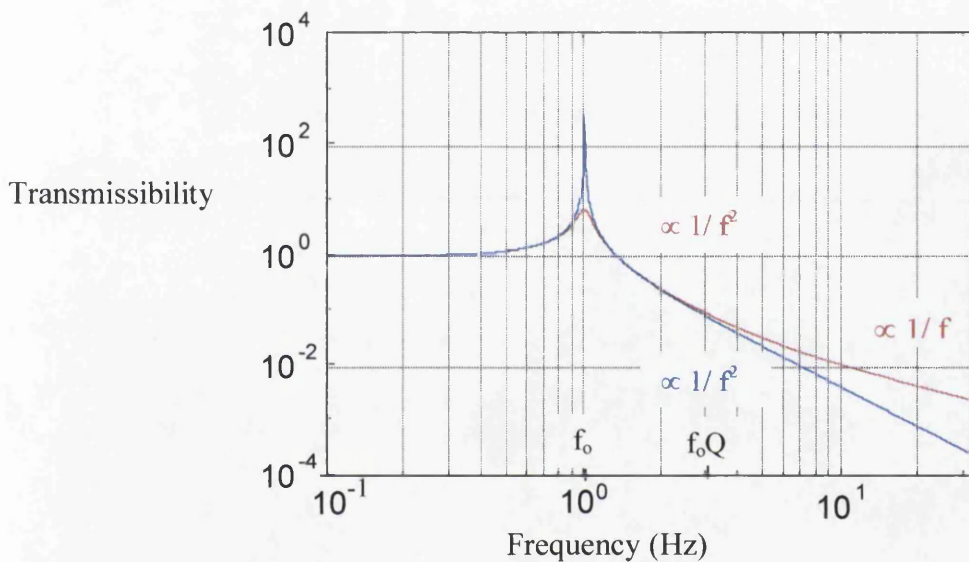
Transmissibility

Figure (2.3): - *Transmissibility versus frequency.*

It should be noted that if b is inversely proportional to frequency (structural damping) rather than viscous damping, which can be represented by a dashpot in parallel with a spring, the transfer function, $\frac{x_1}{x_0}$, equation (2.3), falls off as $\frac{1}{f^2}$ for all frequencies above the resonance. This form of damping is expected for the high Q silica suspensions of the main test mass mirrors in GEO 600.

To increase the isolation, we can suspend two or more pendulums in series. Above the highest resonant frequency, for a high Q system, the isolation will fall off as $\frac{1}{f^{2n}}$ where n is the number of pendulums.

Another example of a simple isolation system is a mass on a spring. This can be reached in practice by using a heavy mass on rubber. The transfer function is the same as that for a simple pendulum suspension, equation 2.3, where the resonant frequency is related to the mass and the elastic modulus of the rubber. This form of isolation provides isolation in both the horizontal and vertical.

2.5 Isolation Requirements for GEO 600

As already mentioned, GEO 600 is designed such that it is limited by thermal noise at 50 Hz and this corresponds to a motion of each mirror of approximately 7×10^{-20} m$/\sqrt{\text{Hz}}$ at 50 Hz. The design goal for the seismic isolation system is to achieve a noise level at each test mass a factor of 10 lower than this [45+46]. Using the measured seismic noise spectrum of $\sim \left[\dfrac{10^{-7}}{f^2} \right]$ m$/\sqrt{\text{Hz}}$ between 20 and 300 Hz, an isolation factor of 6×10^9 at 50 Hz in the horizontal and 6×10^6 in the vertical is therefore required for the mirror test masses. This assumes a 0.1 % cross coupling factor from vertical to horizontal.

There are various contributions that couple vertical to horizontal motion of the test mass. Firstly intrinsic to the design of GEO 600 is that the arms are folded vertically implying that the test mass mirrors must be tilted with respect to the gravitational field [1]. This gives a cross coupling factor of $c = \dfrac{\Delta z}{L} \sim 0.02$ % for $\Delta z = 12.5$ cm where Δz is the vertical height separation of the mirrors and L is the length of the arm [58]. Secondly due to the fact that the gravitational field is not parallel at both ends of the cavity there is a further cross coupling factor of $c = \dfrac{L}{D} \sim 0.005$ % where D is the diameter of the Earth [59]. The cross coupling due to mechanical misalignments for the proposed GEO 600 suspension design has been studied by Matt Husman [60] and he has shown that for reasonable misalignments a cross coupling factor < 0.01 % is obtained. Therefore 0.1 % is a conservative estimate of cross coupling factor from vertical to horizontal motion.

2.6 Main Mirror Isolation

The overall design of the mirror isolation in GEO 600 has been developed by myself and other members of the suspension group at Glasgow. The work carried out by the author is presented in chapters 4, 5, and 6. Presented below is a description of how the final design will be for each test mass mirror [61].

At the bottom of each suspension system, figure (2.4), there will be three legs each consisting of a two-layer isolation stack, the lower layer of which is active and the upper layer is passive. The passive layer, which behaves like a mass on a spring, consists of a steel mass on pieces of rubber. In the active layer, designed by Dr. Ken Strain in Glasgow and Dr. Aniello Grado in Hanover, feed forward, which minimises the motion caused by measurable disturbances, will be used to control the effects of the micro-seismic peak. This occurs at $\sim 0.2\,\text{Hz}$ and is caused primarily by waves crashing against the shoreline. This noise peak could affect the operation of the detector in a heavy storm. Feedback will also be used to improve the isolation at frequencies up to 10 Hz. The basic principle of feedback is to detect the vibration of a mass using an inertial sensor, to amplify and filter this signal and then to feed it back to actuators acting on the mass to reduce the vibration. The combination of feedforward and feedback will reduce the bandwidth required in the damping servos, and ease the acquisition of locking [62]. It should be noted that in the present design the active isolation does not contribute to the overall isolation in the frequency band for the detection of gravitational waves.

At the top of each stack there will be a rotational flexure, a flex-pivot, in order to reduce the rotational stiffness of the stack system, and a stack stabiliser will connect the three legs. A further structure, called the rotational stage, will provide the interface between the stack stabiliser and the pendulum system. This rotational stage provides a coarse level of rotational alignment for the pendulum assembly. In order to minimise friction there is a bearing between the stack stabiliser and rotational stage consisting of three sapphire discs sliding upon highly polished ceramic thrust plates.

The seismic isolation stages, both stacks and pendulums, have low horizontal resonant frequencies and therefore low transmissibilities in our working frequency band. However in the vertical dimension the resonant frequencies are higher. This, together with the unavoidable cross-coupling of vertical to horizontal motion of the test mass, means that for practical isolation systems involving stacks and pendulums, isolation in the vertical dimension is likely to be the overall limiting factor in the total isolation achieved.

The vertical frequency can be shown to be $f_0 = \dfrac{1}{2\pi}\sqrt{\dfrac{g}{\delta l}}$ where δl is the static extension in the wire. For a mass on a wire $\delta l \sim 1$ mm compared to a mass on a soft spring where $\delta l \sim 20$ cm.

The GEO 600 main test mass mirror suspension involves a triple pendulum in which cantilever springs are incorporated in two of the pendulum suspensions to lower the vertical frequencies and hence improve the vertical isolation. The typical vertical resonant frequency of a single pendulum is ~ 20 Hz providing an isolation factor of only 25 at 100 Hz. A typical cantilever spring has a resonant frequency of ~ 3 Hz and provides an isolation factor of $\sim 10^3$ at 100 Hz. Therefore to obtain the required vertical isolation outlined in section 2.5, two stages of cantilever blades are necessary, in addition to the vertical isolation from the single passive stack.

From the top of the rotational stage an upper mass is suspended from two cantilever springs and from the upper mass a double pendulum is suspended by a further four cantilever springs. A schematic of the overall suspension system is shown in figure (2.4).

In order to lock the interferometer it is necessary to apply a feedback force to one of the test mass mirrors. This force is produced by an electrostatic drive, which will not significantly affect the high Q of the test mass mirror. The electrostatic drive is mounted on a reaction mass which is also suspended as a triple pendulum (figure 2.4) thereby providing a seismically isolated platform for the application of global control forces in the detector [59].
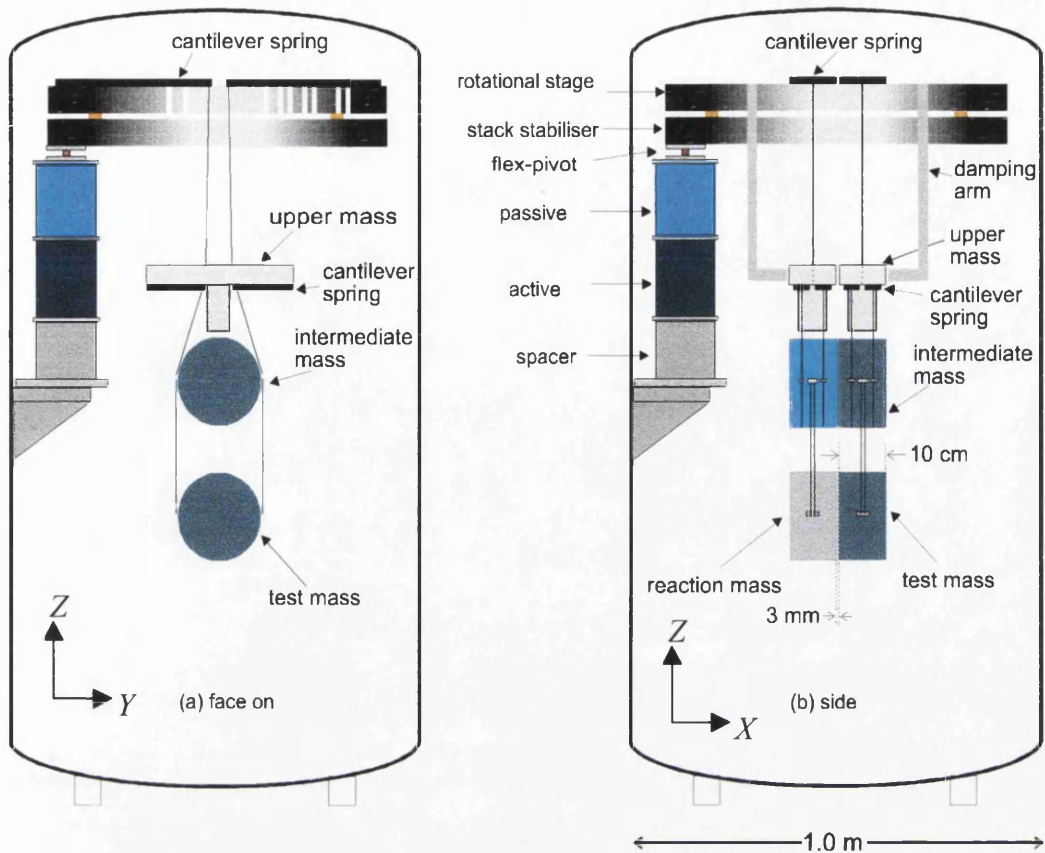
Figure (2.4): - *Schematic of main suspension. Two of the stacks have been removed for clarity.*

2.7 Other Isolation Systems

Initially most of the large laser interferometric detectors are being designed such that they are not limited by seismic noise at ~ 50 to 100 Hz. The effects of seismic noise can be reduced by improvements in isolation. VIRGO are using a multiple isolation system such that they should not be limited by seismic noise down to ~ 4 Hz [63]. This isolation system includes a superattenuator [64], consisting of a chain of cascaded pendulums, and cantilever springs with magnetic antisprings [65], which adds a negative spring constant and thereby reduces the resonance of each stage to ~ 100 mHz. Other groups around the world are looking at methods of going to lower frequencies. These include X-pendulums [66], multiple suspension wires that outline an 'X', producing very long periods of order 10 s for a pendulum of length ~ 25 cm, folded pendulums [67], long period vertical vibration isolator based on a torsion crank linkage, the use of magnetic levitation [68] and a method of combining both active and passive stages of isolation [69].

GEO 600 Sensitivity

The sensitivity curve of GEO 600 is shown in figure (2.5). The black curve is the photon shot noise calculated for a four-beam delay line illuminated by 5 W of laser light. The blue curve is the thermal noise calculated from an internal loss factor of 2×10^{-7}, a pendulum loss factor of 1.4×10^{-8} and structural damping. The red curve is the actual seismic isolation produced by the isolation stages outlined in section 2.6 and produced by Matt Husman from the work done in Chapter 6. The green curve is the total noise.
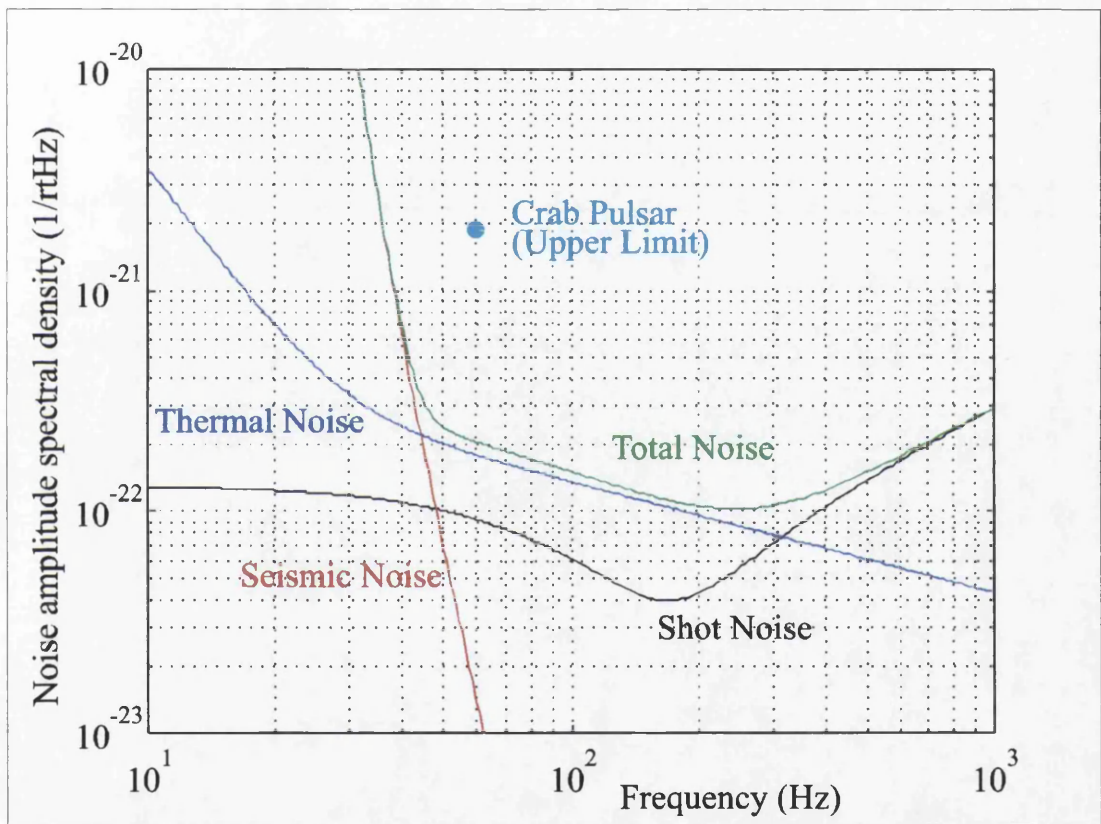
Figure (2.5): - *The estimated strain sensitivity for GEO 600.*

The various long baseline interferometric detectors discussed, aim to have initial sensitivities in the region $\sim 10^{-21}$ to $\sim 10^{-22}$ over a range of frequencies, f, from a few tens of hertz (possibly as low as 10 Hz) to a few kilohertz. GEO 600 will be able to perform stand-alone searches for continuous sources such as SCO-X1 and the Crab Pulsar. Over one year's observing time the detector's signal to noise ratio would increase placing an upper limit of $h \sim 2 \times 10^{-21}$ on the strain amplitude spectral

density for the Crab Pulsar, as shown in figure (2.5). As shown in figure (2.6) the sensitivity of the detector can be resonantly enhanced at a particular frequency (section 2.2.2).

Eventually GEO 600 will also be used along with LIGO, VIRGO and TAMA 300 to search for coincidence events from burst and stochastic sources. It is expected that GEO 600 will become operational in 2001.
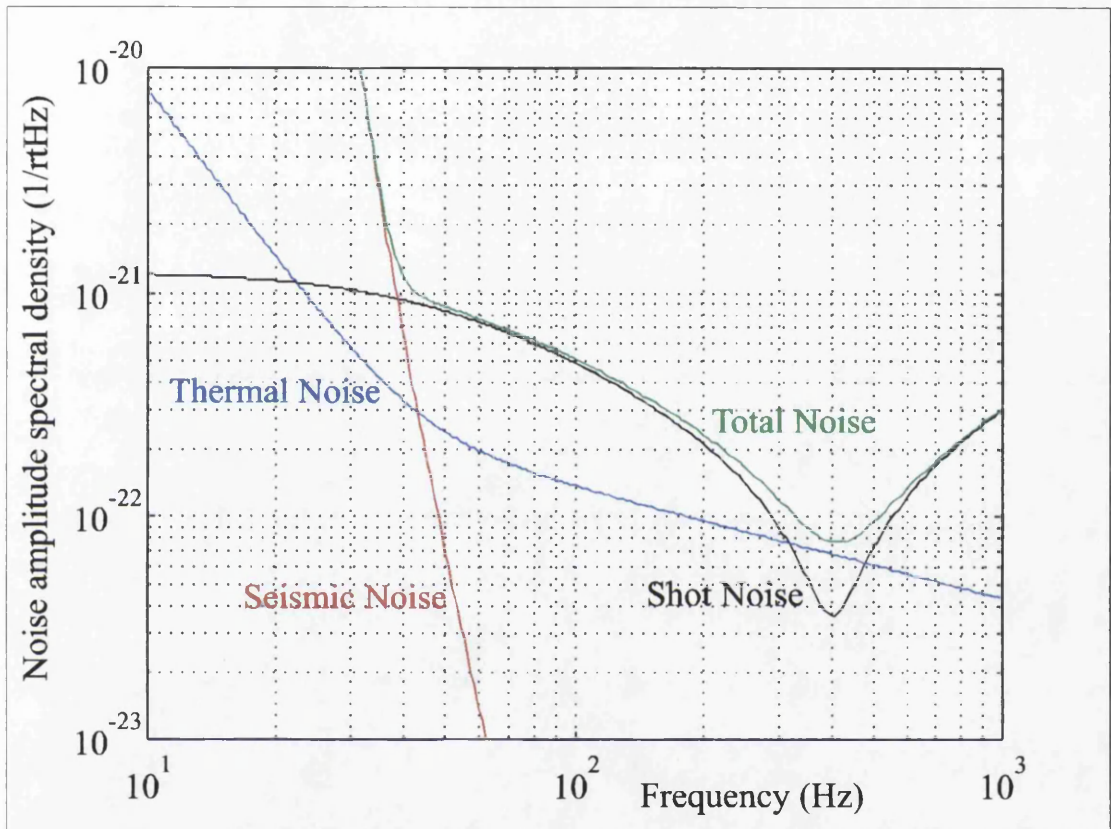
Figure (2.6): - *The estimated strain sensitivity for GEO 600. The sensitivity has been tuned to 400 Hz.*

Chapter 3

GEO 600 Mode-Cleaner

3.1 Introduction

As mentioned in section 2.2, as well as the main mirrors at the ends of each arm, there are also subsidiary suspended mirrors forming two triangular mode-cleaner cavities, placed in front of the interferometer. Each mode-cleaner cavity is a three mirror cavity one with an optical length of 8 m and the other 8.1 m. The finesse of each cavity is chosen to be 1900 and thus suppression of beam geometry fluctuations by 6 orders of magnitude should be achievable [46]. The mode-cleaner suspension does not have as stringent requirements for seismic isolation [59] and therefore does not require the extra vertical isolation supplied by the cantilever springs. The displacement noise of each mirror should be less than $dx \sim 2 \times 10^{-15}\,\mathrm{m}/\sqrt{\mathrm{Hz}}$ above 50 Hz [59]. The isolation of each mirror is achieved with a combination of several elements, as shown in figure (3.1). At the bottom of each suspension there are three legs each consisting of a two-layer passive isolation stack. A flex-pivot, as was mentioned in section 2.6, is situated at the top of each stack. A further structure, called the top-plate, interfaces between the three stack legs and each mirror suspension. In order to provide remote levelling of the top-plate a vertical motor is included in each stack leg between the passive layer and the flex-pivot. From the bottom of the top-plate each mirror is suspended as a double pendulum. Each double pendulum can rotate with respect to the top-plate via a rotational clamp, designed by Herr Klaus in Hannover, with a range of $\sim \pm 20$ mrad. There is also longitudinal adjustment of $\sim \pm 2$ cm provided by a sliding clamp. Both of these adjustments are essential in order to allow the mode-cleaner mirrors to be aligned accurately with respect to each other.
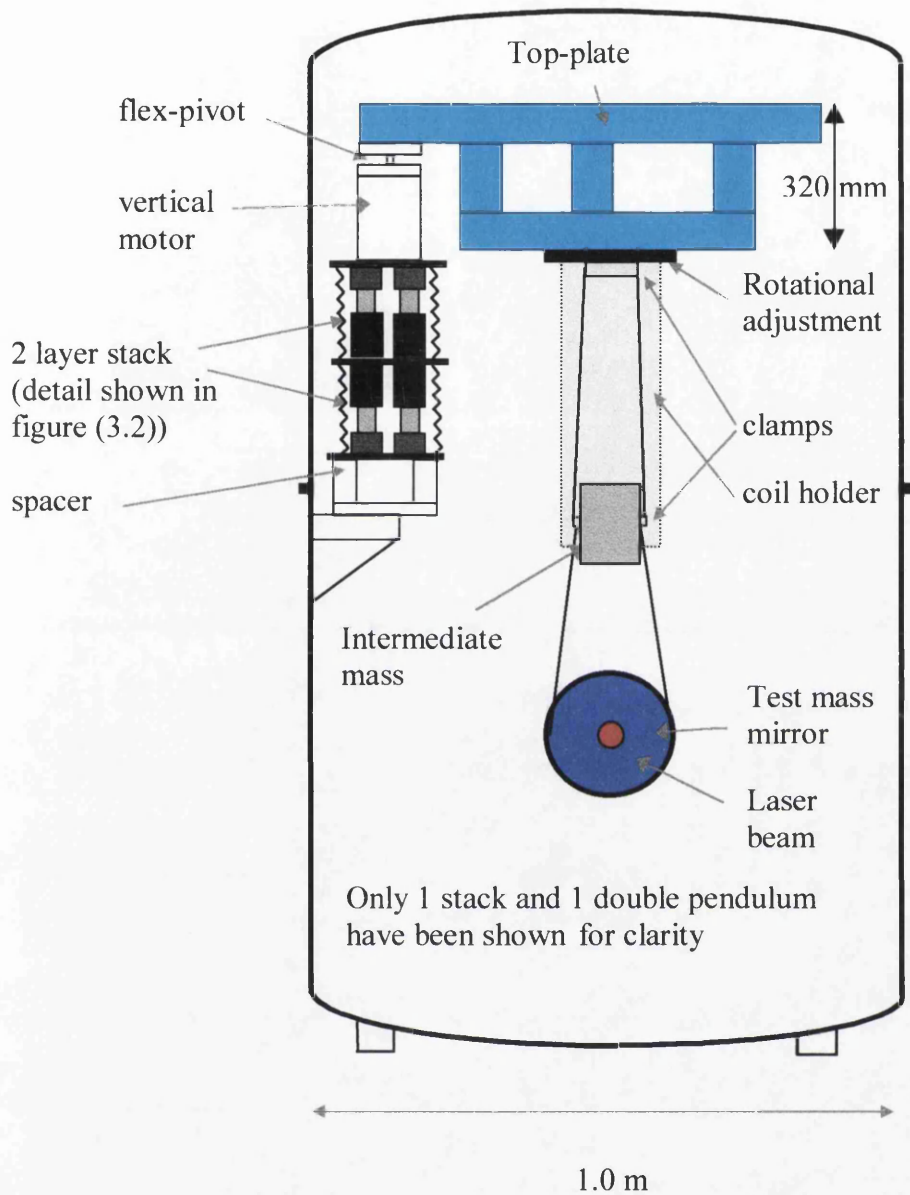
Figure (3.1): - *Face on view of overall mode-cleaner suspension (not to scale).*

3.2 Isolation Stack

3.2.1 Stack design

As mentioned in the introduction we are using a two-layer passive stack [70] in addition to the double pendulum for isolation. Each layer behaves like a mass on a

spring. In this stack the lower mass is a steel block, the upper mass is one third of the mass of the top-plate and the springs are pieces of graphite loaded silicone rubber, RTV (615) [70]. The overall transfer function of one layer is similar to that of a pendulum. However, typically the quality factor, Q is chosen to be small so that the the residual motion due to seismic noise is not enhanced at the resonances of the stack. This implies, as mentioned in section 2.4, off-resonance isolation proportional to $\frac{1}{f}$ above a frequency, $f = f_o Q$ where f_o is the resonant frequency of the stack, assuming viscous internal damping.

Silicone rubber on its own tends to have a $Q \sim 20$, rather high for use in seismic isolation stacks, and it also becomes stiffer under load [70]. Experiments at Glasgow have shown that the addition of graphite results in an improvement in damping as well as a reduction in stiffness. However too much graphite also leads to a reduction in the tear strength of the rubber making it unsuitable for use. Therefore a compromise is reached in loading the rubber with 6 % graphite by weight. The layers are encapsulated in stainless steel bellows in order to meet the GEO 600 vacuum specification, namely below 5×10^{-8} mbar for H_2 and 10^{-9} mbar for other gases. The bellows have approximate dimensions of 145 mm in height, and 140 mm internal diameter, with 0.25 mm thick walls. These dimensions have been chosen so as not to affect the overall isolation performance of the stack. The bellows are stiffest in rotation and so to reduce the possibility of transmission of ground rotation to the top of the stack a rotational flexure has been included. A Lucas flex-pivot of 1/2-inch diameter is used. With this arrangement a rotational resonance of ~ 2 Hz was measured experimentally under appropriate load. This compares with a torsional frequency of greater than 100 Hz measured without the inclusion of the flex-pivot. The bellows have several mechanical resonances. They can be damped successfully by coating the inside of the bellows with a layer of Apiezon Q-compound mixed with silicone grease. A schematic of the overall stack including flex-pivot and bellows can be seen in figure (3.2). Spacers are included, as shown, to match the height of the stack to the length of the bellows.
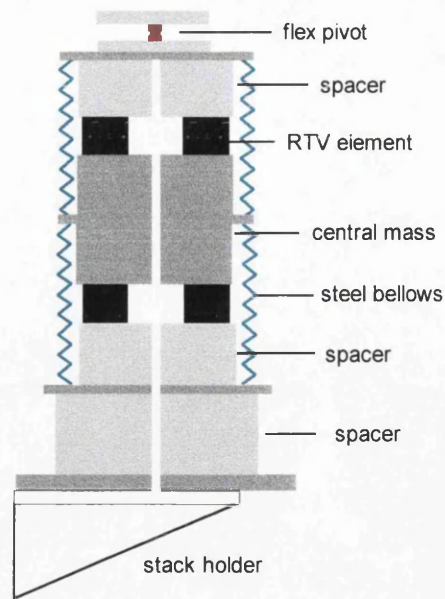
Figure (3.2): - *Vertical cross-section of stack leg and flex-pivot (the vertical motor is not shown).*

3.2.2 Vertical transfer function

A vertical transfer function, the ratio of vertical motion at the top of the stack to that at the bottom, was measured experimentally for a single prototype stack leg consisting of 2 layers of steel plus damped RTV elements. Three RTV elements per layer were used; each element cylindrical in shape with diameter = 30 mm and height = 25 mm. Each layer was encapsulated in bellows. The lower mass was 10 kg and the top mass was ~ 20 kg, representing the contribution on each stack leg from the top-plate and housing for each double pendulum suspension. The transfer function was obtained by driving the stack with a vertical shaker, constructed from piezoelectric elements, and measuring the required signals using two accelerometers, one at the top of the stack and the other at the bottom. The signals were analysed using a FFT spectrum analyser. The accelerometers and the masses were accurately centred on the axis of the stack leg in order to minimise tilt coupling to vertical motion. The measurements were performed in vacuum to prevent acoustic coupling, and indicated that an isolation of ~ 30 dB at 50 Hz was achieved, as shown in figure (3.3). A simple MATLAB [71] model, treating the stack as two spring/mass units in series, is also shown. This model was obtained from a program which allows

the input of the spring constants and masses with damping terms appropriate for the damped RTV bellows combination. The spring constants of each layer are obtained experimentally from the two resonances of the stack. This model shows a very good fit over the frequency range 20 to 120 Hz. The peaks at ~ 40 Hz appear to be related to the driving mechanism and the peak at ~ 70 Hz is the damped bellows resonance.

3.2.3 Horizontal transfer function

A horizontal transfer function for a prototype single stack leg of the same design as above was also obtained, as shown in figure (3.4). The stack leg was driven by a horizontal shaker, provided by Henrich Klein (MPQ, Garching). The accelerometers and the masses were accurately aligned on the central axis of the stack leg in order to minimise tilt cross coupling to horizontal motion. A theoretical horizontal transfer function was again obtained with MATLAB; this is superimposed onto the experimental plot. There is some excess around 30 Hz, which appears to be due to some cross coupling from vertical to horizontal motion. The peak at 50 Hz corresponds to electrical mains interference. Isolation of ~ 50 dB at 60 Hz is achieved in the horizontal direction.

As outlined above, experiments on both the vertical and horizontal transfer function of a two layer passive stack imply that our stack gives good isolation in both the vertical and horizontal direction. The mode-cleaner stacks used for GEO 600 were manufactured in Germany, with designs supplied by Dr. Mike Plissi and Dr. Ken Strain in Glasgow. A photograph of two of these stacks, taken during the construction phase, is shown in figure (3.5).

This photograph shows, starting from the bottom of the stack on the left: steel legs, spacer, rubber, central mass, rubber, spacer. The stack on the right hand side includes one of the bellows for encapsulating the lower passive layer. The vertical motor and the lower half of the flex-pivot can also be seen at the top of the stack. The four vertical rods which can be seen on each stack are end-stops which are included to prevent damage to the stacks during transit from the laboratory to the GEO 600 site and to prevent excessive sideways motion during installation of suspensions.
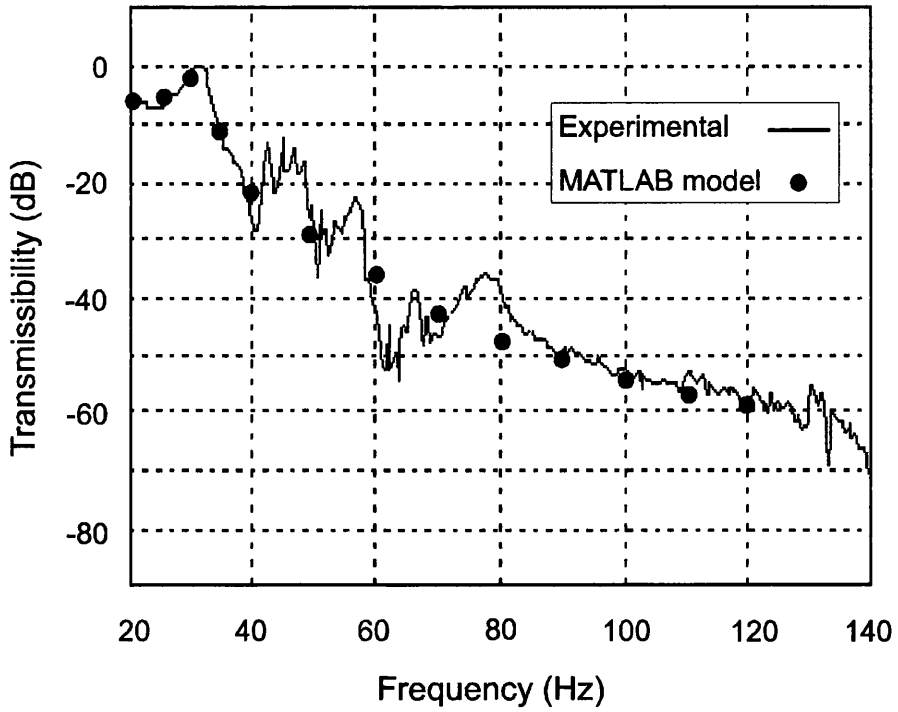
Figure (3.3): - *Vertical transfer function of a two layer stack. Both the theoretical and experimental results are shown.*
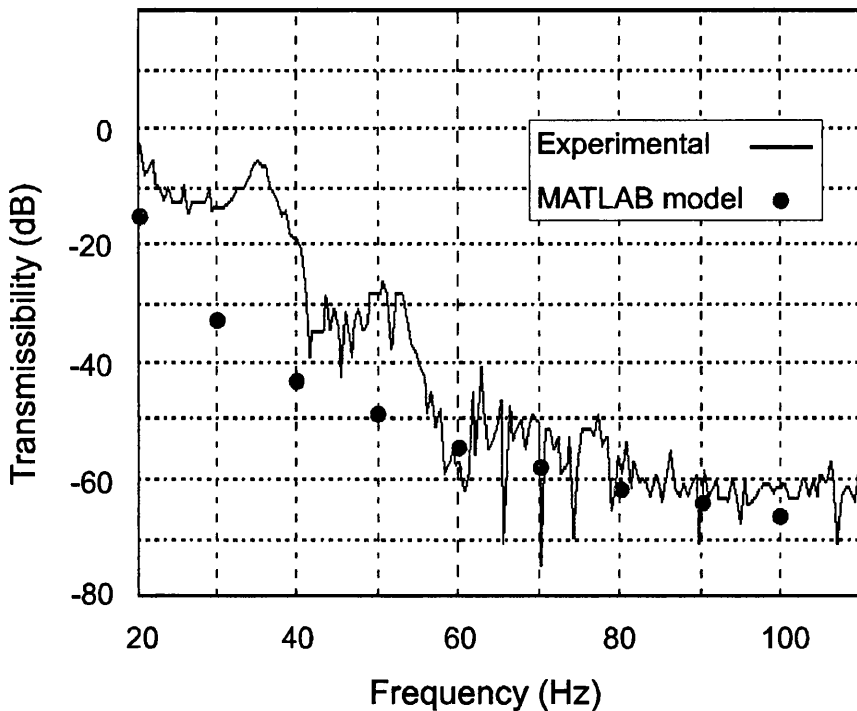
Figure (3.4): - *Horizontal transfer function of a two layer stack. Both the theoretical and experimental results are shown.*

Figure (3.5): - *Photograph of two of the stacks during construction.*

3.3 Top-Plate

3.3.1 Introduction

A detailed diagram of the optics in the pair of mode-cleaner tanks is shown in figure (3.6). Due to the fact that the number and position of the mirrors in each tank is not the same a different design of top-plate is required for each tank. Each top-plate must meet certain requirements. Firstly each plate has to be able to support several double pendulum mirror suspensions without flexing too much. This implies it has to be relatively rigid. Secondly in order to avoid the amplification of the mechanical motion transmitted from the ground it must have low Q resonances. It must also have a low centre of gravity for static stability and the choice of material must be vacuum compatible. Lastly it has to interface between the top of the stacks and the top of the double pendulums, see figure (3.1). When the top-plate was being designed the height of the stack and the double pendulum were already fixed. Therefore it was necessary that the top-plate was 320 mm in height to ensure that each mirror was at the correct height.

3.3.2 Finite element analysis

Modal Analysis is a means of determining modal parameters (natural frequencies, mode shapes and damping factors). This is often done by the approximate theoretical method of finite element analysis. Finite element analysis of the top-plate was carried out using I–DEAS [72]. Geometric properties, material properties, element types and element sizes of the model require to be input into the program [73]. It then assembles the corresponding spring and mass matrices and finally solves the eigenvalues and eigenvectors to get the natural frequencies and mode shapes respectively.

The co-ordinates of the point of attachment of each double pendulum suspension and the three stacks were added as initial fixed nodes. The boundary conditions which were implemented were that the co-ordinates of the points of attachment of the stacks were rigidly constrained in three dimensions.

Key: -

☐ Double pendulum (figure (3.10)).

◯ Stack (figure (3.2) and (3.5)).

☐☐ Double pendulum and reaction mass pendulum (figure (3.12)).

☐
☐ Mounting unit (suspended as double pendulum) consisting of two
☐ Faraday isolators and one pockel cell [74].
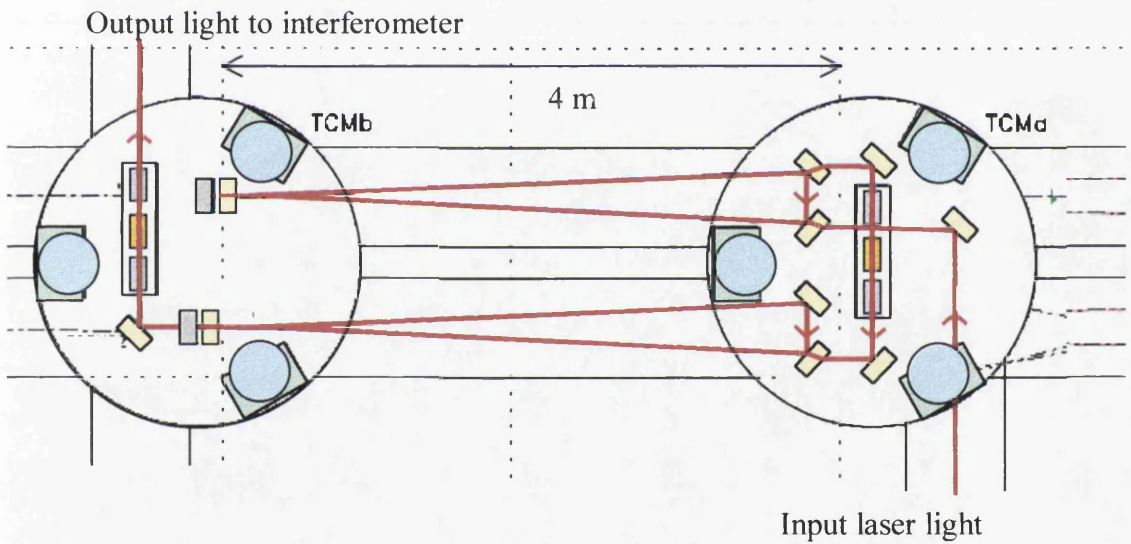
Figure(3.6): - *GEO 600 mode-cleaner.*

The investigation of various designs, including the overall shape and the choice and shape of material elements has been carried out, as outlined below.

3.3.3 Design

Firstly the structure was modelled from solid sections. The lowest resonant mode frequencies of the modes of vibration of both mode-cleaner top-plates, calculated using I–DEAS [72], were found to be below 100 Hz. The frequencies were raised, i.e. the structure was made stiffer, by going to box-section. The initial box section results were predicted by calculating the moment of inertia of a solid and box section with the same mass per unit length. The ratio of the moments of inertia [75,76] gave the factor of improvement by going to box-section for both the vertical and horizontal resonances. This prediction was confirmed by modelling the top-plate made from box section using I–DEAS [70]. The final stage was to improve the choice of box section within the confinements of the overall height and the available dimensions of material. This was achieved by maximising the moment of inertia for a given mass and also taking into account the bending stress and static deflection of the box section. Steel box section was chosen for its high stiffness to weight ratio and ease of welding. Aluminium had been chosen initially for its low density, however tests indicated that the welding together of aluminium sections would prove difficult [77]. The two-layer structure shown in figure (3.7) and figure (3.8) has been chosen as the optimum design. Each layer of the top-plate has dimension 40 mm width by 80 mm depth with 2 mm thick walls. The intermediate struts connecting the two layers have dimensions 40 mm by 40 mm with 2 mm thick walls, implying an overall weight of each top-plate of ~ 35 kg. The lowest resonant mode frequencies of the modes of vibration of both mode-cleaner top-plates, calculated using I–DEAS [72], were found to be above 200 Hz. The overall attenuation from the double pendulum and the two layer passive isolation stack increases rapidly with frequency. Therefore as long as the Q of the resonances are low enough they will not amplify mechanical motion transmitted from the ground, which could affect the sensitivity of the detector. To ensure that the Qs are low enough, damping is required, as discussed in the next section.
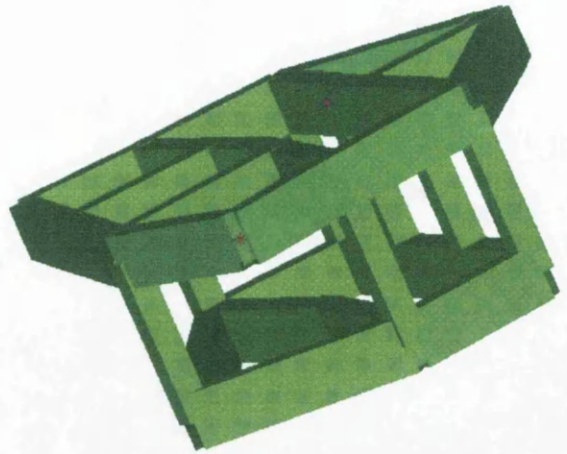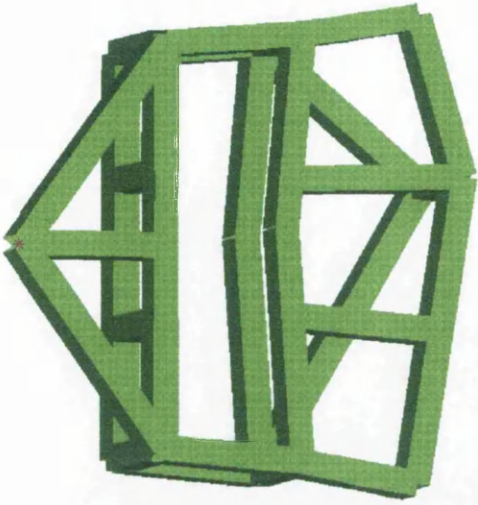
Figure (3.7): - *Two schematics of the top-plate for tank TCM a: - (a) view from above (b) side view.*

(a)

(b)
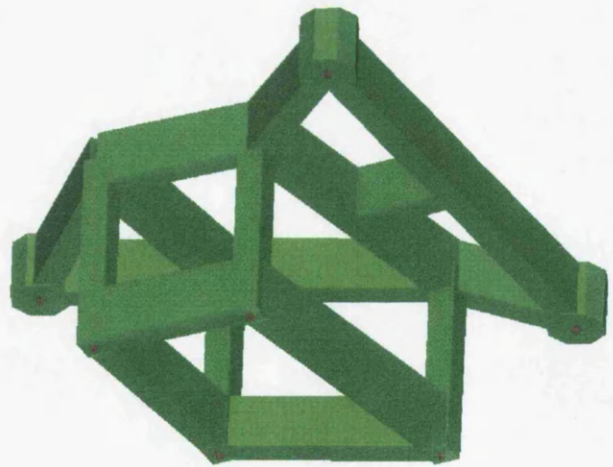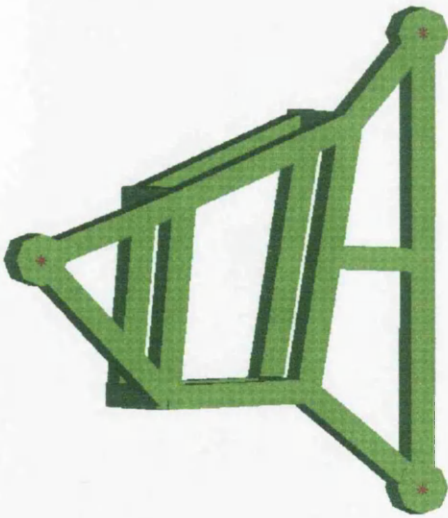
Figure (3.8): - *Two schematics of the top-plate for tank TCM b: - (a) view from above (b) side view.*

3.3.4 Damping

Structural elements, like our top-plates, exhibit a number of normal modes. If they are subjected to random vibrations a number of resonances can become excited. Because most engineering materials like steel or aluminium have $Q \gg 50$ the damping of resonant vibrations must be done artificially. In order that the top-plate is vacuum compatible the damping materials are applied to the inside of the box-section. Two main types of artificial damping were investigated. The first was the application of a visco-elastic polymer with high internal losses. Here the long chain molecules are free to vibrate and thereby dissipate kinetic energy as heat.
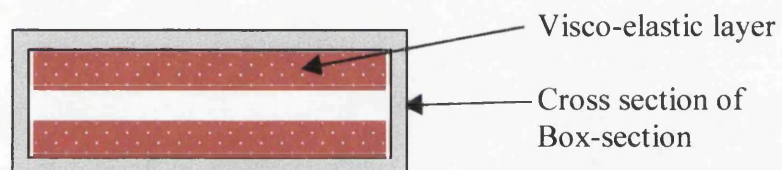
The second method was to apply a constrained layer [78]. Here the damping material was covered with a thin metal sheet forming a sandwich type arrangement, as shown.
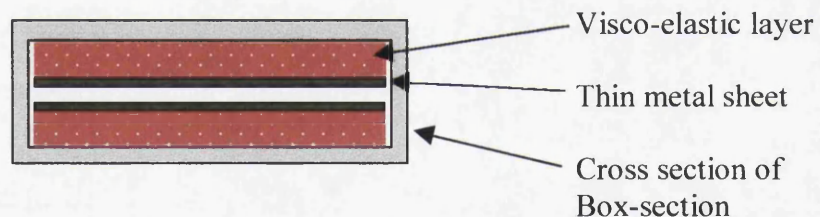
When the composite material vibrates the constrained damping layers are subjected to shear effects, which cause the vibration energy to be converted into heat and hence dissipated [79]. It should be noted that the damping properties of the visco-elastic materials can be both frequency and temperature dependent [80].

3.3.5 Tests on damping materials

A section of box aluminium with dimensions 50 cm long by 10 cm broad by 5 cm deep with 0.6 cm thick walls was used for testing various damping materials and techniques. To determine its Q, it was hung horizontally as a single pendulum in air. A vertical shaker was bolted to one of the ends and connected to a signal generator

that was used to provide the drive. The output was obtained using an accelerometer, bolted onto the middle of the box-section, and measured on an oscilloscope. The signal generator was used to scan through the frequency range of 1-2 kHz, which covered the first four resonances of the section. At a resonance peak the Q was measured, using an oscilloscope, as: -

$$Q = \frac{f_n}{\Delta f_n} \qquad (3.1)$$

where Δf_n is the bandwidth at the half power points (6 dB points) and f_n is the resonant frequency where n is the mode number. For all of the tests the damping material formed a thin coating over all of the inside walls of the section and contributed to about $10 - 20 \%$ of the total weight. From the measured Qs from the first four resonances the loss factor, ϕ was calculated using: -

$$\phi = \left(\frac{1}{Q_D} - \frac{1}{Q_U} \right) \qquad (3.2)$$

where Q_D and Q_U are the Qs measured with and without the damping material respectively. This eliminated the fact that the experiment was carried out in air, allowing the effect of the damping material to be observed on its own. This result is also therefore independent of the metal from which the box-section is made. The average loss factor, $< \phi >$ was then calculated, and hence the average Q,: -

$$< Q > = \frac{1}{< \phi >} \qquad (3.3)$$

$< Q >$ for each material is quoted in table (3.1).

As an example for graphite loaded silicone rubber a value of $Q_U = 550$ and $Q_D = 40$ was measured for the first resonance of the bar of ~ 1000 Hz, implying a value of $\phi = 0.023$.

The GEO 600 vacuum system will have to be baked to 80°C in order to remove water vapour from the vacuum tank, thus allowing an improved vacuum. Therefore

due to the variation of the behaviour of the damping materials with temperature [80] each material was baked to 100°C for 30 minutes and the Q from before and after compared, as shown in table (3.1).

MATERIAL / DESCRIPTION	AMOUNT ADDED as a % of the TOTAL WEIGHT	$<Q> = \dfrac{1}{<\eta>}$	AFTER BAKE TEST $<Q> = \dfrac{1}{<\eta>}$
VISCO-ELASTIC DAMPING			
1. Q- mixture, 3:1 Q compound + silicone grease (visco-elastic)	10	250	250
2. WAXOYL (rust-proofing for cars)	10	100	(liquefies)
3. Sorbothane (visco-elastic polymer)	13	50	70
4. Bitumen felt	13	40	140
5. Graphite loaded silicone rubber (15 % graphite by weight)	15	60	60
CONSTRAINED LAYER DAMPING			
6. Q- mixture and thin aluminium sheet (constrained layer)	13 (0.3 mm Al)	50	50
7. 3-M tape and thin aluminium sheet (constrained layer)	3 (0.3 mm Al)	100	120

Table (3.1): - *Investigation into various materials for damping the resonant modes of a test box-section of aluminium.*

3.3.6 Final choice

Experience obtained from SKODOCK, the company who manufactured the top-plates, told us that the damping material must be applied after the sections have been

welded together, in order to prevent contamination of the weld from the damping material. This therefore restricted our choice of damping material and ruled out completely the use of constrained layer damping, because it must be applied before welding. An aperture nozzle is fitted to each layer of the top-plate, allowing the damping material to be added after welding. The aperture is then sealed with a vacuum flange.
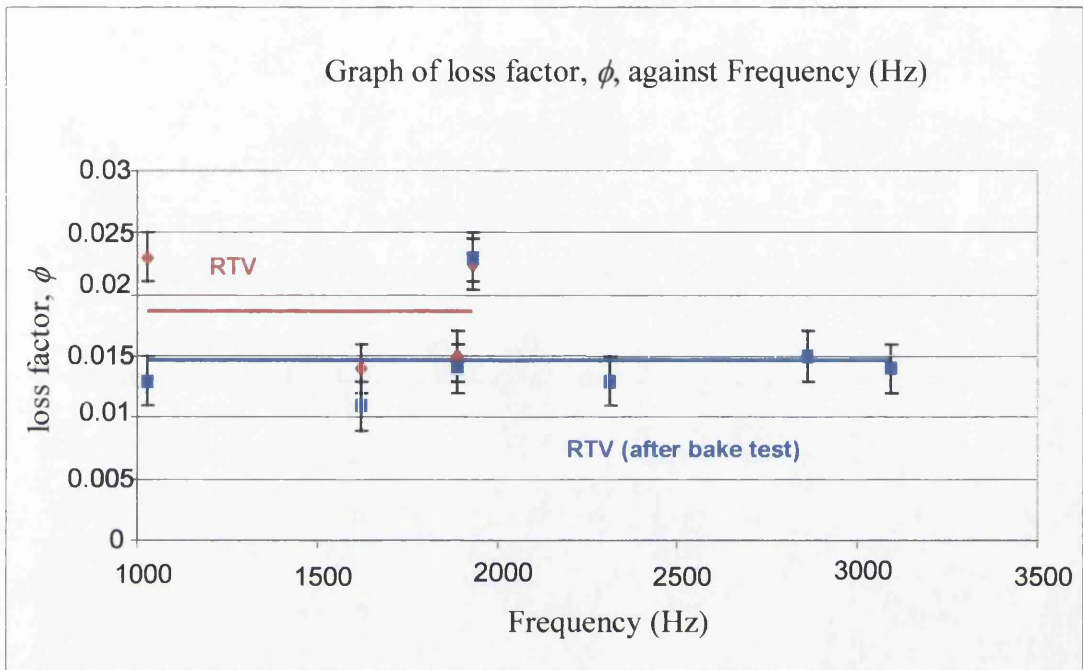
Figure (3.9): - *Final choice of damping material – RTV (graphite loaded silicone rubber) . The straight line represents the average value of the loss factor, ϕ, before (red) and after the bake test (blue).*

Graphite loaded silicone rubber is used as the damping material. It is easily applied in its initial liquid form before curing, forming a thin coating over the inside walls of the box-section. More importantly it has been shown to survive the bake test at 100°C with only small changes in its damping properties. Figure (3.9) shows how the damping properties of graphite loaded silicone rubber varies with frequency before and after the bake test. The results taken for the ϕ for each resonance of the bar, after the bake test show that ϕ is constant over a factor of three in frequency, implying structural damping is present. Finally it has very good damping properties leading to an average quality factor, $<Q> \sim 65$ (1.5 % loss factor) of the resonances with an addition of 15 % by weight. This is shown as the blue line in figure (3.9).

3.4 Double Pendulum Suspension

The mode-cleaner mirrors are suspended as double pendulums, where the transfer function becomes proportional to $\frac{1}{f^4}$ above the highest resonant frequency, for a high Q system. The mirrors are made from fused silica with dimensions 100 mm diameter by 50 mm thick, giving a mass of 0.86 kg. Each mirror is suspended on four stainless steel wires from an intermediate mass, made from aluminium with dimensions 70 mm by 50 mm by 85 mm in the X, Y, and Z directions respectively, which in turn is suspended from two stainless steel wires. A schematic of the mode-cleaner double pendulum is shown in figure (3.10). The mode frequencies of the double pendulum were predicted using a MATLAB [71] model of a double pendulum written by Dr. Stuart Killbourn [59]. These mode frequencies were verified experimentally on the mode-cleaner prototype [81]. As explained in section 2.4 for a simple pendulum, the resonant modes of the double pendulum require to be actively damped, and this is done with sensors and actuators acting at the intermediate mass. Applying the damping at the intermediate mass ensures that any extra motion caused by electronic noise in the sensor or actuator is filtered by the lower pendulum stage and therefore does not affect the mirror.

The active damping system uses co-located damping, a shadow sensor (consisting of a LED/photodiode assembly and an opaque flag interrupting the light beam) is used to sense the displacement of the pendulum and then an actuator applies a feedback force, after suitable filtering, at the point of sensing to counter the motion. The feedback force is provided by passing a current through a coil of wire and this interacts with a magnet attached, in this case, to the intermediate mass [29].

The modelling of a local control servo indicated that the longitudinal, tilt, sideways and rotational modes of the double pendulum can be actively damped using four-sensor/actuators [59]. The power spectral density (PSD) was measured on the mode-cleaner prototype in both the rotational and tilt directions for both the undamped case, red curve, and the damped case, green curve, as shown in figure (3.11) and figure (3.12) for the rotational and tilt directions respectively. The vertical and roll modes are left undamped.

The magnets are fixed with Ceramabond 571S, vacuum compatible adhesive, to the intermediate mass and the coils are mounted on a coil-holder, attached to the top-plate. There is one coil-holder for each double pendulum. The sensor/actuators have the following arrangement: -

- Two on the main section of the holder, which damp the tilt and longitudinal modes of the double pendulum.

- One on each side arm, acting on either side of the intermediate mass, which damp the sideways and rotational modes of the double pendulum.

A schematic of the set-up for each modecleaner mirror is shown in figure (3.10).

As already mentioned in section 2.2, the mode-cleaner cavity must be locked to the input laser light. This requires actuation on one of the mirrors to provide feedback to the length of the cavity. Three actuators, adapted units without sensors, apply a force to one of the mode-cleaner mirrors in each mode-cleaner. The coils are mounted on an aluminium reaction mass suspended as a double pendulum, as shown in figure (3.13). The hole in the aluminium reaction mass is to allow the laser light to pass through as shown in figure (3.6).
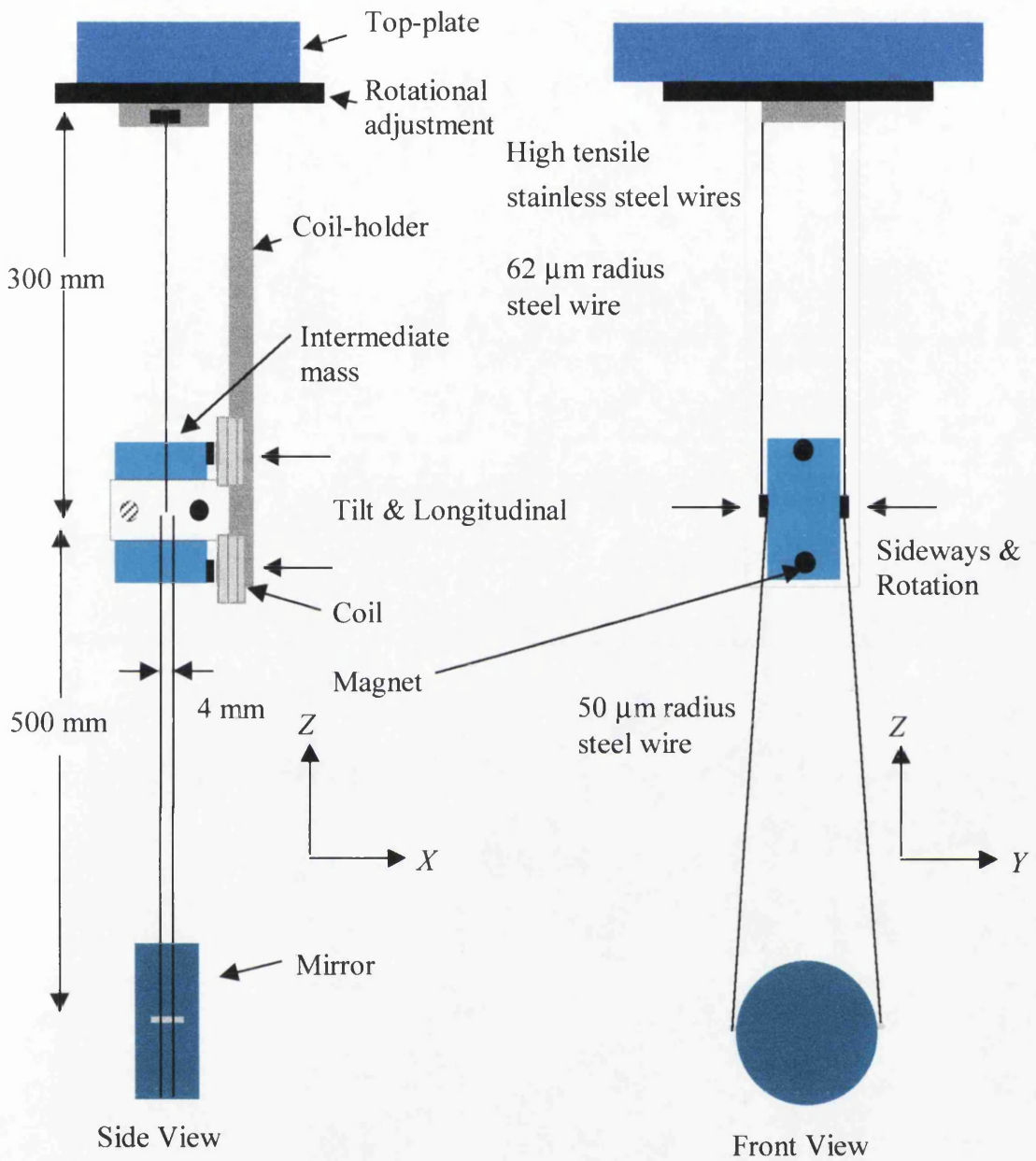
Figure (3.10): -*Mode-cleaner double pendulum suspension.*
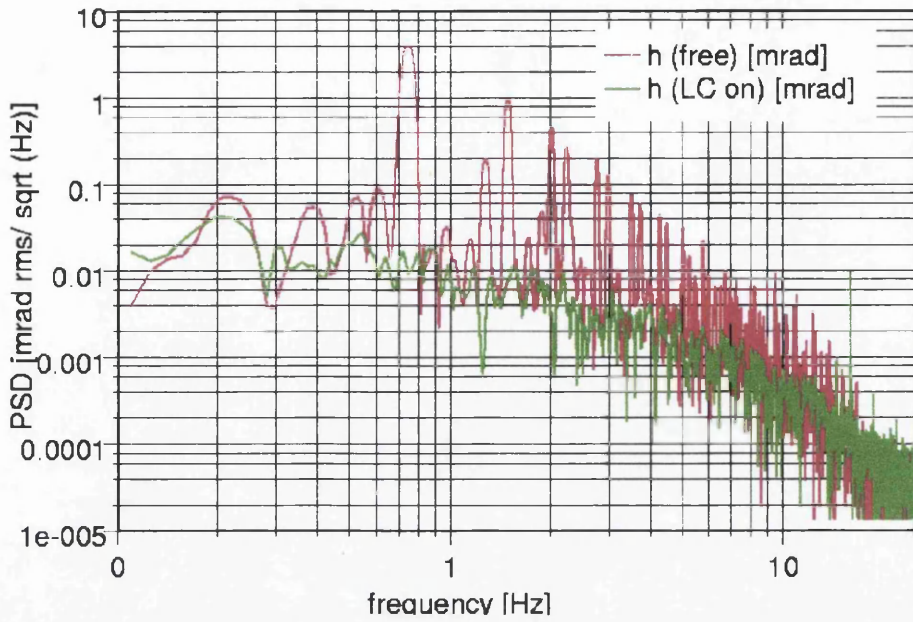
Figure (3.11):- *The power spectral density (PSD) against frequency of the mode-cleaner prototype in the rotational direction for both the undamped case, red curve, and the damped case, green curve.*
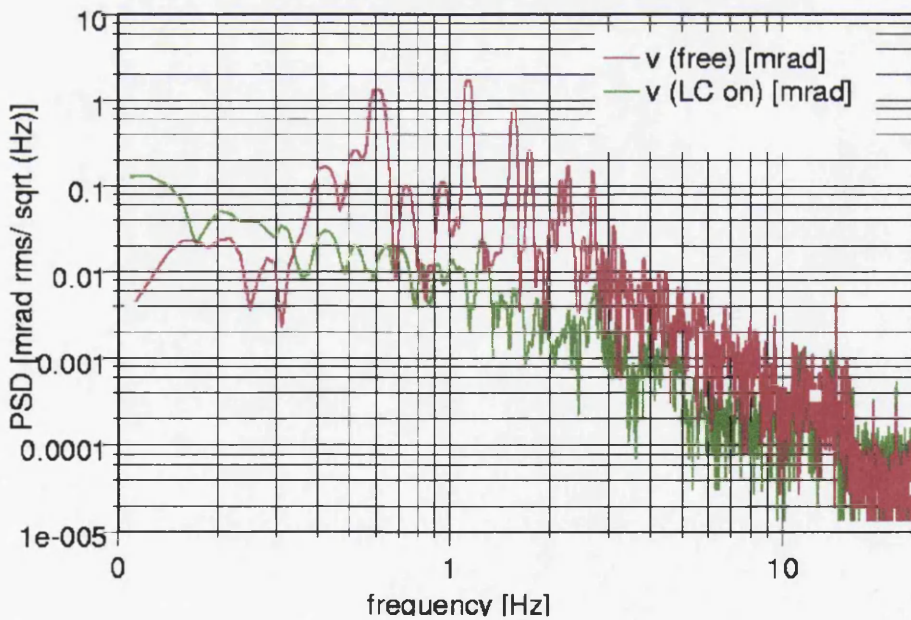
Figure (3.12):-*The power spectral density (PSD) against frequency of the mode-cleaner prototype in the tilt direction for both the undamped case, red curve, and the damped case, green curve.*
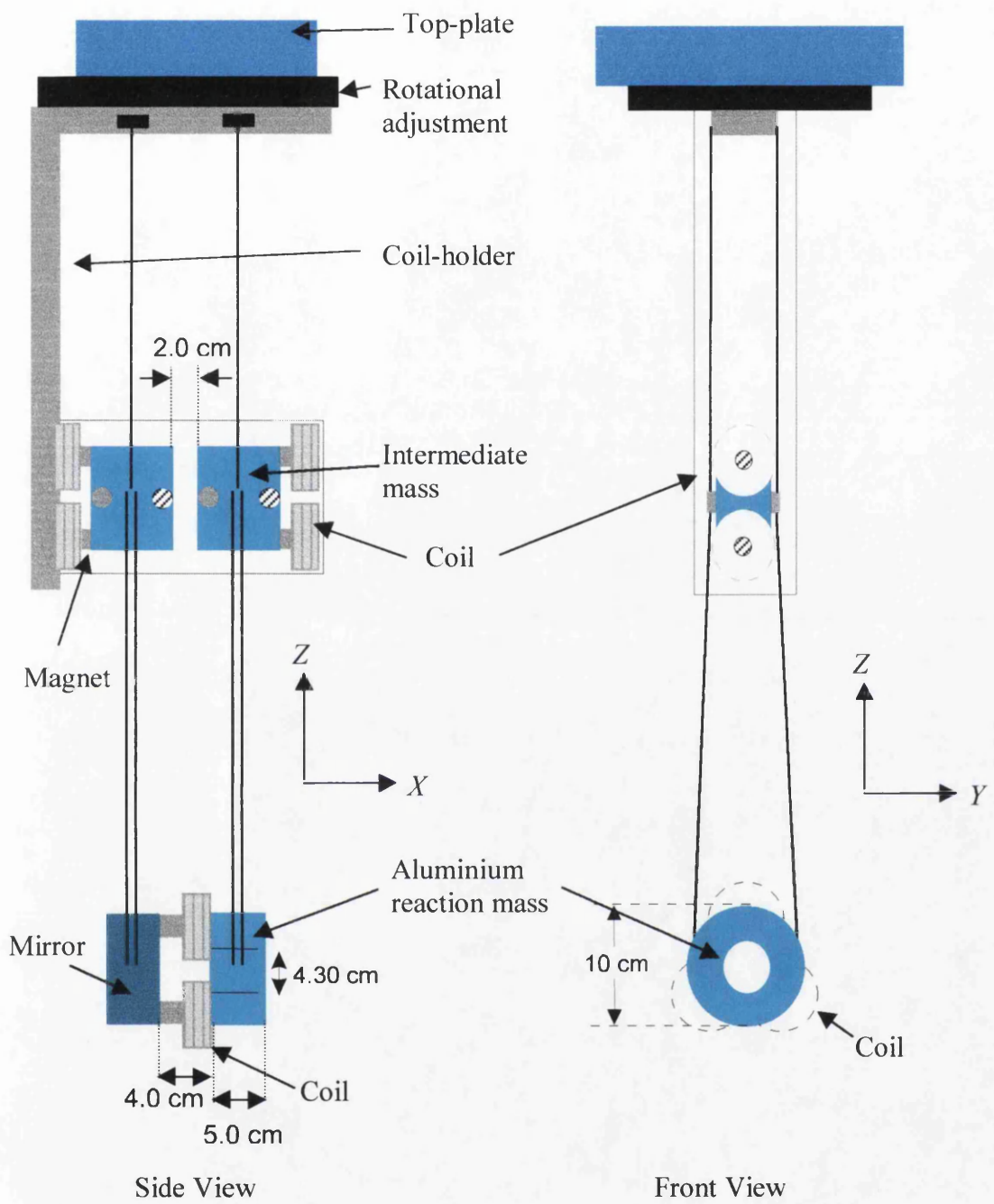
Figure (3.13):- *Mode-cleaner double pendulum suspension and reaction mass suspension.*

3.5 Transfer Function

It is possible to write an expression for the vertical transmissibility, T_v, of the mode-cleaner suspension system above the highest resonance frequency, where the system consists of a two-layer passive isolation stack and a double pendulum suspension.

In the vertical direction: -

$$T_v = \left[\frac{f_{sv}}{f}\right]^2 \left[\frac{f_{pv}}{f}\right]^4 c \qquad\qquad (3.1)$$

where f_{sv} is the geometric mean frequency of the stack (18 Hz), f_{pv} is the geometric mean frequency of the double pendulum (~ 20 Hz) and c is the cross-coupling factor (0.1 %).

$$\Rightarrow \qquad T_v = 5.2 \times 10^{-8} \text{ at } f = 100 \text{ Hz.}$$

With a ground noise spectrum of $\left[\dfrac{10^{-7}}{f^2}\right]$ m$/\sqrt{\text{Hz}}$ we obtain a resulting test mass motion $dx \sim 5.2 \times 10^{-19}$ m$/\sqrt{\text{Hz}}$ at 100 Hz, which more than adequately meets the noise specification outlined in section 3.1.

3.6 Transfer and Installation of Mode-Cleaner

The design and testing of the prototype mode-cleaner suspension has been outlined in the previous sections. The isolation properties have also been shown to satisfy the requirements for the GEO 600 mode-cleaner. The installation of the mode-cleaner at the GEO 600 site, near Hannover, started in December 1998. The transfer of the design has been undertaken by Dr. Mike Plissi and myself working closely with Dr. Benno Willke, Dr. Peter Aufmuth and Dr. Harald Lueck in Hannover. Before the installation started, several pre-installation stages had to be undertaken. Firstly drawings and sketches of the various parts were transferred to Germany for the construction in the workshop. Secondly a prototype was put together in the laboratory to ensure all of the components interfaced successfully. A photograph of

the German prototype mode-cleaner suspension is shown in figure (3.14) and (3.15). The three stacks can be seen supporting one of the top-plates. One test mode cleaner mirror, made from aluminium, can be seen suspended as a double pendulum with the coil-holder and coils also shown. The next step was to clean all of the parts from this prototype in an ultrasonic bath and bake them in an oven in order to make them vacuum compatible. Lastly all of the components were installed into the tanks under cleanroom conditions. At the time of writing both sets of stacks and top-plates have been installed in the mode-cleaner tanks and three double pendulums have been installed. During this installation period I have worked in Hannover on various occasions with Dr. Mike Plissi.
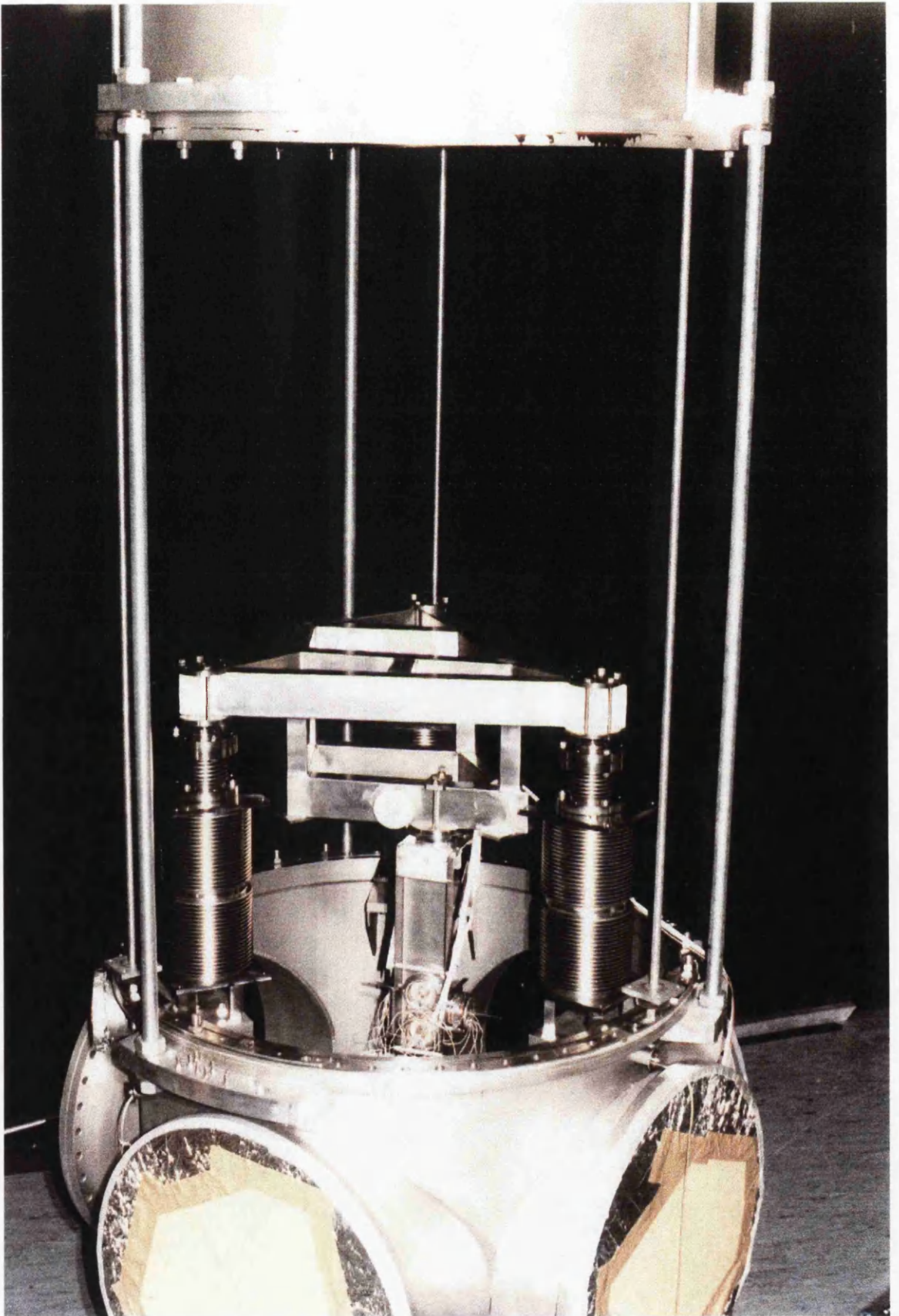
Figure (3.14): - *Photograph of the German prototype mode-cleaner suspension.*
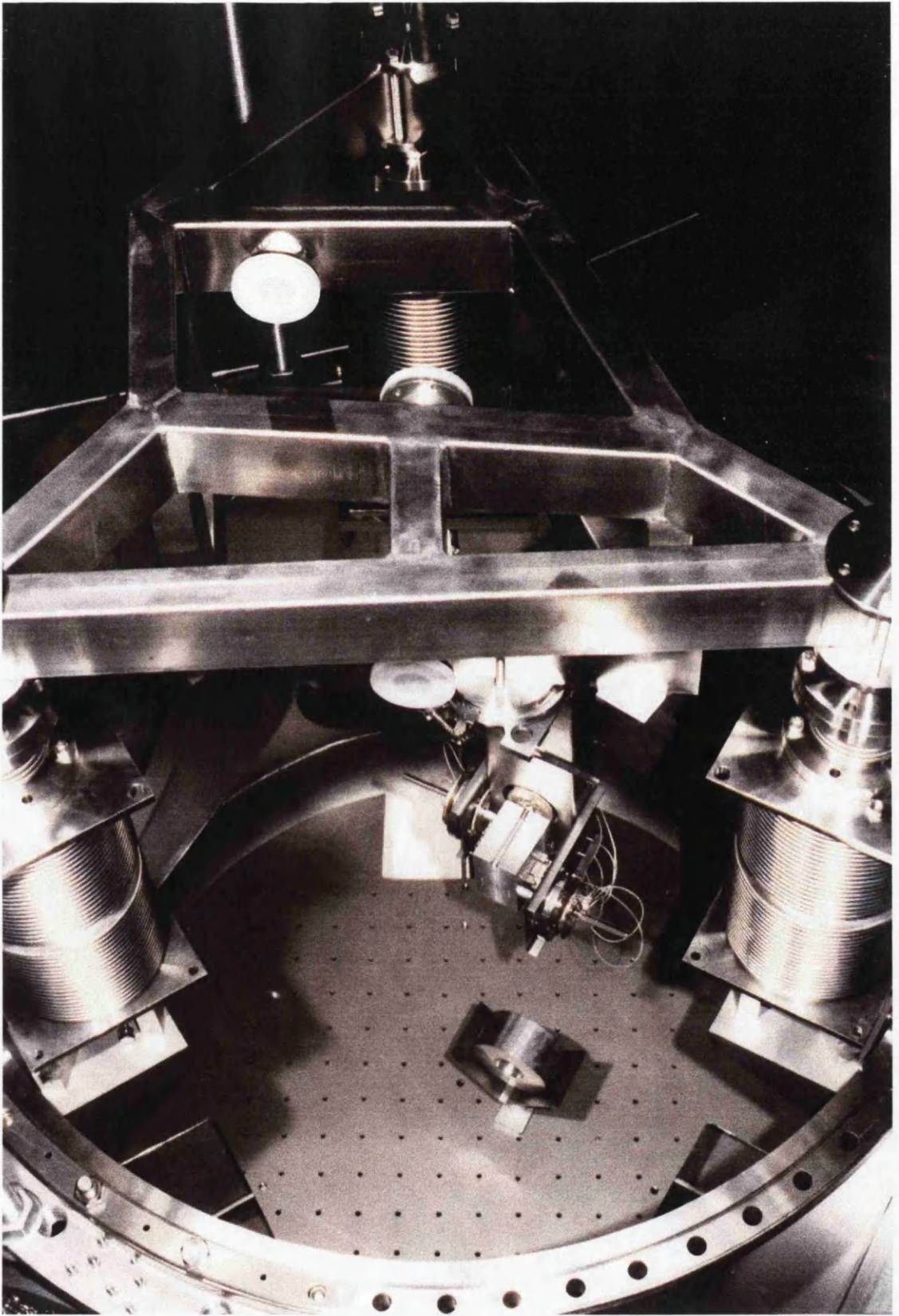
Figure (3.15): - *Photograph of the German prototype mode-cleaner suspension.*

Chapter 4

Model of a Pendulum Suspension

4.1 Introduction

As already mentioned in section 2.6, in GEO 600 a triple pendulum suspension is used for each main test mass. A model is therefore required to calculate the mode frequencies and dynamic response of such a pendulum. However in order to understand the mechanics of a triple pendulum it is necessary firstly to model a single pendulum. The equations of motion of a single pendulum (section 4.3 to 4.6) are derived for all the degrees of freedom (section 4.2). The model is then used to investigate how various parameters, for example the separation of the wires, affect the mode frequencies (section 4.7). The extension to a triple pendululm is outlined in chapter 5.

4.2 Single Pendulum

A single pendulum as shown in figure (4.1) was modelled, including all of the geometrical effects of gravity and the stretching of the wires, assuming negligible damping. The mass is assumed to be rigid with the wires acting as linear springs obeying Hooke's law. A single pendulum has six degrees of freedom and therefore six mode frequencies, which are as follows: -

> Longitudinal motion, x, translation parallel to the X-axis
>
> Sideways motion, y, translation perpendicular to the X-axis
>
> Vertical motion, z,
>
> Roll, ψ, about the X-axis
>
> Rotation, σ, about the Z-axis
>
> Tilt, ϕ, about the Y-axis

Two different techniques were used, firstly writing down the differential equations of motion using Newton's second law, as presented here, and secondly calculating the kinetic and potential energy in order to utilise Lagrange's equations. This second technique was modelled with Matt Husman [82].

SIDE ON   **FACE ON**
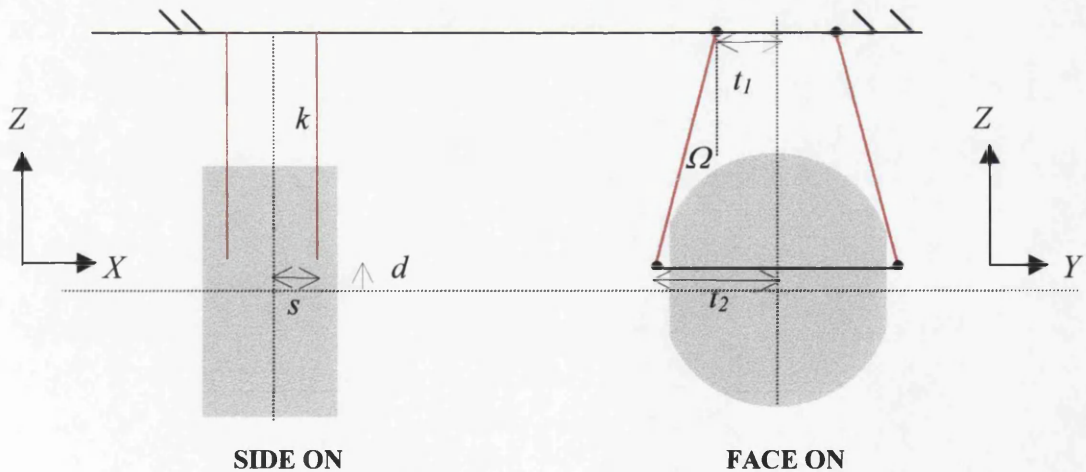
Figure (4.1): - *Schematic of a single pendulum.*

The parameters used are: -

l = the length of a wire,

s = the half separation of the wires in the X-direction,

t_1 = the half separation of the wires in the Y-direction at the suspension point,

t_2 = the half separation of the wires in the Y-direction at the mass,

d = the distance the wires break-off above the line through the centre of mass

and

k = the spring constant of one wire.

The differential equations of motion for all of the degrees of freedom outlined above are now obtained for a single pendulum. To first order the vertical and rotation frequencies remain uncoupled in the following arrangements. The sideways and roll pair and the longitudinal and tilt pair are coupled. Both modelling techniques, outlined above, produced the same results.

4.3 Vertical

Consider a single pendulum of mass m suspended from two wires of length l with spring constant k and at an angle of Ω with the vertical. In static equilibrium we have: -
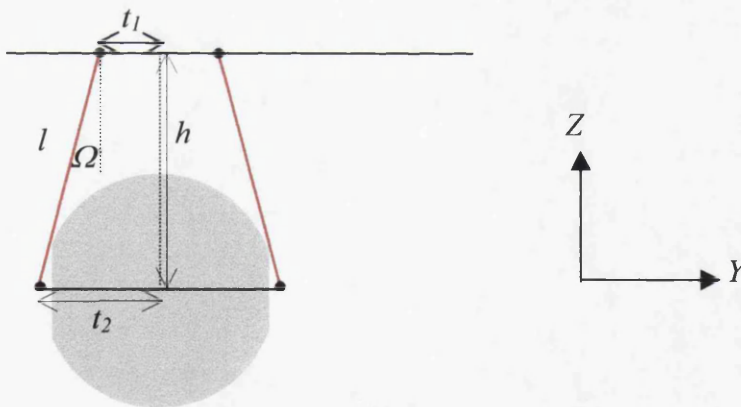
Figure (4.2): - *Face on view of cylindrical mass.*

$$l = l_o + \Delta l_o \qquad (4.1)$$

where l_o is the unstretched length of the wire. $T = k\Delta l_o$ is the tension in the wire due to the gravitational loading. Hence since $T = \dfrac{mg}{2\cos\Omega}$

$$\Rightarrow \qquad \Delta l_o = \frac{mg}{2k\cos\Omega} \qquad (4.2)$$

A force now displaces the mass downward in the vertical direction by a small amount 'z' from the equilibrium position. The length and angle of the wire are changed to l' and Ω' and the tension in the wire due to gravitational loading also changes such that $T' = \dfrac{mg}{2\cos\Omega'}$. The tension is equal to $k\Delta l_o'$ where

$$\Delta l'_o = \frac{mg}{2k\cos\Omega} ' \tag{4.3}$$
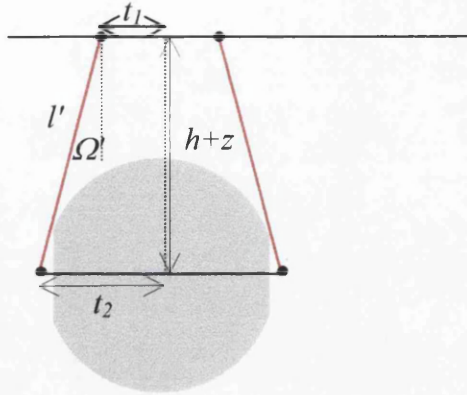
Figure (4.3): - *Face on view of cylindrical mass after displacement z.*

A restoring force will act on the mass, proportional to the extra extension Δl, where

$$\Delta l = l' - l_o - \Delta l'_o = (l' - l) + (\Delta l_o - \Delta l'_o) \tag{4.4}$$

after substitution for l_o from equation (4.1). The calculation of Δl is best carried out by considering the two terms separately. Using $l = \sqrt{h^2 + (t_2 - t_1)^2}$ and $l' = \sqrt{(h + z)^2 + (t_2 - t_1)^2}$ in the first term of equation (4.5) we obtain: -

$$l' - l = z\left(\frac{h}{l}\right) = z\cos\Omega \tag{4.5}$$

to first order in z.

Using $\Delta l_o = \dfrac{mg}{2k\cos\Omega} = \dfrac{mg}{2k\left(\dfrac{h}{l}\right)}$ and $\Delta l'_o = \dfrac{mg}{2k\cos\Omega '} = \dfrac{mg}{2k\left(\dfrac{h+z}{l'}\right)} \approx \dfrac{mg}{2k\left(\dfrac{h+z}{l - z\dfrac{h}{l}}\right)}$,

in the second term we obtain

$$\Delta l_o - \Delta l'_o = \frac{mg}{2k}\left(\frac{z\tan^2\Omega}{l}\right). \tag{4.6}$$

to first order in z. Simplification is achieved by the use of the binomial expansion and by discarding second and higher order terms. Putting these together gives: -

59

$$\Delta l = z\cos\Omega + \frac{mg}{2k}\left(\frac{z\tan^2\Omega}{l}\right)$$

(4.7)

The equation of motion in the vertical direction is: -

$$m\ddot{z} = -2k\Delta l\cos\Omega' \approx -2k\Delta l\cos\Omega \text{ to first order.}$$

(4.8)

Substituting for Δl from equation (4.6) gives: -

$$m\ddot{z} = -\left(2k\cos^2\Omega + \frac{mg\sin^2\Omega}{l\cos\Omega}\right)z$$

(4.9)

This is simple harmonic motion where $\ddot{z} = -(2\pi f)^2 z \Rightarrow$ the vertical frequency of a single pendulum, $f_{\text{vertical}} = \frac{1}{2\pi}\sqrt{\left(+\frac{2k\cos^2\Omega}{m} + \frac{g\sin^2\Omega}{l\cos\Omega}\right)}$

For the case of four wires the k in equation (4.9) would become $2k$, where k is again the spring constant of one wire.

In considering equation (4.9) it can be seen that there are two effects which determine to the frequency, one related to the spring constant k, and one to g. It is clear from the derivation that the first term arises due to the overall length change in the wires as the mass moves. It is however less obvious that there should be an additional term involving g. The Lagrangian model [82] predicted this term and the forces model allowed us to understand that it comes from a change in the angle, Ω, of the wires when the pendulum moves in the vertical direction. The same argument leads to an additional term arising in the rotational equation of motion, see equation (4.49).

4.4 Tilt and Longitudinal Motion

Firstly the mass is rotated through an angle, ϕ, to the vertical. Secondly the mass is displaced in the X-direction such that the wires move through an angle θ. ϕ is defined as the motion about the centre of mass. x_n is defined as the linear displacement of the centre of mass, x_1 is defined as the linear displacement of the line joining the wires to the mass and x_0 is defined as the linear displacement of the line joining the wires at the points of suspension (all in the X-direction).

(i)   Consider the case of a mass suspended from 2 wires of length, l, which are vertical when the mass is at rest and attached to the mass a distance, d above the line through the centre of mass.
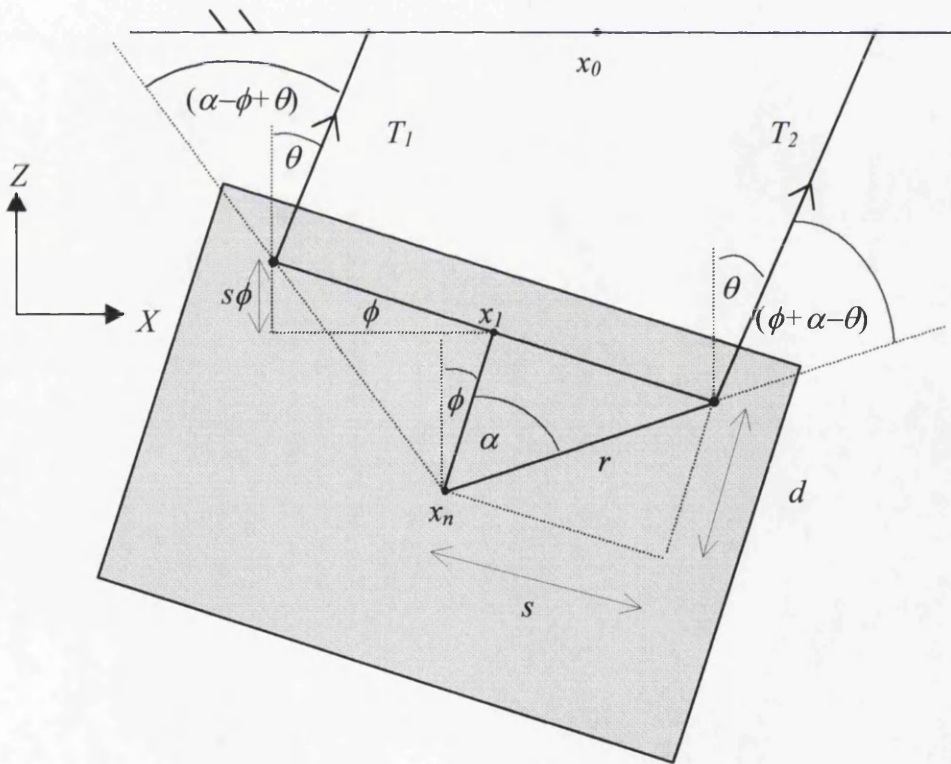
Figure (4.4): - *Side view of cylindrical mass.*

For small angles $\qquad \phi = \dfrac{x_n - x_1}{d}$ (4.10)

and $\qquad \theta = \dfrac{x_1 - x_0}{l}$. (4.11)

The component of restoring force which acts to tilt the mass for one wire $= T_2\sin(\phi - \theta + \alpha)$ and for the other wire $= T_1\sin(\alpha - \phi + \theta)$. T_2 and T_1 are the tensions in each wire such that: -

$$T_2 = \frac{mg}{2} + k\Delta l$$ (4.12)

and $\qquad T_1 = \dfrac{mg}{2} - k\Delta l$. (4.13)

where Δl is the change in vertical height as the mass tilts, equation (4.7). Now Torque $= (\underline{r}) \times (\underline{F}) = $ (distance)$\times$(perpendicular component of Force). Hence the equation of motion for tilt for a two wire suspension is: -

$$I_Y \ddot{\phi} = - T_2 r \sin(\phi - \theta + \alpha) - T_1 r \sin(\phi - \theta - \alpha)$$ (4.14)

where I_Y is the moment of inertia about the Y-axis. Expanding equation (4.14) for small angle $(\phi - \theta)$ and substituting for T_1 and T_2 where $\Delta l = z = s\phi$, for small angle, ϕ, for vertical wires, gives: -

$$I_Y \ddot{\phi} = -mgd(\phi - \theta) - 2ks^2\phi$$ (4.15)

where $d = r\cos\alpha$ and $s = r\sin\alpha$.

Now using equations (4.10) and (4.11) and solving for θ in terms of x_n and ϕ gives: -

$$\theta = \frac{x_n - x_0 - \phi d}{l}$$ (4.16)

substituting equation (4.16) into (4.15) gives: -

$$I_Y \ddot{\phi} = \frac{mgd}{l}(x_n - x_0) + \left(-mgd - \frac{mgd^2}{l} - 2ks^2\right)\phi$$ (4.17)

The longitudinal equation of motion is: -

$$m\ddot{x}_n = -mg\theta$$ (4.18)

substituting equation (4.16) into (4.18) gives: -

$$m\ddot{x}_n = -\frac{mg}{l}(x_n - x_0) + \frac{mgd}{l}\phi$$ (4.19)

It can be seen that equations (4.17) and (4.19) are coupled.

(ii)   Consider the case of a mass suspended from 2 wires as in case (i) and figure (4.4) but this time the wires are sloping at an angle, Ω, to the vertical in the Y-direction, in its equilibrium position, as in figure (4.1).

In this case equation (4.10) is the same as before but equation (4.11) becomes: -

$$\theta = \frac{x_1 - x_0}{l \cos\Omega} \qquad (4.20)$$

and subsequently equation (4.16) becomes: -

$$\theta = \frac{x_n - x_0 - \phi d}{l \cos\Omega} \qquad (4.21)$$

This time the equation of motion for tilt must take into account the fact that the wires are angled in the Y-direction. Thus component of forces acting vertically are $T_2 \cos\Omega$ and $T_1 \cos\Omega$ Hence: -

$$I_Y \ddot{\phi} = - T_2 r \cos\Omega \sin(\phi - \theta + \alpha) - T_1 r \cos\Omega \sin(\phi - \theta - \alpha) \qquad (4.22)$$

where $T_1 = \dfrac{mg}{2 \cos\Omega} - k\Delta l$ $\qquad (4.23)$

and $\quad T_2 = \dfrac{mg}{2 \cos\Omega} + k\Delta l$ $\qquad (4.24)$

expanding equation (4.22) for small angle $(\phi - \theta)$ and substituting for T_1, T_2 and Δl, from equation (4.7) where $\Delta l = z = s\phi$, gives: -

$$I_Y \ddot{\phi} = -mgd(\phi - \theta) - \frac{mgs^2 \sin^2 \Omega}{l \cos\Omega} \phi - 2ks^2 \cos^2 \Omega \phi \qquad (4.25)$$

where again $d = r\cos\alpha$ and $s = r\sin\alpha$

Substituting equation (4.21) into (4.25) gives: -

$$I_Y \ddot{\phi} = \frac{mgd}{l \cos\Omega}(x_n - x_0) + \left(-mgd - \frac{mgd^2}{l \cos\Omega} - \frac{mgs^2 \sin^2 \Omega}{l \cos\Omega} - 2ks^2 \cos^2 \Omega \right)\phi \qquad (4.26)$$

For the case of four wires the k in equation (4.26) would become $2k$, where k is again the spring constant of one wire.

Now substituting equation (4.21) into equation (4.18) gives the longitudinal equation of motion as: -

$$m\ddot{x}_n = - \frac{mg}{l \cos \Omega}(x_n - x_0) + \frac{mgd}{l \cos \Omega} \phi \qquad (4.27)$$

Firstly it can be seen when comparing equations (4.26) and (4.27) with equations (4.17) and (4.19) that for the case of vertical wires, $\Omega = 0$, equations (4.26) and (4.27) simplify to equations (4.17) and (4.19). Secondly as already mentioned it can be seen that both sets of equations are coupled. It is therefore necessary to calculate the eigenvalues from the matrix of the coupled equations, outlined below, in order to find the normal mode frequencies.

$$\frac{d^2}{dt^2}\begin{bmatrix}\phi \\ x_n\end{bmatrix} = \begin{bmatrix}k_{11} & k_{12} \\ k_{21} & k_{22}\end{bmatrix}\begin{bmatrix}\phi \\ x_n\end{bmatrix} = [\mathbf{A}]\begin{bmatrix}\phi \\ x_n\end{bmatrix} \qquad (4.28)$$

where $k_{11} = -\dfrac{mgs^2\sin^2\Omega}{I_Y l\cos\Omega} - \dfrac{mgd}{I_Y} - \dfrac{mgd^2}{I_Y\, l\cos\Omega} - \dfrac{2ks^2\cos^2\Omega}{I_Y}$,

$k_{12} = \dfrac{mgd}{I_Y l\cos\Omega}$,

$k_{21} = \dfrac{gd}{l\cos\Omega}$ and

$k_{22} = -\dfrac{g}{l\cos\Omega}$

$\Rightarrow$ the coupled tilt and longitudinal frequencies, $f_{\text{tilt/longitudinal}} = \dfrac{1}{2\pi}\sqrt{(abs(eig[A]))}$

where *abs* calculates the absolute value of the eigenvalues (*eig*) of *A*.

It can also be seen from both sets of equations that they become uncoupled when the distance, *d*, the wires break-off above the line through the centre of mass equals zero, implying the longitudinal motion, x_n, and tilt, ϕ, become uncoupled. Thus the coupling has a dependence on a non-zero value of *d*.

4.5 Rotation

Due to the complexity of the equation of motion for rotation four examples are set below. In all four of the cases the wires are assumed to break-off from the line through the centre of mass.

(i)   Consider the case of a mass, m, suspended by two wires of length, l, which are vertical.

If the mass rotates through an angle, σ, the wires therefore change through an angle, θ, where the point of attachment at the mass moves in the arc of a circle, shown as a dotted line in figure (4.5). The component of restoring force in the rotational direction due to one wire $= T\sin\theta \approx T\theta$ where T = tension in one wire $= \dfrac{mg}{2\cos\theta} \approx \dfrac{mg}{2}$ for small angle approximation.
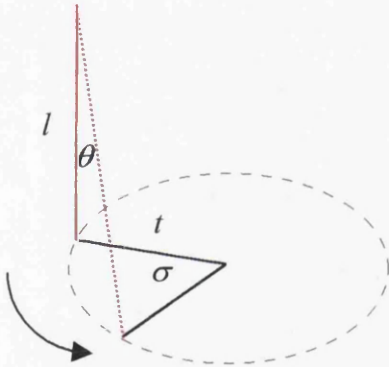
Figure (4.5): - *Effect on one wire when the mass is rotated through an angle, σ.*

Now Torque $= (\underline{r}) \times (\underline{F}) = $ (distance)×(perpendicular component of Force). Hence the equation of motion for a two wire suspension is: -

$$I_z \ddot{\sigma} = -2Tt\theta \qquad (4.29)$$

where $\theta = \dfrac{t\sigma}{l}$, I_z is the moment of inertia about the z-axis, t is the distance the wire is from the vertical line through the centre of mass.

$$\Rightarrow \quad I_z \ddot{\sigma} = -\frac{mgt^2}{l}\sigma \qquad (4.30)$$

(ii)   Consider the case of a mass suspended from four wires, which are vertical. Each wire is distance $(t^2 + s^2)^{1/2}$ away from the vertical line through the centre of mass, where s and t are the distances in the X and Y direction as shown below. By a similar argument to the above the equation of motion for a four wire suspension is: -

$$I_Z \ddot{\sigma} = -\frac{mg(t^2+s^2)}{l}\sigma \qquad\qquad (4.31)$$
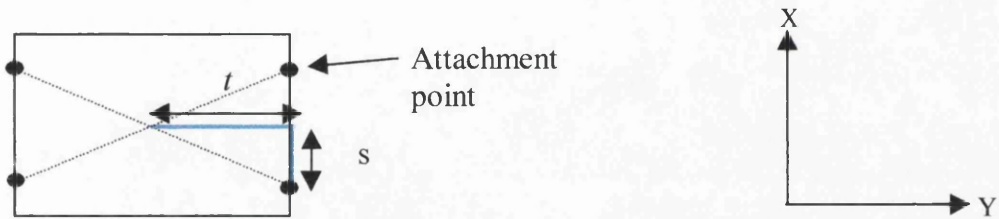
Figure (4.6): - *View of mass from above.*

(iii)   Consider the case of a mass suspended from two wires sloping in at an angle, Ω, to the vertical (Z-direction), as shown in figure (4.2). t_1 and t_2 are as defined before.
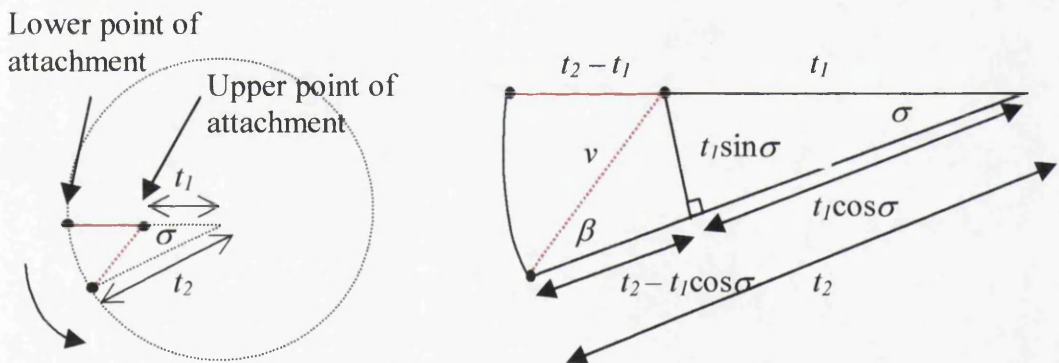
Figure (4.7): - *Projection onto X-Y plane looking from above.*

The dotted red line, in figure (4.7), represents the projected position of one wire after the mass rotates through an angle, σ. It can be shown that the length $v = t_2 - t_1$ assuming a small angle for σ. The component of tension, in the X-Y plane acting

66
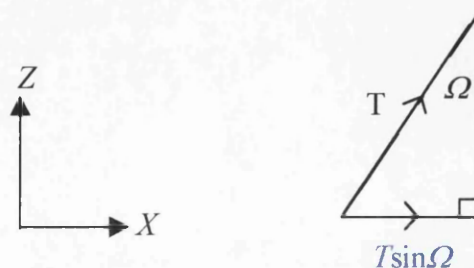
along direction $v = T\sin\Omega$ where $T = \dfrac{mg}{2\cos\Omega}$ and $\sin\Omega = \dfrac{(t_2 - t_1)}{l}$.

Now the component of this, which acts to rotate the mass, is the component in the direction perpendicular to the radius vector i.e. $T\sin\Omega \sin\beta$, where $\sin\beta = \dfrac{t_1}{t_2 - t_1}\,\sigma$ for small angle σ.

Therefore the torque for one wire $= (t_2)\times(T\sin\Omega \sin\beta)$. Implying: -

$$I_Z\ddot{\sigma} = -\frac{mgt_1t_2}{l\cos\Omega}\,\sigma \qquad\qquad (4.32)$$

(iv) Finally consider the case of four wires sloping in at an angle, Ω, to the vertical (Z-direction).

Figures (4.8) and (4.9) are a projection onto the X-Y plane looking from above. The solid line represents the mass. The dotted line represents the path on which the points of attachments move.
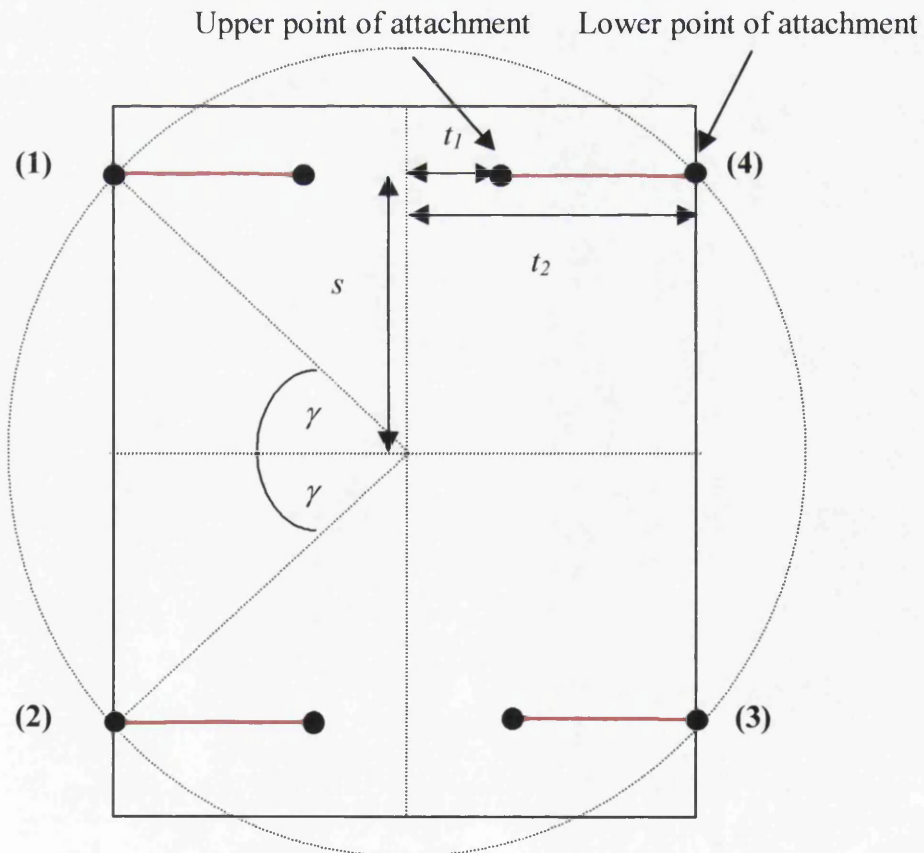
Figure(4.8): - *Before rotation.*
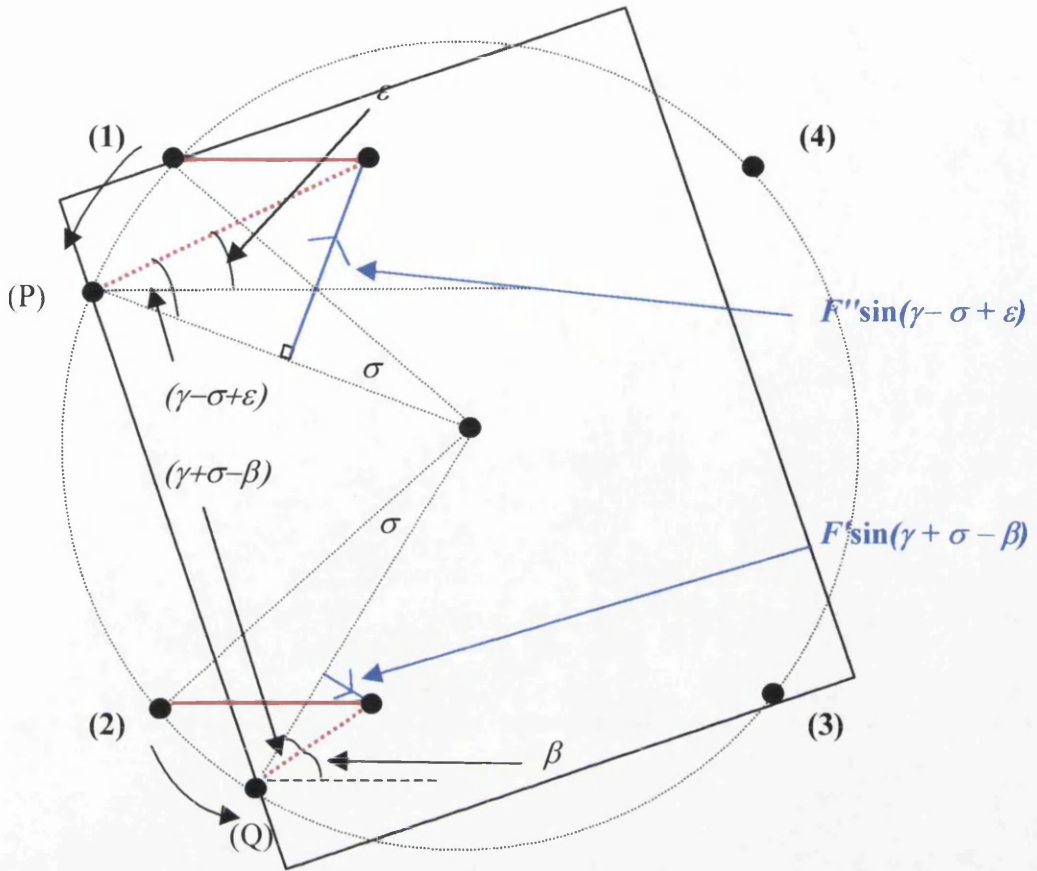
Figure(4.9): - *After rotation through a small angle, σ.*

The components of tensions, in the X-Y plane, in the wires **(1)** and **(2)** (dotted red lines) when the mass is rotated through a small angle, σ are given by F'' and F' respectively. The magnitude of the components of these tensions which are perpendicular to the radius and act to rotate the mass are shown in blue. These forces act at points (P) and (Q) respectively. Note that the resulting torques act in the opposite sense to each other.

Therefore the total torque from four wires is: -

$$2[\sqrt{t_2^2+s^2}][F''\sin(\gamma - \sigma + \varepsilon) - F'\sin(\gamma + \sigma - \beta)] \qquad (4.33)$$

where the factor of 2 takes into account all 4 wires.
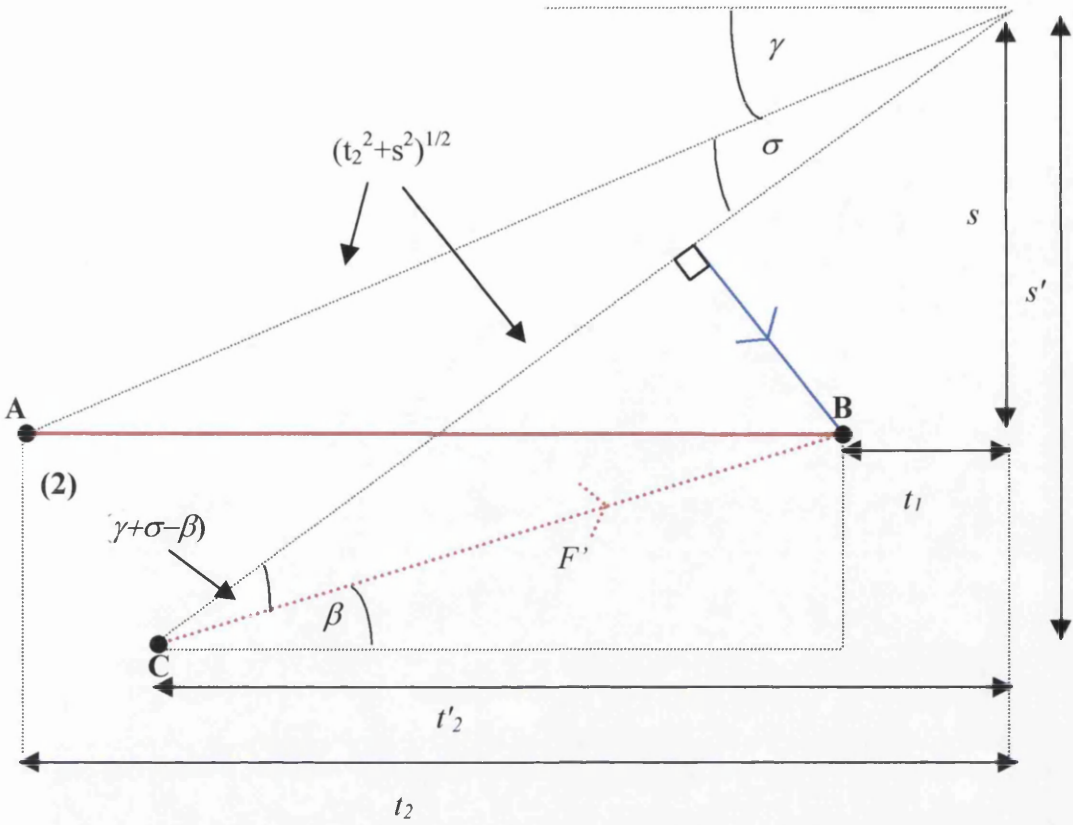
Figure (4.10): - *Figure (4.9) expanded for wire (2).*

Firstly an expression for $\sin(\gamma + \sigma - \beta)$ can be found from consideration of geometry, in figure (4.10).

Now
$$s' = \sin(\gamma + \sigma)\sqrt{t_2^2 + s^2} \qquad (4.34)$$

$$\Rightarrow \quad s' - s = (\sin(\gamma + \sigma) - \sin\gamma)\sqrt{t_2^2 + s^2} = t_2\sigma \quad \text{for small angle, } \sigma \qquad (4.35)$$

and
$$t'_2 = \cos(\gamma + \sigma)\sqrt{t_2^2 + s^2} \qquad (4.36)$$

$$\Rightarrow \quad t_2 - t'_2 = (\cos(\gamma) - \cos(\gamma + \sigma))\sqrt{t_2^2 + s^2} = s\sigma \quad \text{for small angle, } \sigma \qquad (4.37)$$

and hence
$$\tan\beta \approx \sin\beta = \frac{(s' - s)}{t_2 - t_1 - (t_2 - t'_2)} \approx \frac{t_2\sigma}{t_2 - t_1 - s\sigma} \qquad (4.38)$$

$$\Rightarrow \quad \sin(\beta - \sigma) \approx (\beta - \sigma) \approx \frac{t_1\sigma}{t_2 - t_1} \quad \text{discarding terms in } \sigma^2 \qquad (4.39)$$

$$\sin(\gamma - \beta + \sigma) = \sin(\gamma)\cos(\beta - \sigma) - \sin(\beta - \sigma)\cos(\gamma) = \left(\sin\gamma - \frac{t_1\cos\gamma}{t_2 - t_1}\sigma\right) \qquad (4.40)$$

for small angles.

It can be shown that $\sin(\gamma - \sigma + \varepsilon) = \left(\sin\gamma + \frac{t_1\cos\gamma}{t_2 - t_1}\sigma\right)$ using a similar argument for wire (1).

$$\Rightarrow \text{Total torque} = 2\sqrt{t_2{}^2+s^2}\left(F''\left(\sin\gamma + \frac{t_1\cos\gamma}{t_2-t_1}\sigma\right) - F'\left(\sin\gamma - \frac{t_1\cos\gamma}{t_2-t_1}\sigma\right)\right) \qquad (4.41)$$

Secondly expressions for F'' and F' can be found by considering the dynamics of the wires. Assuming the mass does not change vertical position and does not tilt, the wires have to change length by an amount Δl when the mass rotates through an angle, σ.

Before rotation: -   After rotation through σ (for wire (2)): -
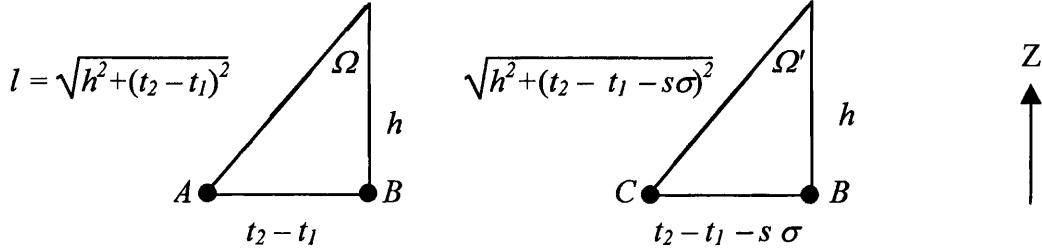
where $CB = \dfrac{(s'-s)}{\sin\beta} = t_2 - t_1 - s\sigma$ from equations (4.35) and (4.38)

$$\Delta l = \sqrt{h^2+(t_2-t_1-s\sigma)^2} - \sqrt{h^2+(t_2-t_1)^2} \qquad (4.42)$$

$$\Rightarrow \quad \Delta l \approx -\frac{s\sigma(t_2-t_1)}{\sqrt{h^2+(t_2-t_1)^2}} \qquad (4.43)$$

Wires (1) and (3) are stretched and (2) and (4) are contracted assuming the overall height is not changed. Thus the tensions in wires (1) and (2) are given by

$$T'' = \frac{mg}{4\cos\Omega} + k\Delta l \quad \text{and} \quad T' = \frac{mg}{4\cos\Omega} - k\Delta l \text{ respectively.}$$

wires (1) and (3): -   wires (2) and (4): -

$$F'' = T''\sin\Omega'' \qquad\qquad F' = T'\sin\Omega'$$
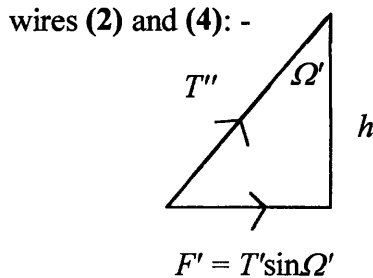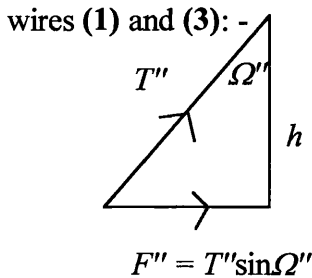
Finally from the geometry of the triangles shown above the components of force in the X-Y plane, F'' and F' are given by: -

$$F'' = T''\sin\Omega'' \qquad (4.44)$$

$$\text{and} \quad F' = T'\sin\Omega' \qquad (4.45)$$

where $\sin\Omega'' = \dfrac{t_2 - t_1 + s\sigma}{\sqrt{h^2 + (t_2 - t_1 + s\sigma)^2}} \approx \dfrac{t_2 - t_1}{l} + \dfrac{s\sigma\cos^2\Omega}{l}$ (4.45)

and $\sin\Omega' = \dfrac{t_2 - t_1 - s\sigma}{\sqrt{h^2 + (t_2 - t_1 - s\sigma)^2}} \approx \dfrac{t_2 - t_1}{l} - \dfrac{s\sigma\cos^2\Omega}{l}$ (4.46)

Now substituting for F'' and F' and Δl into equation (4.33)

$\Rightarrow$ total torque =

$$-2\sqrt{t_2^2 + s^2}\left[\frac{mg}{2l\cos\Omega}\left(\frac{s^2\cos^2\Omega + t_1 t_2}{(t_2^2 + s^2)^{1/2}}\sigma\right) + 2ks\left(\frac{(t_2 - t_1)^2}{l^2 + (t_2 - t_1)^2}\sigma\right)\frac{s}{(t_2^2 + s^2)^{1/2}}\right]$$ (4.48)

$\Rightarrow$ the equation of motion is: -

$$I_z\ddot{\sigma} = -\frac{mg}{l\cos\Omega}\left(s^2\cos^2\Omega + t_1 t_2\right)\sigma - \left(\frac{4ks^2(t_2 - t_1)^2}{l^2}\right)\sigma$$ (4.49)

$\Rightarrow$ rotational frequency, $f_{\text{rotation}} = \dfrac{1}{2\pi}\sqrt{+\dfrac{mg}{I_z l\cos\Omega}\left(s^2\cos^2\Omega + t_1 t_2\right) + \left(\dfrac{4ks^2(t_2 - t_1)^2}{I_z l^2}\right)}$

4.6 Sideways Motion and Roll

The sideways and roll frequency equations are derived in a similar manner to the longitudinal and tilt equations but are somewhat more complicated. They become coupled when either the wires are angled in the Y-direction or the break-off position is moved to above or below the line through the centre of mass. Consider the case of a mass suspended from two wires sloping at an angle, Ω, to the vertical (Z-direction). t_1, t_2 and d are as defined before.

Firstly an expression for the change in length of the wires, Δl, and also the change in angle of the wires, θ, as the mass moves, has to be found. This is achieved by considering separately the effect that roll and sideways motions have on the mass.

(a) Consider the effect of roll through an angle, ψ, on the length and angle of the wire.
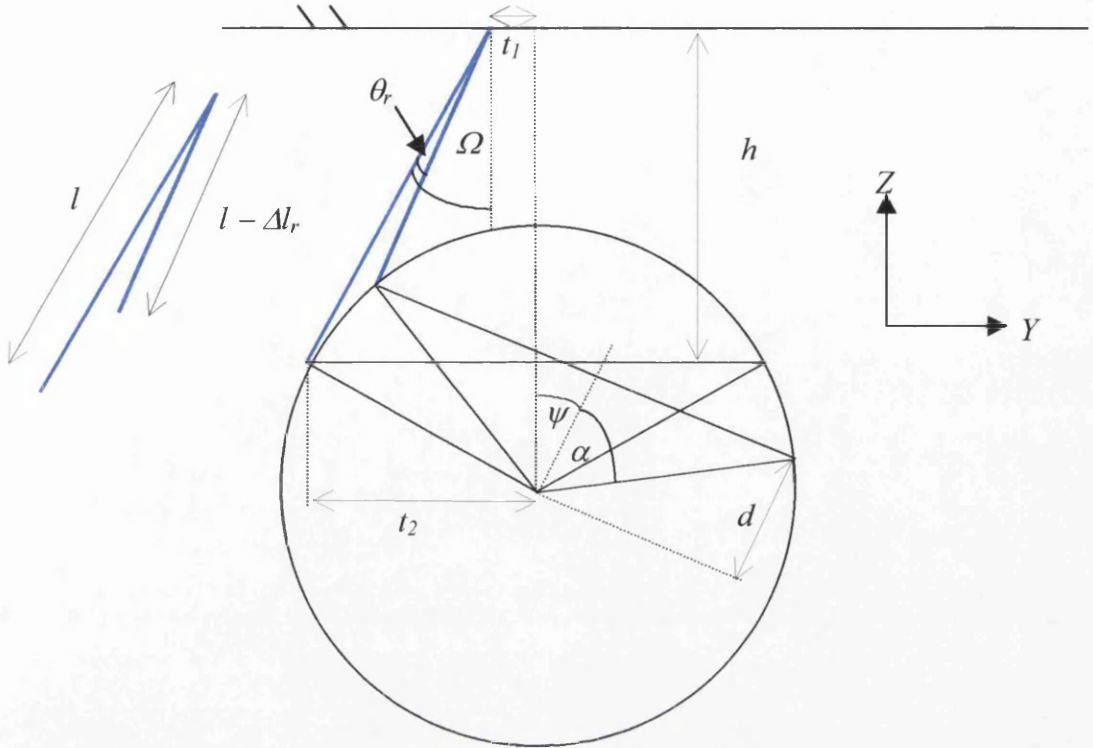
Figure (4.11): - *Face on view of cylindrical mass.*
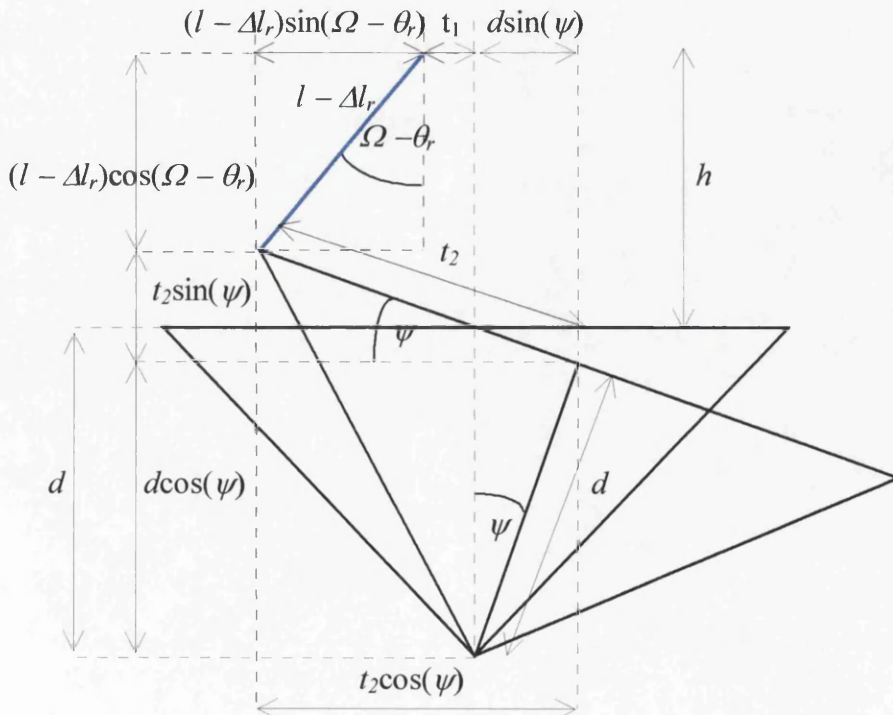
Figure (4.12): - *Figure (4.11) expanded to show various lengths.*

The mass is rotated through an angle, ψ, to the vertical. As a result, the angle Ω is decreased, on the left-hand side of figure (4.11), by an amount θ_r. Now

$$l\sin(\Omega) = t_2 - t_1 \qquad (4.50)$$

From figure (4.12) it is clear that: -

$$t_2\cos(\psi) = (l - \Delta l_r)\sin(\Omega - \theta_r) + t_1 + d\sin(\psi) \qquad (4.51)$$

$$\Rightarrow \quad (l - \Delta l_r)\sin(\Omega - \theta_r) = t_2\cos(\psi) - t_1 - d\sin(\psi) \qquad (4.52)$$

$$l\cos(\Omega) = h \qquad (4.53)$$

Again using figure (4.12) it is clear that: -

$$h = (l - \Delta l_r)\cos(\Omega - \theta_r) - d(1 - \cos(\psi)) + t_2\sin(\psi) \qquad (4.54)$$

$$\Rightarrow \quad (l - \Delta l_r)\cos(\Omega - \theta_r) = h + d(1 - \cos(\psi)) - t_2\sin(\psi) \qquad (4.55)$$

Expanding equations (4.52) and (4.55) for small angle θ_r and ψ, substituting for equations (4.50) and (4.53) and solving for Δl_r and θ_r gives: -

$$\Delta l_r = + t_2\cos(\Omega)\psi + d\sin(\Omega)\psi \qquad (4.56)$$

$$\theta_r = \left(-\frac{t_2\sin\Omega}{l} + \frac{d\cos\Omega}{l} \right) \psi \qquad (4.57)$$

The previous equations considered one side of the mass rotating. It can be shown that to first order the change in length and angle of the wires on the right hand side is identical to the change on the left-hand side of the mass.

(b) Consider the effect of a sideways movement, Δy on Δl and θ.
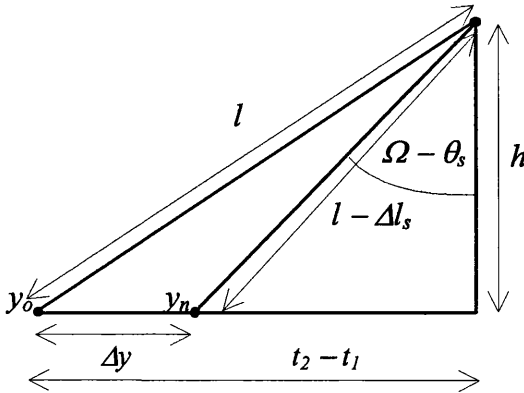
Figure (4.13): - *The effect of a sideways movement.*

Where $\Delta y = (y_n - y_0)$ $\qquad (4.58)$

Δy is defined as the linear displacement of the point of attachment on the mass from the rest position, y_0 to the new position, y_n. It can be shown that: -

$$\Delta l_s = \sin\Omega\,(y_n - y_0) \qquad (4.59)$$

and $\quad \theta_s = \cos\Omega \dfrac{(y_n - y_0)}{l}$ $\hfill$ (4.60)

Adding equations (4.56) and (4.57) to (4.59) and (4.60) respectively gives: -

$$\theta = \theta_s + \theta_r = \frac{\cos\Omega}{l}(y_n - y_0) - \left(\frac{t_2\sin\Omega}{l} - \frac{d\cos\Omega}{l}\right)\psi \hspace{1cm} (4.61)$$

$$\Delta l = \Delta l_s + \Delta l_r = \sin\Omega(y_n - y_0) + (t_2\cos\Omega + d\sin\Omega)\psi \hspace{1cm} (4.62)$$

Secondly the equations of motion for both the displacement of the centre of mass and motion about the centre of mass can be obtained as outlined below with reference to figure (4.14).
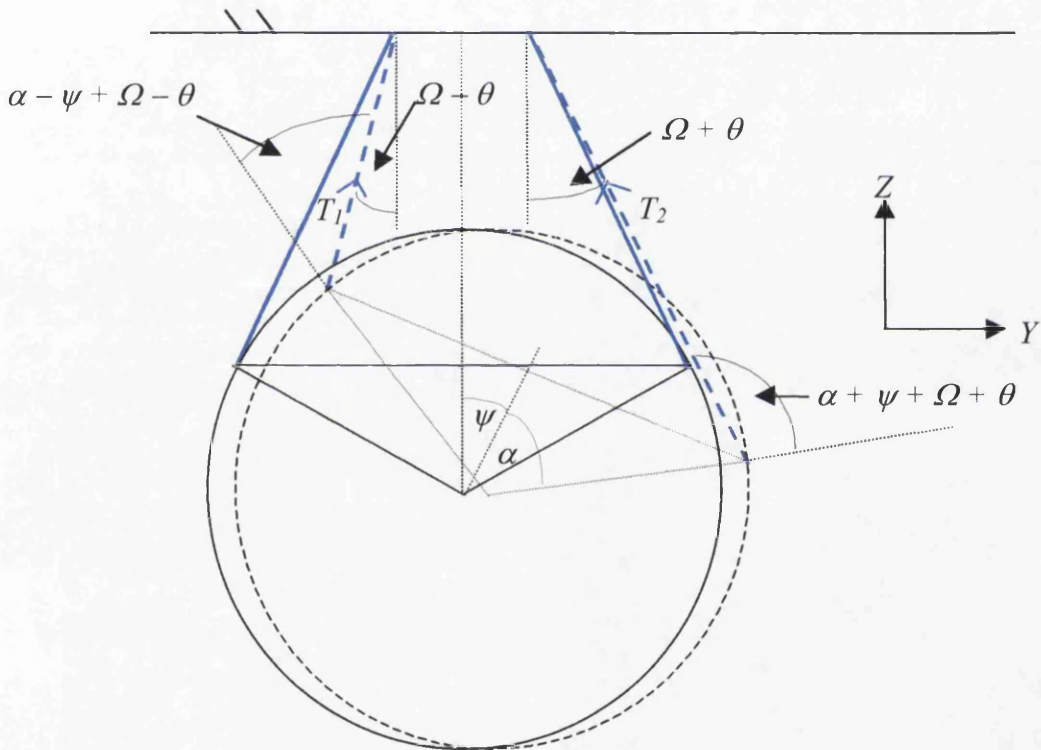
Figure (4.14): - *The effect of a sideways movement and roll.*

The equation of motion for the displacement of the centre of mass, y_n, is: -

$$m\ddot{y}_n = -T_2\sin(\Omega + \theta) - T_1\sin(\theta - \Omega) \hspace{1cm} (4.63)$$

The component of force which acts to roll the mass for one wire $= T_2 sin(\alpha + \psi + \Omega + \theta)$ and for the other wire $= T_1 sin(\alpha - \psi + \Omega - \theta)$ where T_2 and T_1 are as defined in equations (4.23) and (4.24).

Now Torque $= (\underline{r}) \times (\underline{F}) = $ (distance)$\times$(perpendicular component of Force). Hence the equation of motion for motion, ψ, about the centre of mass is: -

$$I_x \ddot{\psi} = -T_2 r \sin((\psi + \theta) + (\alpha + \Omega)) - T_1 r \sin((\psi + \theta) - (\alpha + \Omega)) \qquad (4.64)$$

$\Rightarrow$

$$I_x \ddot{\psi} = -T_2 r((\psi + \theta)\cos(\alpha + \Omega) + \sin(\alpha + \Omega)) - T_1 r((\psi + \theta)\cos(\alpha + \Omega) - \sin(\alpha + \Omega))$$

for small angle $(\psi + \theta)$.

Substituting for T_1, T_2 from equations (4.23) and (4.24), for Δl and θ from equations (4.61) and (4.62) and using small angle approximations gives: -

$$m\ddot{y}_n = \left(-\frac{mg\cos\Omega}{l} - 2k\sin^2\Omega \right)(y_n - y_0)$$

$$- \left(+\frac{mgd\cos\Omega}{l} - \frac{mgt_2\sin\Omega}{l} + 2kd\sin^2\Omega + 2kt_2\sin\Omega\cos\Omega \right)\psi \qquad (4.65)$$

and

$$I_x \ddot{\psi} = + \left(+\frac{mgt_2\sin\Omega}{\cos\Omega} - mgd + \frac{2mgdt_2\sin\Omega}{l} - \frac{mgd^2\cos\Omega}{l} - \frac{mgt_2^2\sin^2\Omega}{l\cos\Omega} \right)\psi$$

$$+ (-4kdt_2\sin\Omega\cos\Omega - 2kd^2\sin^2\Omega - 2kt_2^2\cos^2\Omega)\psi$$

$$+ \left(+\frac{mgd\cos\Omega}{l} - \frac{mgt_2\sin\Omega}{l} + 2kd\sin^2\Omega + 2kt_2\sin\Omega\cos\Omega \right)(y_n - y_0) \quad (4.66)$$

For the case of four wires the k in equations (4.65) and (4.66) would become $2k$, where k is again the spring constant of one wire.

As already mentioned the sideways and roll frequency equations are coupled. Therefore it is necessary to calculate the eigenvalues from the matrix of the coupled equations, outlined below, in order to find the normal mode frequencies.

$$\frac{d^2}{dt^2}\begin{bmatrix} \psi \\ y \end{bmatrix} = \begin{bmatrix} s_{11} & s_{12} \\ s_{21} & s_{22} \end{bmatrix}\begin{bmatrix} \psi \\ y \end{bmatrix} = [\mathbf{A}]\begin{bmatrix} \psi \\ y \end{bmatrix} \qquad (4.67)$$

where $s_{11} = +\dfrac{mgt_2\sin\Omega}{\cos\Omega\, I_X} - \dfrac{mgd}{I_X} - \dfrac{mgd^2\cos\Omega}{l\, I_X} - \dfrac{mgt_2^2\sin^2\Omega}{l\cos\Omega\, I_X} - \dfrac{2kd^2\sin^2\Omega}{I_X}$

$$+ \frac{2mgdt_2\sin\Omega}{l\, I_X} - \frac{4kdt_2\sin\Omega\cos\Omega}{I_X} - \frac{2kt_2^2\cos^2\Omega}{I_X},$$

$$s_{12} = +\frac{mgd\cos\Omega}{l\, I_X} - \frac{mgt_2\sin\Omega}{l\, I_X} + \frac{2kd\sin^2\Omega}{I_X} + \frac{2kt_2\sin\Omega\cos\Omega}{I_X},$$

$$s_{21} = -\frac{gd\cos\Omega}{l} + \frac{gt_2\sin\Omega}{l} - \frac{2kd\sin^2\Omega}{m} - \frac{2kt_2\sin\Omega\cos\Omega}{m} \text{ and}$$

$$s_{22} = -\frac{g\cos\Omega}{l} - \frac{2k\sin^2\Omega}{m}$$

$\Rightarrow$ the coupled sideways and roll frequencies, $f_{\text{roll/sideways}} = \dfrac{1}{2\pi}\sqrt{(abs(eig[A]))}$ where *abs* calculates the absolute value of the eigenvalues (*eig*) of *A*.

The equations of motion of a single pendulum, for all the degrees of freedom, are outlined in Appendix A.

4.7 Single Pendulum Analysis

4.7.1 Experimental results

To test the model, a single pendulum was set up on a four-wire suspension. The resonant frequencies were obtained by exciting the pendulum and measuring the response on a FFT spectrum analyser from an accelerometer attached to the mass. The table below shows the experimental results obtained for four different examples. The first case investigated had four straight wires breaking off from the centre of mass (case 1). Secondly the wires were angled in the Y-direction for two different angles (case 2 and 3). Finally the wires were attached to the mass above the line through the centre of mass (case 4). For all the cases the mass, m, $= 20$ kg.

The MATLAB [71] routine **mcsing.m** in Appendix A.1, model of a single pendulum, allows the input of the various pendulum parameters, assembles the single pendulum model, outlined in this chapter, and returns the theoretical mode frequencies for all degrees of freedom.

The first theoretical predictions were too high compared to the measured value for the frequencies where the spring constant dominated. The spring constant of the wire is given by: -

$$k = \frac{E\pi r^2}{l} \tag{4.68}$$

where E is the Young's Modulus, r is the radius of the wire and the other symbols have their usual meaning. In the first set of predictions the book value of Young's Modulus [83] of 2.0×10^{11} Pa was used. An attempt was then made to fit the theory using the measured vertical frequencies to calculate a new value for E. The new E was then used to predict the other frequencies. However this gave the theoretical

frequencies in tilt, rotation and roll as being too low compared to measured values. At this point it was postulated that some of the vertical frequencies might be affected by coupling to the support structure which was not completely rigid. Thus it was decided to independently measure E of the wire by measuring the vertical and rotational frequencies of a pendulum of 8 m in length. A long pendulum was used to minimise any coupling effect from its support structure. The measured frequencies gave a value for E of $\sim 1.7 \times 10^{11}$ Pa. Using this value the theoretical predictions agree with the measured results within experimental error, except for the vertical frequencies for case 1 and 2 where it was believed that the support structure was coupling to the pendulum, thus giving a lower frequency. The result table (4.1) below shows the revised theoretical predictions. The experimental values all have an error of ~ 10 %. The parameters outlined below for a single pendulum are all given in metres and are explained in figure (4.1).

Case 1: $l = 0.27$, $d = 0$, $s = 0.0405$, $t_1 = 0.133$, $t_2 = 0.133$

Case 2: $l = 0.2572$, $d = 0$, $s = 0.025$, $t_1 = 0.0465$, $t_2 = 0.133$

Case 3: $l = 0.395$, $d = 0$, $s = 0.025$, $t_1 = 0$, $t_2 = 0.133$

Case 4: $l = 0.363$, $d = 0.032$, $s = 0.025$, $t_1 = 0$, $t_2 = 0.133$

All in (Hz)	Tilt	Longitudinal	Roll	Sideways	Rotation	Vertical
Case 1 Experimental	7	0.94	20.3	0.94	1.78	11.25
Theory	7.6	0.96	22.2	0.96	1.78	14.3
Case 2 Experimental	4.39	1.0	19.4	1	1.9	11.9
Theory	4.5	1.01	21.8	1.01	2.02	13.74
Case 3 Experimental	3.58	0.81	16.1	0.8	1.26	10.2
Theory	3.6	0.82	17.6	0.8	1.37	11.1
Case 4 Experimental	3.88	0.84	18.5	0.84	1.44	11.4
Theory	3.9	0.85	19.9	0.8	1.5	11.4

Table (4.1): - *Results from single pendulum experiment*

4.7.2   Further investigation of the single pendulum model

As discussed in chapter 5, there are various constraints in the overall design of the suspension, such as for example the dimensions of the GEO 600 test masses and the overall length of the triple pendulum and the number of wires in each stage. However factors such as the separation of the wires in the X-direction and the angle of the wires in the Y-direction can be varied, and it is instructive to see how their variations affect the tilt and rotational frequencies.

Consider a GEO 600 test mass, for the main suspension, made from fused silica with a radius of 9 cm and thickness 10 cm giving a mass, m ~ 6 kg. The mass is suspended from four steel wires, of radius 200 μm, attached 1 mm above the line through the centre of mass.
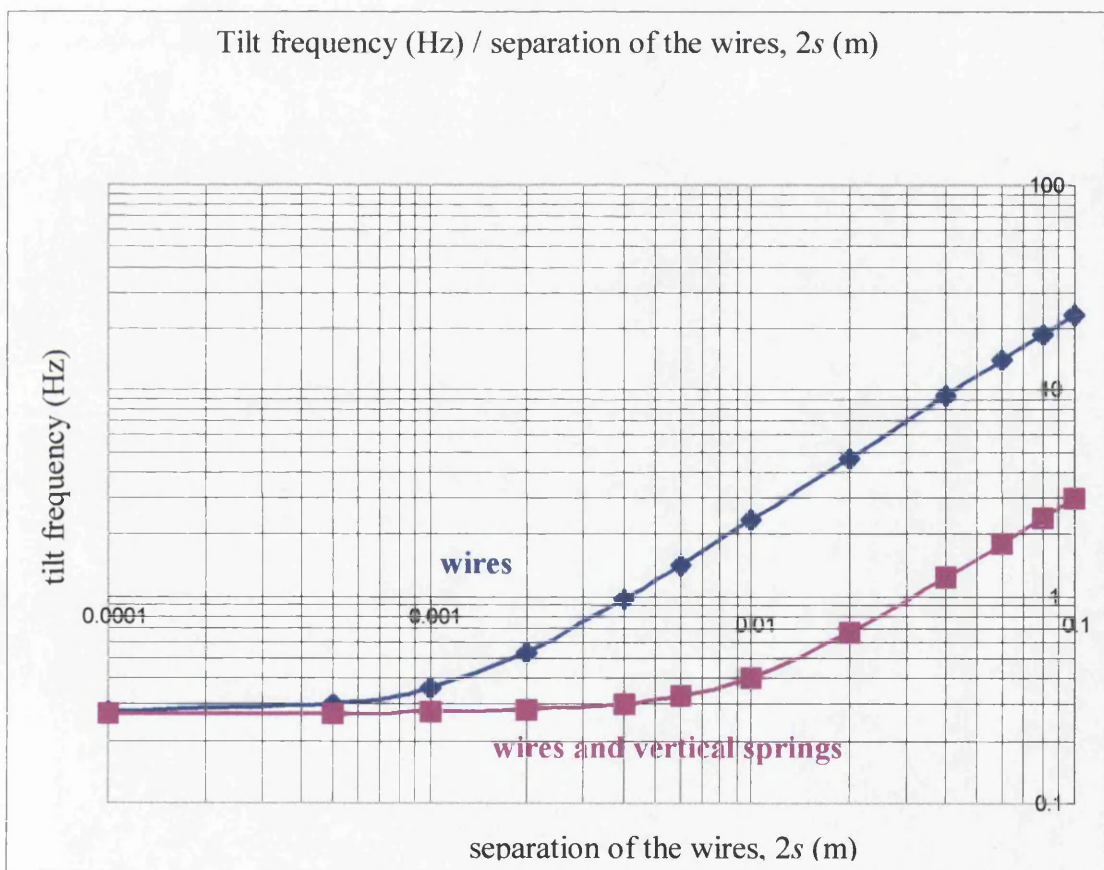
Figure (4.15): - *Graph of tilt frequency (Hz) / separation of the wires, 2s (m)*

Figure (4.15) shows how the tilt frequency is affected by varying the full separation of the wires in the X-direction, 2s, from 1 mm to 10 cm (the edge of the mass) for: -

- a four wire suspension

- and for a four wire suspension incorporating vertical springs of low spring constant and hence producing a lower tilt frequency to that of the four wires only.

The above case is for a separation in the Y-direction fixed at 18 cm and for four vertical wires of length 18 cm. It should be noted that the tilt and longitudinal frequencies are coupled. The mode, which is shown in figure (4.15), is the one that is dominated by the tilt motion. The two effects which contribute to the tilt frequency, namely the restoring forces due to gravity and the spring constant of the wire, can be clearly seen in both equation (4.17) and in figure (4.15). When the separation of the wires, s, in the X-direction, is small the tilt frequency is flat as a function of s and as the separation increases the tilt frequency varies linearly as a function of s.

Rotational frequency (Hz) / upper separation of the wires, t_1 (m)
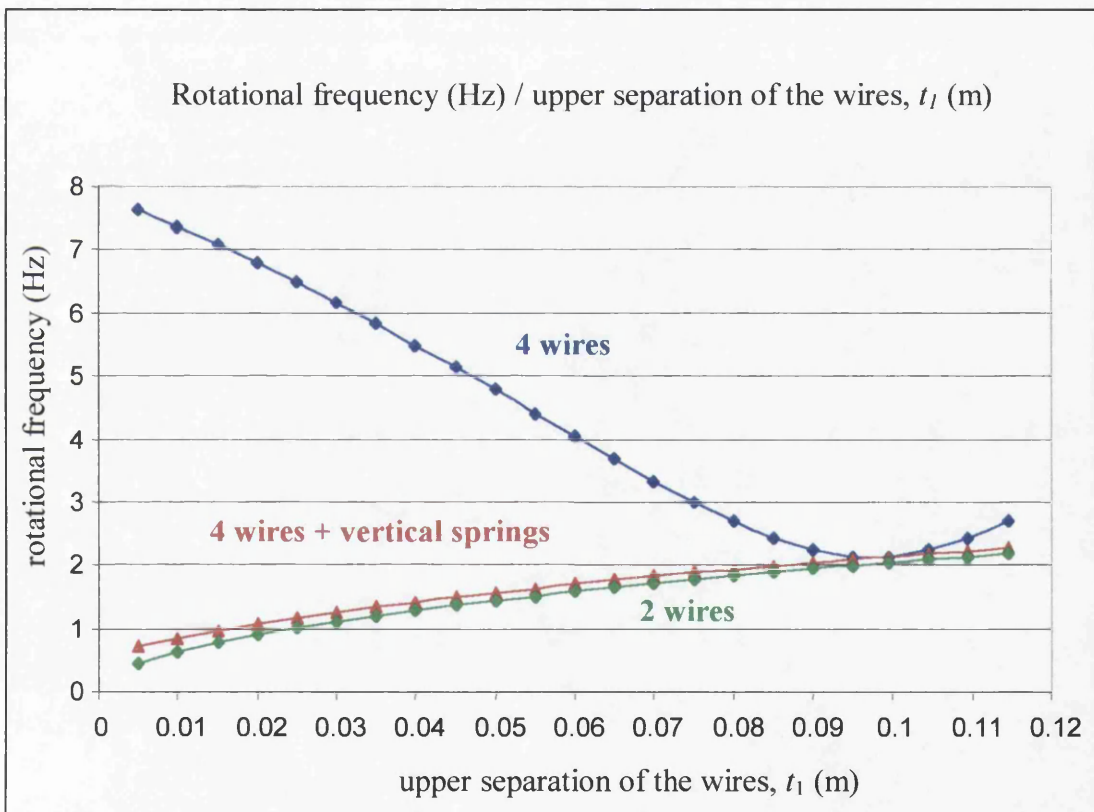
Figure (4.16): - *Graph of Rotational frequency (Hz) / upper separation of the separation of the wires, t_1 (m)*

Figure (4.16) shows how the rotational frequency is affected by the upper separation of the wires in the Y-direction, t_1, for $t_1 < t_2$, $t_1 = t_2$ and $t_1 > t_2$ where $t_2 = 0.095$: -

79

- for a two wire suspension, $s = 0$ (green)

- for a four wire suspension (blue)

- and for a four wire suspension incorporating vertical springs of low spring constant, k (red)

All of the above cases are for a fixed vertical height, of 18 cm, from the point of attachment of the wires on the mass to the point of attachment of the wires at the suspension point. For the four wire cases there is a fixed separation of the wires in the X-direction of 3 cm.

For the two wire case the rotational frequency decreases as the wires are angled in, in the Y-direction (i.e. as Ω and t_1 decrease). For the four wire case with a large separation of the wires in the X-direction the rotational frequency increases as the wires are angled in, in the Y-direction, see figure (4.16). However for the four wire and vertical spring case, again for the case of large separation of the wires in the X-direction, the rotational frequency decreases as the wires are angled in, in a similar way to that of the two wire case. This is explained by the fact that there are two effects that contribute to the rotational frequency, see equation (4.49). For the four wire case (blue) the spring term dominates whereas for the two wire case (green) there is only the gravitational term and the four wire and vertical spring case (red) the gravitational term dominates due to the small value of k.

It should be noted that for each graph an example of four wires incorporating vertical springs of low spring constant was included, in order to represent the effect that the cantilever spring blades have on the particular resonant frequencies of the pendulum. The information obtained from both graphs is used to facilitate the selection of the various parameters for a triple pendulum suspension, outlined in section 5.4.

Chapter 5

Triple Pendulum: analysis and Choice of Design

5.1 Introduction

The extension to a triple pendulum model from that of a single pendulum is outlined for both the vertical and the longitudinal-tilt degrees of freedom (section 5.2). The other degrees of freedom, sideways-roll and rotation, are obtained in a similar fashion and are shown in a final form in Appendix C.2. The next step is to add the active control to the triple pendulum model in order to design a working triple pendulum. This is done by firstly introducing the method of control modelling and secondly outlining the form of each triple pendulum model (section 5.3). With all of this in place the final choice of the various parameters of the triple pendulum for the main suspension for GEO 600 are described in detail (section 5.4).

5.2 Triple Pendulum Model

5.2.1   Vertical

The extension to a triple pendulum is outlined below for the vertical case. Firstly, as a reminder, the equation of motion in the vertical direction for a single pendulum is: -

$$m\ddot{z} = -\left(2k\cos^2\Omega + \frac{mg\sin^2\Omega}{l\cos\Omega}\right)z = -az, \quad \text{where } a = \left(2k\cos^2\Omega + \frac{mg\sin^2\Omega}{l\cos\Omega}\right). \quad [4.9]$$

The modelling of a triple pendulum, see figure (5.1), was developed from the equation of motion of a single pendulum.
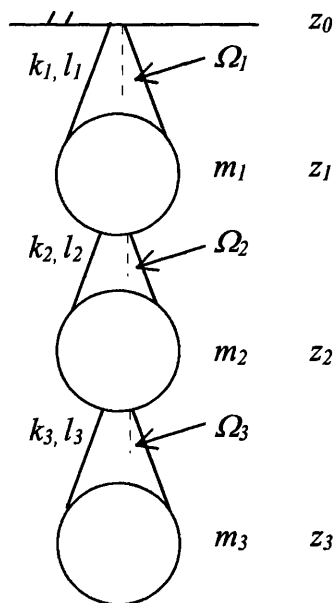
Figure (5.1): - *Face on schematic of a triple pendulum.*

The parameters used are: -

l_v = the length of a wire,

Ω_v = angle of the wires with respect to vertical in the Y-direction

m_v = the mass of each stage

and

k_v = the spring constant of a wire

where the subscript $v = 1, 2, 3$ for upper, intermediate and test mass respectively.

'z_ρ' ($\rho = 0,1,2,3$) represent a small excursion from the equilibrium position in the vertical direction. The extension of the wire of spring constant k_1 is: -

$$z_1 - z_0$$

Similarly the extensions of the wires of spring constant k_2 and k_3 are: -

$$z_2 - z_1$$

and $z_3 - z_2$ respectively.

The restoring force on m_3 depends only on $k_3 \Rightarrow$

$$m_3 \ddot{z}_3 = z_3 = -a_3(z_3 - z_2) \tag{5.1}$$

The restoring force on m_2 depends on both k_3 and $k_2 \Rightarrow$

$$m_2 \ddot{z}_2 = -a_2(z_2 - z_1) - a_3(z_2 - z_3) \tag{5.2}$$

The restoring force on m_1 depends on both k_1 and $k_2 \Rightarrow$

$$m_1 \ddot{z}_1 = -a_1(z_1 - z_0) - a_2(z_1 - z_2) \tag{5.3}$$

where

$$a_1 = \left(2k_1\cos^2\Omega_1 + \frac{(m_1+m_2+m_3)g\sin^2\Omega_1}{l_1\cos\Omega_1} \right) \tag{5.4}$$

$$a_2 = \left(2k_2\cos^2\Omega_2 + \frac{(m_2+m_3)g\sin^2\Omega_2}{l_2\cos\Omega_2} \right) \tag{5.5}$$

$$a_3 = \left(2k_3\cos^2\Omega_3 + \frac{m_3 g\sin^2\Omega_3}{l_3\cos\Omega_3} \right) \tag{5.6}$$

Thus

$$\ddot{z}_1 = -\left(\frac{a_1}{m_1} + \frac{a_2}{m_1}\right)z_1 + \left(\frac{a_1}{m_1}\right)z_0 + \left(\frac{a_2}{m_1}\right)z_2 \qquad (5.7)$$

$$\ddot{z}_2 = -\left(\frac{a_3}{m_2} + \frac{a_2}{m_2}\right)z_2 + \left(\frac{a_2}{m_2}\right)z_1 + \left(\frac{a_3}{m_2}\right)z_3 \qquad (5.8)$$

$$\ddot{z}_3 = -\left(\frac{a_3}{m_3}\right)z_3 + \left(\frac{a_3}{m_3}\right)z_2 \qquad (5.9)$$

5.2.2   Longitudinal motion and tilt

The extension to a triple pendulum is outlined below for the longitudinal-tilt case. Consider the case of a triple pendulum with each mass being suspended from two wires which are sloping at an angle, Ω_v, (where $v = 1,2,3$), to the vertical in the Y-direction. Each set of wires is attached a distance, d_t, (where $t = 0,1,2,3,4$) above or below the line through the centre of mass with a half separation of, s_q, in the X-direction (where $q = 0,1,2,3,4,5$). In the triple pendulum model, each set of wires for each stage is vertical in the X-direction implying that $s_0 = s_1 = Su$, $s_2 = s_3 = Si$, $s_4 = s_5 = Sl$ as outlined in Appendix B and figure (5.2).

As already mentioned, when obtaining the equations of motion for a single pendulum in the longitudinal-tilt direction (section 4.4) one considers the mass being rotated through an angle, ϕ, to the vertical and displaced in the X-direction such that the wires move through an angle, θ. For a triple pendulum this is true for each mass. ϕ_v is defined as the motion about the centre of mass (where $v = 1,2,3$), x_ω is defined as the linear displacement of the centre of mass (where $\omega = n,m,p$), x_e is defined as the linear displacement of the line joining the wires to the mass (where $e = 1,2,3,4,5$) and x_0 is defined as the linear displacement of the line joining the upper wires to the points of suspension, as outlined in figure (5.2).
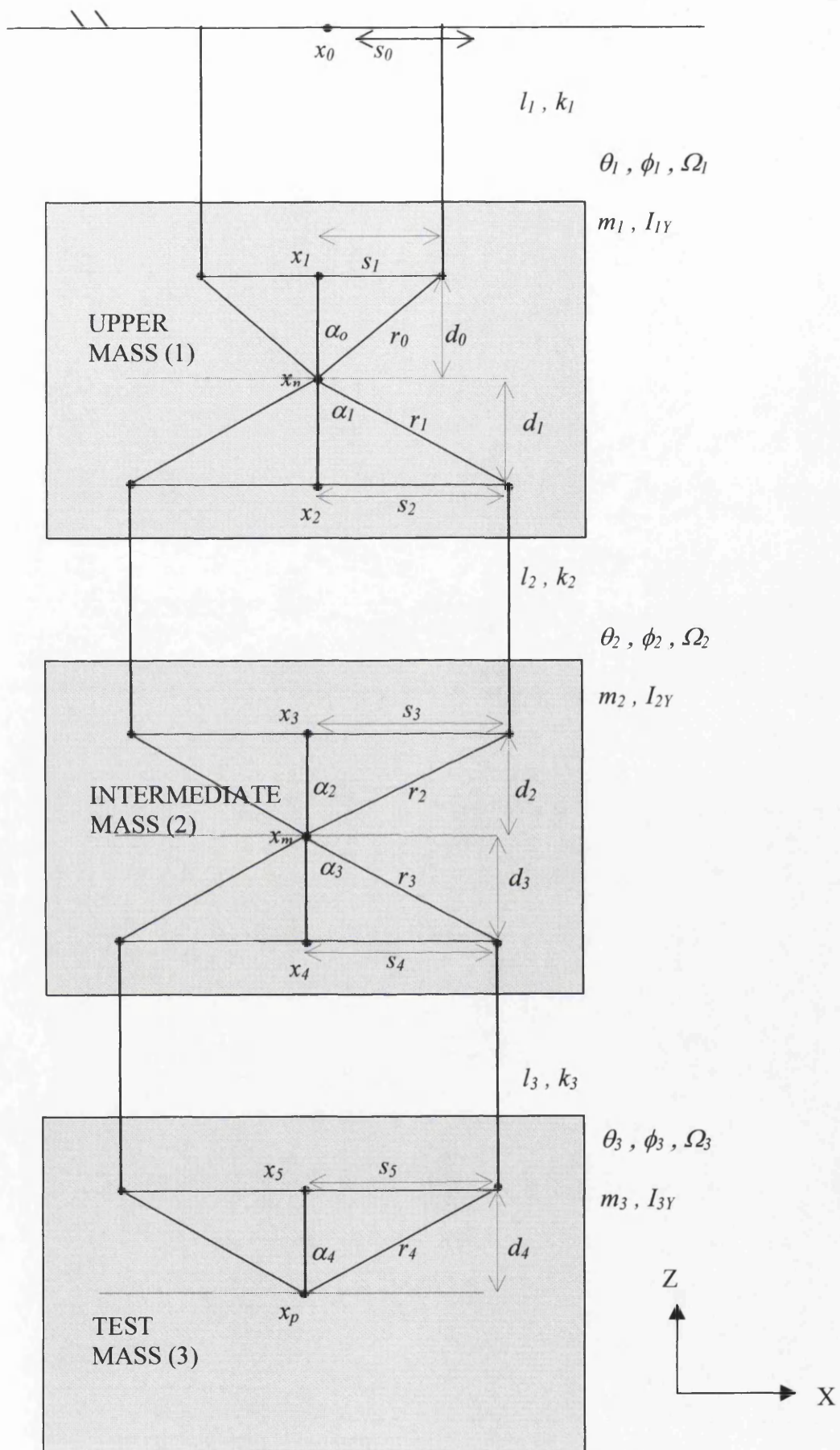
Figure (5.2): - *Schematic of triple pendulum from the side.*

Now for a single pendulum as in figure (4.4) the equations of motion for longitudinal and tilt (refer to section 4.4) are: -

$$m\ddot{x}_n = -mg\theta \qquad\qquad\qquad\qquad\qquad\qquad [4.18]$$

$$I_Y\ddot{\phi} = -mgd(\phi-\theta) - 2ks^2\cos^2\Omega\phi - \frac{mgs^2\sin^2\Omega}{l\cos\Omega}\phi \qquad [4.25]$$

where $\theta = \dfrac{x_n - x_0 - \phi d}{l\cos\Omega}$ \qquad\qquad\qquad\qquad [4.21]

The equations of motion for a triple pendulum are therefore: -

$$m_1\ddot{x}_n = -(m_1+m_2+m_3)g\theta_1 + (m_2+m_3)g\theta_2 \qquad (5.10)$$

$$m_2\ddot{x}_m = -(m_2+m_3)g\theta_2 + m_3g\theta_3 \qquad (5.11)$$

$$m_3\ddot{x}_p = -m_3g\theta_3 \qquad (5.12)$$

$$I_{1Y}\ddot{\phi}_1 = -(m_1+m_2+m_3)gd_0(\phi_1-\theta_1) - 2k_1s_0^2\cos^2\Omega_1(\phi_1) - (m_2+m_3)gd_1(\phi_1-\theta_2)$$

$$- 2k_2s_2^2\cos^2\Omega_2(\phi_1-\phi_2) - \frac{(m_1+m_2+m_3)gs_0^2\sin^2\Omega_1}{l_1\cos\Omega_1}(\phi_1)$$

$$- \frac{(m_2+m_3)gs_2^2\sin^2\Omega_2}{l_2\cos\Omega_2}(\phi_1-\phi_2) \qquad (5.13)$$

$$I_{2Y}\ddot{\phi}_2 = -(m_2+m_3)gd_2(\phi_2-\theta_2) - 2k_2s_2^2\cos^2\Omega_2(\phi_2-\phi_1)$$

$$- m_3gd_3(\phi_2-\theta_3) - 2k_3s_4^2\cos^2\Omega_3(\phi_2-\phi_3)$$

$$- \frac{(m_2+m_3)gs_2^2\sin^2\Omega_2}{l_2\cos\Omega_2}(\phi_2-\phi_1) - \frac{m_3gs_4^2\sin^2\Omega_3}{l_3\cos\Omega_3}(\phi_2-\phi_3) \qquad (5.14)$$

$$I_{3Y}\ddot{\phi}_3 = -m_3gd_4(\phi_3-\theta_3) - 2k_3s_4^2\cos^2\Omega_3(\phi_3-\phi_2) - \frac{m_3gs_4^2\sin^2\Omega_3}{l_3\cos\Omega_3}(\phi_3-\phi_2) \quad (5.15)$$

where $\quad \theta_1 = \dfrac{x_n - x_0 - \phi_1 \, d_0}{l_1 \cos\Omega_1}$, $\qquad\qquad\qquad\qquad$ (5.16)

$$\theta_2 = \dfrac{x_m - x_n - \phi_2 \, d_2 - \phi_1 \, d_1}{l_2 \cos\Omega_2} \qquad\qquad\qquad\qquad (5.17)$$

and $\quad \theta_3 = \dfrac{x_6 - x_m - \phi_3 \, d_4 - \phi_2 \, d_3}{l_3 \cos\Omega_3}$. $\qquad\qquad\qquad\qquad$ (5.18)

It is necessary, as it was with the single pendulum, to calculate the eigenvalues from the matrix of the coupled equations, outlined below, in order to find the six normal mode frequencies associated with the longitudinal-tilt direction.

$$\frac{d^2}{dt^2}\begin{bmatrix} x_n \\ \phi_1 \\ x_m \\ \phi_2 \\ x_p \\ \phi_3 \end{bmatrix} = \begin{bmatrix} k_{11} & k_{12} & k_{13} & k_{14} & k_{15} & k_{16} \\ k_{21} & k_{22} & k_{23} & k_{24} & k_{25} & k_{26} \\ k_{31} & k_{32} & k_{33} & k_{34} & k_{35} & k_{36} \\ k_{41} & k_{42} & k_{43} & k_{44} & k_{45} & k_{46} \\ k_{51} & k_{52} & k_{53} & k_{54} & k_{55} & k_{56} \\ k_{61} & k_{62} & k_{63} & k_{64} & k_{65} & k_{66} \end{bmatrix} \begin{bmatrix} x_n \\ \phi_1 \\ x_m \\ \phi_2 \\ x_p \\ \phi_3 \end{bmatrix} \qquad (5.19)$$

where the k_{ij} terms can be found in Appendix C.2.

5.2.3 Triple pendulum model

The equations of motion of a triple pendulum for the other degrees of freedom, sideways–roll and rotation, can be obtained using the same method as that outlined above for the longitudinal–tilt and the vertical cases. All of the degrees of freedom are outlined in **cit.m** in Appendix C.2. In chapter 4, it was mentioned that the theoretical modelling of a triple pendulum was carried out using two different techniques. Matt Husman and I worked on two separate theoretical techniques and were able to confirm that our models were consistent [82]. The mode frequencies for a triple pendulum can be obtained by running **modes.m** with both **cit.m** and **jbr.m**, for example, using MATLAB [71]. All of these files are outlined in appendix C.1 to C.3. The various input parameters for **jbr.m** are outlined in Appendix B.1 to B.3

5.3 State Space Modelling

5.3.1 Introduction

As already mentioned, it is not only the mode frequencies of a triple pendulum we are interested in. Understanding the dynamic response of the triple pendulum is also essential in order to, for example, model the effect of damping the pendulum mode frequencies. One method which can be used to calculate the response of a pendulum to a particular input is state-space modelling [84], which uses the following 1st order linear differential equations: -

$$\dot{x} = Ax + Bu \qquad\qquad (5.20)$$

$$y = Cx + Du. \qquad\qquad (5.21)$$

Here x is the state vector and u, y are the input and output vectors of the system. The D matrix allows straight through connection of an input to the output. This is not required for the following example and therefore the D matrix is set to zero, and will be ignored for the rest of this section.

Numerical packages, such as MATLAB [71], are readily available to model systems written in this form.

5.3.2 Example

As an illustration, consider a pendulum of mass, m, spring constant, k, and a damping force, $F = -b\dot{x}$. where b is a constant (viscous damping). The equation of motion is: -

$$m\ddot{x} + b\dot{x} + kx = F(t) \qquad\qquad (5.22)$$

where x is the displacement of the pendulum and $F(t)$ is an input force.

If you define one state variable as the position x and the other as the velocity, v then the equation can be written as: -

$$\dot{x} = v \qquad\qquad (5.23)$$

$$\text{and} \quad \dot{v} = -\frac{b}{m}v - \frac{k}{m}x + \frac{F(t)}{m} \qquad\qquad (5.24)$$

These first order linear differential equations can be written in matrix notation as follows: -

$$\dot{x} = \begin{pmatrix} \dot{x} \\ \dot{v} \end{pmatrix} = \begin{pmatrix} 0 & 1 \\ -\dfrac{k}{m} & -\dfrac{b}{m} \end{pmatrix} \begin{pmatrix} x \\ v \end{pmatrix} + \begin{pmatrix} 0 \\ 1 \end{pmatrix} \dfrac{F(t)}{m} \qquad (5.25)$$

$$\text{or} \qquad \dot{x} = Ax + Bu \qquad\qquad [5.20]$$

The eigenvalues of the A matrix would give the mode frequencies for the pendulum. Furthermore if you consider the output to be $y = v$, it is also possible to write this in matrix form: -

$$y = (\, 0 \quad 1\,) \begin{pmatrix} x \\ v \end{pmatrix} \qquad\qquad (5.26)$$

$$\text{or} \qquad y = (C) \begin{pmatrix} x \\ v \end{pmatrix} \qquad\qquad (5.27)$$

For the local control of the GEO 600 triple pendulum suspension the input force, $F(t)$, is produced by the action of a current carrying coil on a magnet attached to a mass, see section 5.4.3, and the outputs are displacements measured from a shadow sensor.

5.3.3   Triple pendulum model

The six degrees of freedom for the triple pendulum are divided into four models as follows: -

- Vertical, z — scz2.m
- Rotation, rz — scrz2.m
- Longitudinal, l, + tilt, rt, — sclrt2.m
- Sideways, t, + roll, rl, — sctrl2.m

These files are documented in Appendix C. The files read the ABCD matrices from **cit.m**, which in turn calls the input parameters from **jbr.m** (for example), see section 5.2.3. Each **2.m** file then calls **local.m**, the local control filter, which in turn calls several files from the Matlabf package written by Dr. Stuart Killbourn and internally documented [85]. The form of the local control filter is outlined in section 5.4.4. Each **2.m** file combines the ABCD matrices of the pendulum model

with the matrix representation of the local control in such a way so as to close the feedback loop.

There are varying numbers of inputs and outputs for each model. All of the inputs are to the upper mass while the outputs represent co-ordinates of each mass. As an example the longitudinal and tilt triple pendulum model incorporating closed loop local control is represented in the block diagram in figure (5.3). Both the closed loop transfer function and impulse response, for example, can now be obtained for each mass of the triple pendulum.
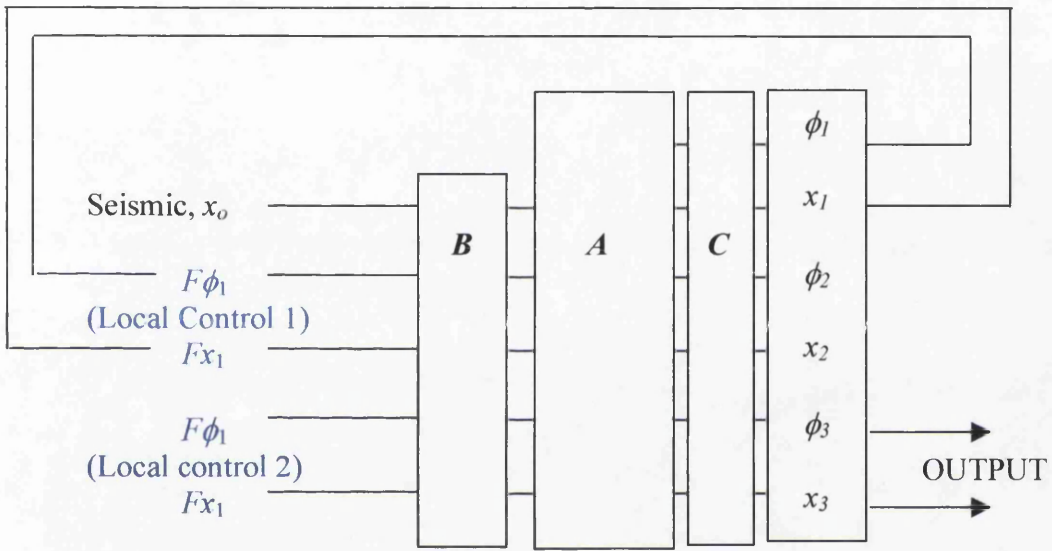
Figure (5.3): - *Block diagram of the state space representation of the triple pendulum in the longitudinal and tilt direction with the addition of local control.*

5.4 Triple Pendulum

5.4.1 Introduction

There are several key constraints already in place for the triple pendulum suspension, as outlined in section 2.6, which have to be taken into account before finalising the design and calculating the mode frequencies. Firstly the intermediate and test mass main optics are made from fused silica, each has dimensions 180 mm diameter by 100 mm thick giving a mass of ~ 6 kg, with four vertical fibres of fused silica between them. This design has been chosen to minimise the effects of thermal noise, as outlined in section 2.3. Secondly the low frequency resonant modes of the triple pendulum must be damped in a way that does not introduce excess noise at the test mass, as outlined in section 5.4.3. Some of the secondary constraints on the design include the fact that the test mass and its reaction mass, outlined in section 2.6, must be separated by approximately 3 mm, in the X-direction. As already mentioned, from the upper mass a double pendulum is suspended by four cantilever spring blades. The upper mass is 37 cm in the Y-direction and 10 cm in the X-direction, as shown in figure (5.3). The central mass in the upper mass, creating the 'T' shape, is necessary in order to lower the position of the centre of mass of the upper mass, thus making it possible to attach both sets of wires so that they break off 1 mm from the centre of mass, see section 5.4.2, as shown in figure (5.4). Further, in order to be able to apply orientation control of the test masses from the actuators on the upper mass, there must be four wires between the upper and intermediate mass.
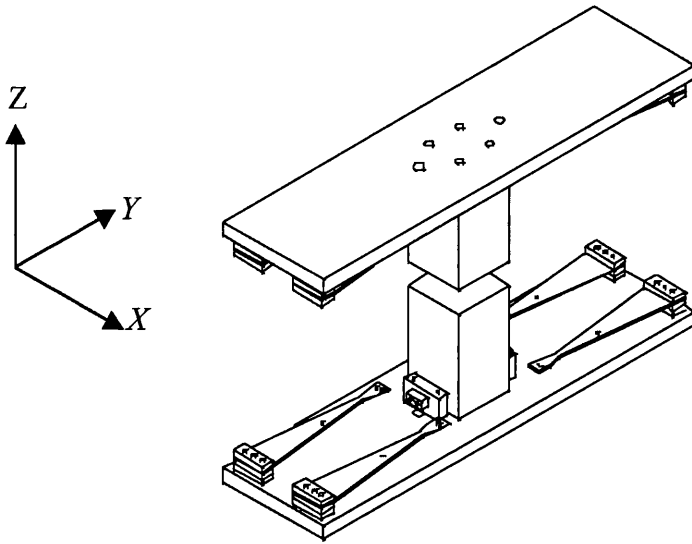
Figure (5.4): - *Two schematic views of the upper mass, looking from above and below.*

5.4.2 Triple pendulum parameters for the main suspension

With reference to Appendix B.1 and B.2, the following is a summary of the choice of parameters for the GEO 600 main triple pendulum suspension [86].

The upper stage has two steel wires ($s_1 = s_2 = su = 0$) suspended from two cantilevers and the intermediate stage has four steel wires ($s_2 = s_3 = si = 3$ cm) suspended from four cantilever blades. The parameters of each set of cantilever blades are outlined in section 6.5. The intermediate and upper wires are only tensioned to ~ 10 % of the breaking stress of carbon steel. This is chosen since the wires break off from the end of the cantilever blade and experiments at Glasgow have shown this safety factor was essential in order to ensure the stresses are reduced.

The lower stage has four straight fused silica fibres with a separation of 1 cm in the X-direction, this separation being chosen by consideration of both mechanical designs of the attachments and the need for a low tilt frequency, ($s_4 = s_5 = sl = 5$ mm and $\Omega_3 = 0$). The lower wires are tensioned to approximately one third of the breaking stress, the value of which has been measured by Dr. Sheila Rowan to be $\sim 8\times10^8$ Pa for typical fibres, suggesting the use of ~ 150 μm radius for each of the four fibres. This conservative estimate for the radius of the fibres was used in the

triple pendulum model. More recently Dr. Geppo Cagnoli, at Glasgow, has measured fibres with a breaking stress of 3 GPa, suggesting the use of four fibres of radius ~ 80 μm [55].

The choice of local control action on the upper mass places some constraints on the pendulum design. It is necessary to ensure that the modes of the triple pendulum that are to be damped couple to motion along at least one of the sensed directions of the upper mass. This coupling can be made strong enough by following two design principles: masses and moments of inertia about corresponding axes of each pendulum stage should be within a factor of ~ 2, and the stiffness of each stage should increase as you go down the pendulum. These constraints have been found to be simple to incorporate into the triple pendulum design and they are achieved by: -

- having all of the break off points as 1 mm with respect to the line through centre of mass ($d_0=d_1=d_2=d_3=d_4=1$ mm) (chosen to provide a stable system),
- selecting approximately the same mass in each stage (~ 6 kg),
- ensuring approximately the same moment of inertia about the equivalent axis,
- having the wires for the upper stage angled in, in the Y–direction ($\Omega_1 \sim 1.4^\circ$)
- suitable choice of the wire length for each stage ($l_1 = 42$ cm, $l_2 = 18.5$ cm and $l_3 = 28$ cm).

As already mentioned in section 5.2.3, the theoretical mode frequencies for the GEO 600 main triple pendulum suspension are obtained by running **modes.m** with both **jbr.m** and **cit.m** giving: -

Normal mode	Model prediction (Hz)					
Tilt / longitudinal	3.3	2.6	2.15	1.33	0.55	0.6
Roll / sideways	37	3.55	2.5	1.33	1.15	0.6
Rotation		3.15	1.55	0.4		
Vertical		26	4.2	1.25		

Table (5.1): - *Mode frequencies for the GEO 600 main triple pendulum suspension.*

A schematic of the mode shapes for the tilt and longitudinal modes is shown in figure (5.5). The frequencies can all be seen to be less than 5 Hz apart from the

vertical and roll frequencies of the final stage, outlined in blue, which lie between 20 and 40 Hz. These modes couple weakly to the main interferometer signal. These frequencies are left undamped in the present set-up as they occur too near the gravitational wave band for sufficient attenuation of electronic noise that would be associated with the use of the present design of local sensor. However they are only weakly excited by ground noise because they are isolated by the stacks and the two upper pendulum stages. As already mentioned, the final stage of suspension is on fused silica fibres to minimise thermal noise effects [50,51] and does not therefore incorporate soft vertical springs, as used in the upper two stages to give low vertical frequencies. Such springs would degrade the thermal noise.
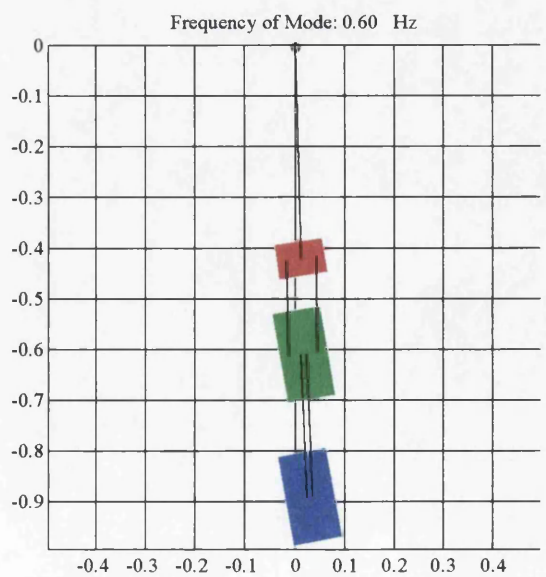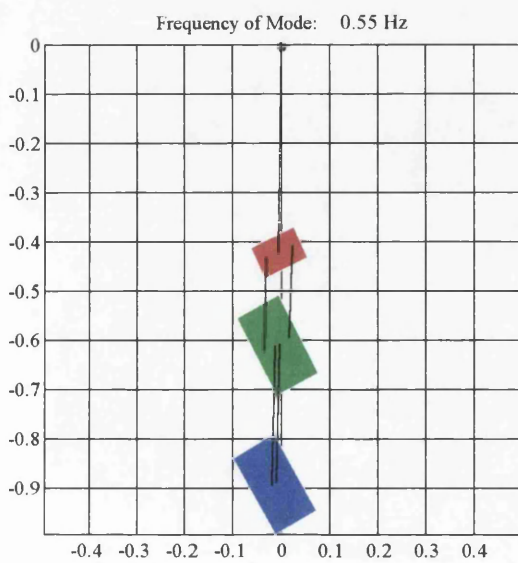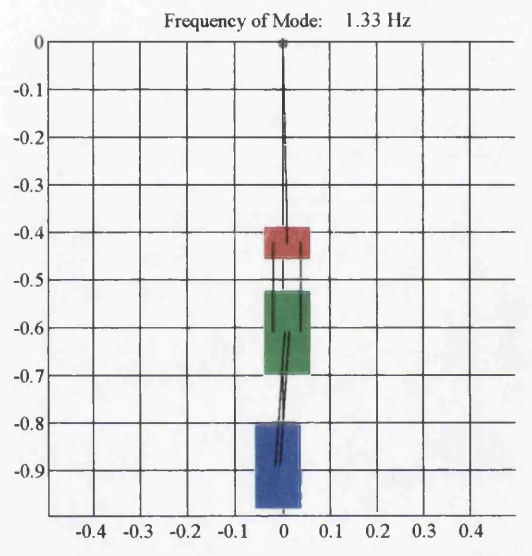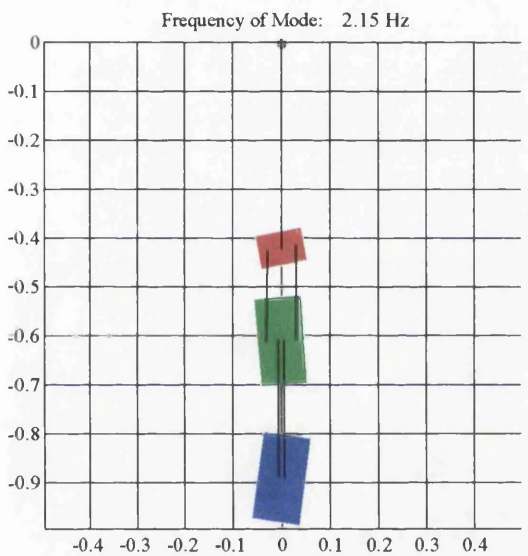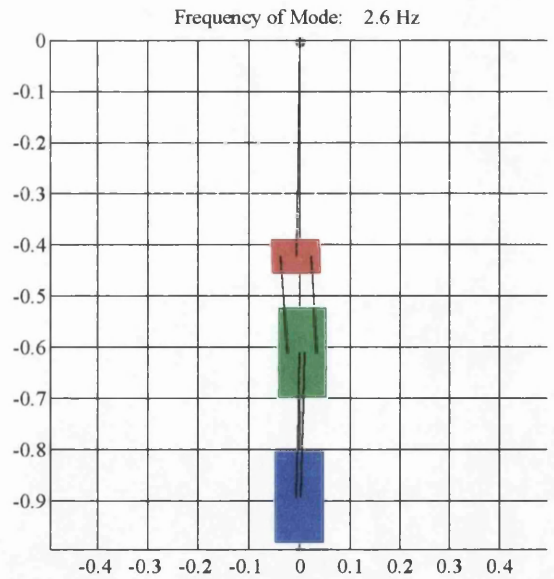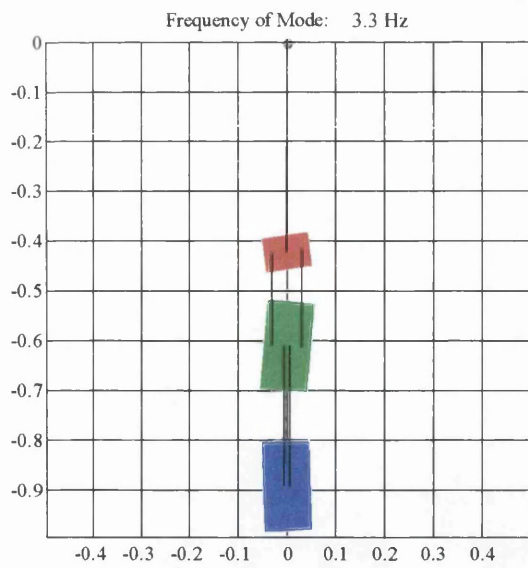
Figure (5.5): - *Schematic of the mode shapes for the tilt and longitudinal modes.*

5.4.3 Damping of the triple pendulum
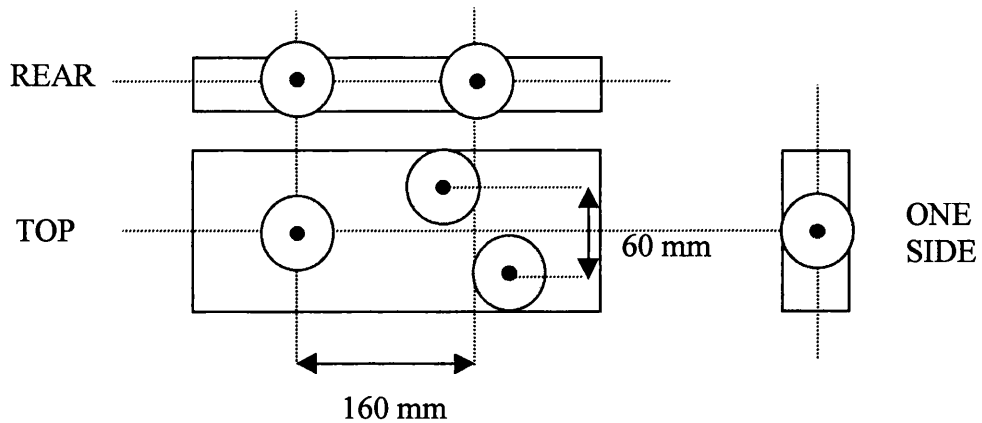
Figure (5.6): - *Schematic of positioning of sensors and actuators on upper mass.*

The local control of the triple pendulum is provided in six degrees of freedom between the rotational stage and the upper mass [85]. Applying the active damping at the upper mass ensures that the test mass is isolated from local control noise by the double pendulum below. The active damping system uses co-located sensing and damping, as described in section 3.4. The damping of the longitudinal and rotational modes is done by placing the sensors/actuators symmetrically on the long rear side of the upper mass. After careful modelling the damping was optimised with spacing for the coils of 16 cm, as shown in figure (5.6). The sensor/actuator for sideways damping is placed on one of the short sides with the remaining sensors/actuators for tilt and vertical damping placed on the top of the upper mass, as shown in figure (5.6). This gives an optimised balance of damping in all degrees of freedom. The channel gains should then all be within a few dB of each other, apart from the sideways gain which should be ~ 6 dB more as there is only one sensor/actuator for damping sideways motion. The magnets are again fixed with Ceramabond 571S to the upper mass and the sensors and actuators, housed in a vacuum-sealed glass encapsulation, are mounted on a rigid structure, which is attached to the rotational stage and extends down to the upper mass, as shown in figure (6.20) on page 124.

The theoretical damping performance of each mass of the triple pendulum is shown in figure (5.7). All of the modes can be seen to be strongly damped within a few

seconds. A comparison between the theoretical and experimental damping of the pendulum modes is outlined in section 6.7.
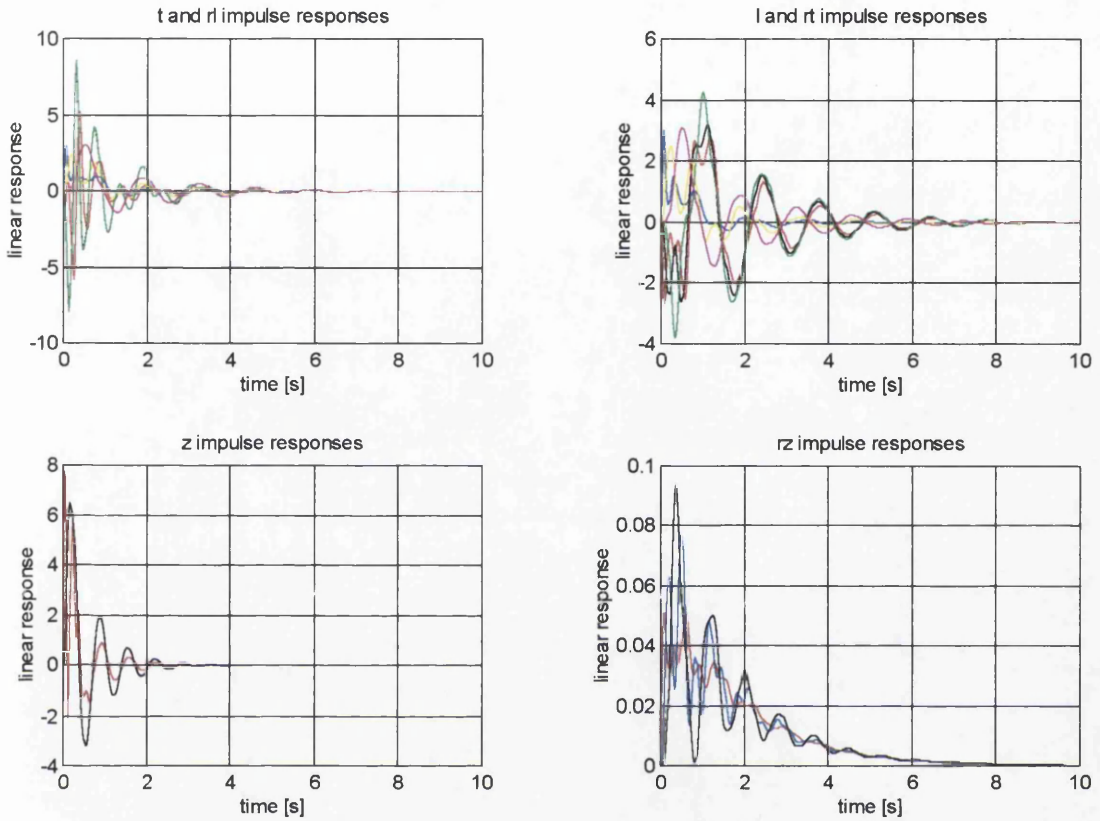
Figure (5.7): - *Theoretical impulse response of all six local control channels (sideways, t, roll, rl, longitudinal, l, tilt, rt, vertical, z, rotation, rz). The motion of each mass is shown for each degree of freedom. (The units of the response can be considered to be arbitrary.)*

5.4.4 Local control transfer function

This work follows closely that done by Dr. Stuart Killbourn on a double pendulum [59] and it was carried out mainly by Dr. Ken Strain. The local control transfer function was selected in order to meet certain requirements. Firstly, as already mentioned, all the low frequency (< 5 Hz) modes of the triple pendulum had to be actively damped. Secondly, as closely as possible, the same circuit layout developed for the local control of the mode-cleaner (designed by Dr. David Robertson and Dr. Stuart Killbourn) had to be used.

The transfer function of the local control for damping the triple pendulum for the main suspension is designed as a series connection of the following units: -

- gain factor (outlined in section 5.4.3)
- high pass filter at 0.7 Hz
- transitional differentiator (real zero and real pole) from 0.35 Hz to 0.8 Hz
- transitional differentiator (real zero and real pole) from 2 Hz to 14 Hz

In addition in order to reduce the control noise at high frequencies the following are used: -

- three Scultété two pole low pass + zero filter
  1. poles at 18 Hz, Q ~ 3, zero at 26 Hz
  2. poles at 24 Hz, Q ~ 4, zero at 50 Hz
  3. poles at 28 Hz, Q ~ 5, zero at 55 Hz
- low pass filter at 9 Hz

The zero at 26 Hz is intended to coincide with the undamped vertical mode, table 5.1. It should be noted that this frequency is dependent on the final choice of radius, r of the fused silica fibres in the final stage. At the time of writing the radius of the fibres were expected to be 150 μm.

5.5 Conclusion

A dynamic model for a triple pendulum has been obtained for all six degrees of freedom. The dynamics have been verified by checking each term with Matt

Husman's Lagrangian model. Further the method of controlling the triple pendulum has been introduced. It is now possible to predict, for example, the mode frequencies or the step response of a triple pendulum. The design parameters of the GEO 600 main test mass suspension are introduced, the full list of parameters are documented in Appendix B.3. In Chapter 6 both the mode frequencies and the step response of the Glasgow prototype pendulum are compared with the theoretical predictions from the model.

Chapter 6

Prototype Suspension in Glasgow for GEO 600

6.1 Introduction

The various stages of the GEO 600 main suspension system have been tested in Glasgow. Firstly a prototype single layer passive stack was tested for its isolation properties (section 6.2). Three of these prototype stacks were then interfaced with the stack stabiliser and rotational stage, the design of which is outlined in section 6.3. Secondly a prototype triple pendulum suspension was interfaced with the stacks and rotational stages, as shown in figure (6.1 (a)). Aluminium masses of the same mass and outer dimensions as the fused silica masses to be used in the final design were used for the intermediate and test masses, as shown in figure (6.1 (b)). Steel wires were used to suspend each stage. The equations required to design a cantilever blade are introduced (section 6.4) in order to choose the parameters of the two sets of blades for the triple pendulum. Each set of blades was used to suspend a single pendulum in order to test their predicted performance (section 6.5). The purpose of this prototype was to test the theoretical mode frequencies (section 6.6) and to test the performance of the local control for the triple pendulum (section 6.7). All of the parameters for the prototype suspension are outlined in Appendix B.4. A schematic showing both the side and face-on views of the triple pendulum suspension is in Appendix B.1 and B.2.
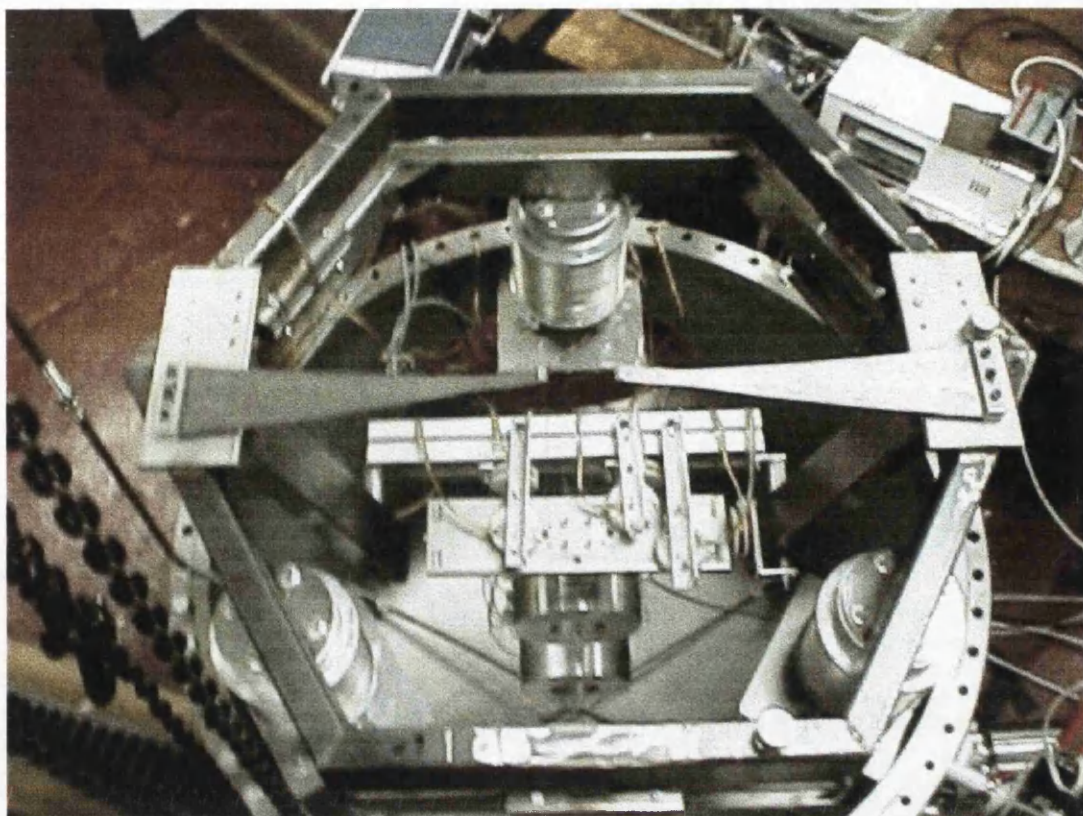
Figure (6.1): - *Photograph of the Glasgow prototype suspension (a) view from above.*
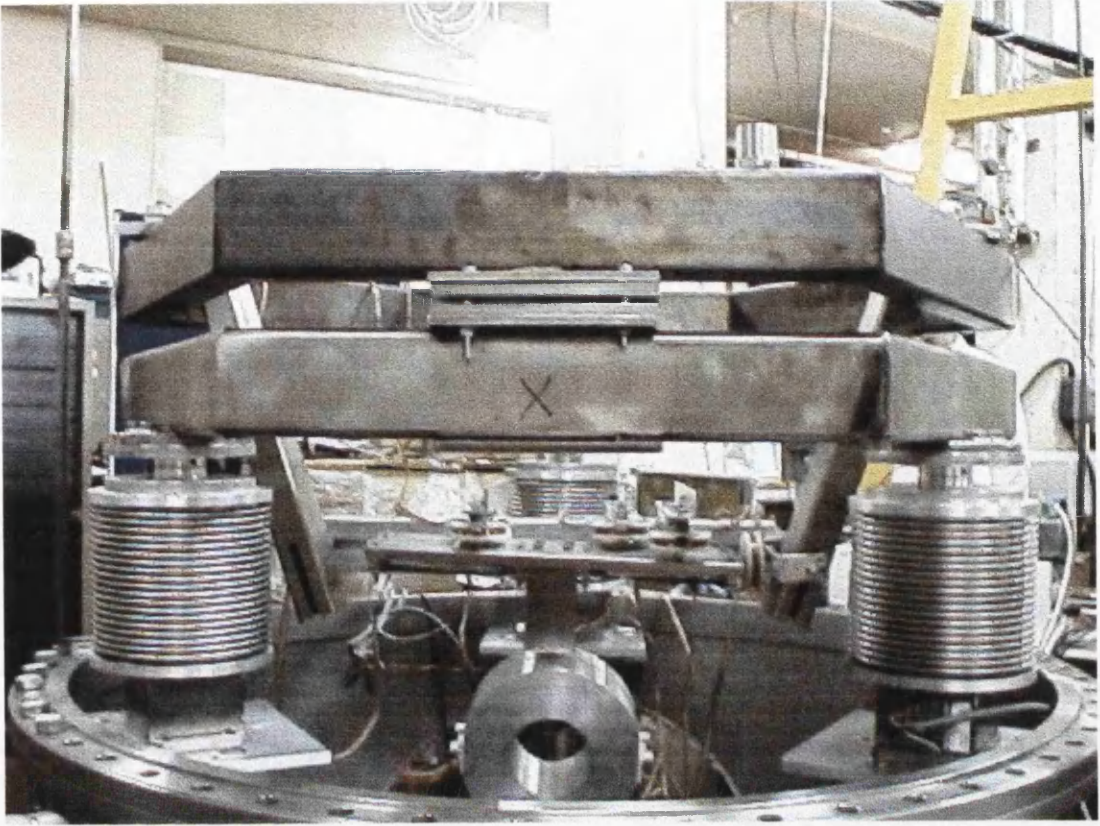
Figure (6.1): - *Photograph of the Glasgow prototype suspension (b) side view.*

6.2 Isolation Stack

As described in section 2.6, each isolation stack consists of two layers, the lower layer of which is active and the upper layer is passive. In the prototype suspension the piezoelectric transducer in the active layer, outlined in section 2.6, are used to drive the various stages in the vertical direction for studying transfer functions.
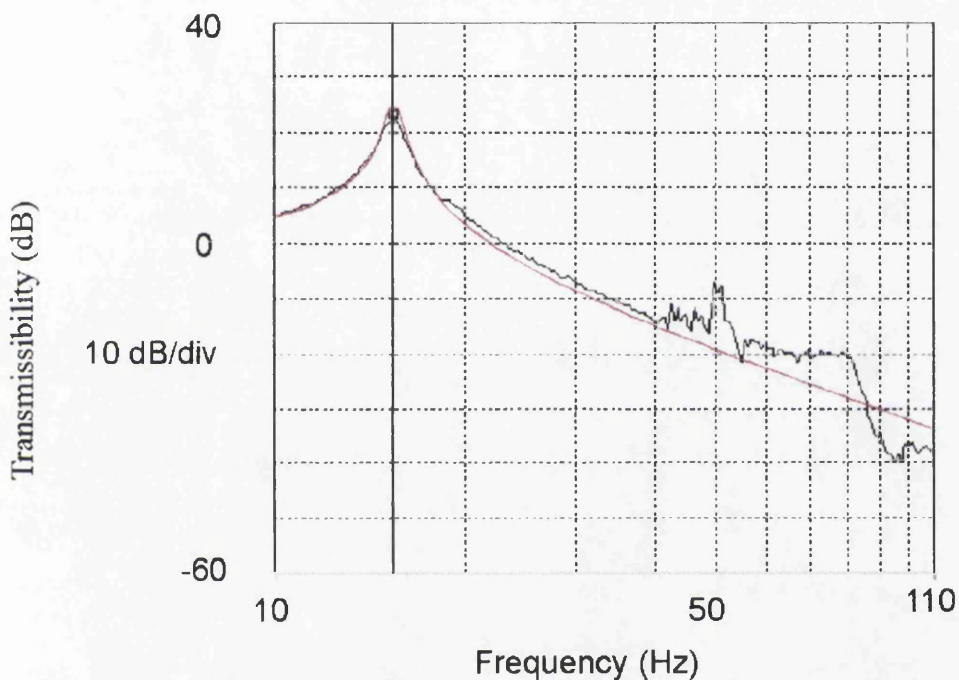
Figure (6.2): - *Vertical transfer function of a single layer prototype stack leg (red: - theoretical, black: - experimental).*

The design of the single layer passive stack is based on the work done for the two layer passive stack for the mode-cleaner suspensions, as outlined in section 3.2. A single passive layer is used rather than a double layer in the main suspension in order to provide improved static stability given that there is also an active layer which has a spring constant in the stack. The passive stack can be designed to have a vertical frequency at 15 Hz, with a 20 kg load. Experiments at Glasgow, using the same set-up as that outlined in section 3.2, have shown that a vertical attenuation of ~ 18 dB at

50 Hz can be achieved with this single passive layer, as shown in figure (6.2). Again a theoretical vertical transfer function was plotted with MATLAB [71], and is shown as the red curve in figure (6.2). The peak at 50 Hz corresponds to electrical mains interference. Further, the horizontal transfer function of the single layer passive stack has been measured to have a horizontal attenuation of ~ 30 dB at 50 Hz.

6.3 Stack stabiliser / Rotational stage

6.3.1 Design

The stack stabiliser and rotational stage, introduced in section 2.6, are very similar in design. Both must meet certain requirements. Firstly the stack stabiliser must rigidly attach to the three isolation stacks to provide static stability. Secondly the rotational stage must be able to support the triple pendulum suspension, without flexing. This implies that both have to be relatively rigid. Lastly the rotational stage must be able to rotate with respect to the stack stabiliser in order to allow initial alignment of the optics in the interferometer, see figure (6.3)
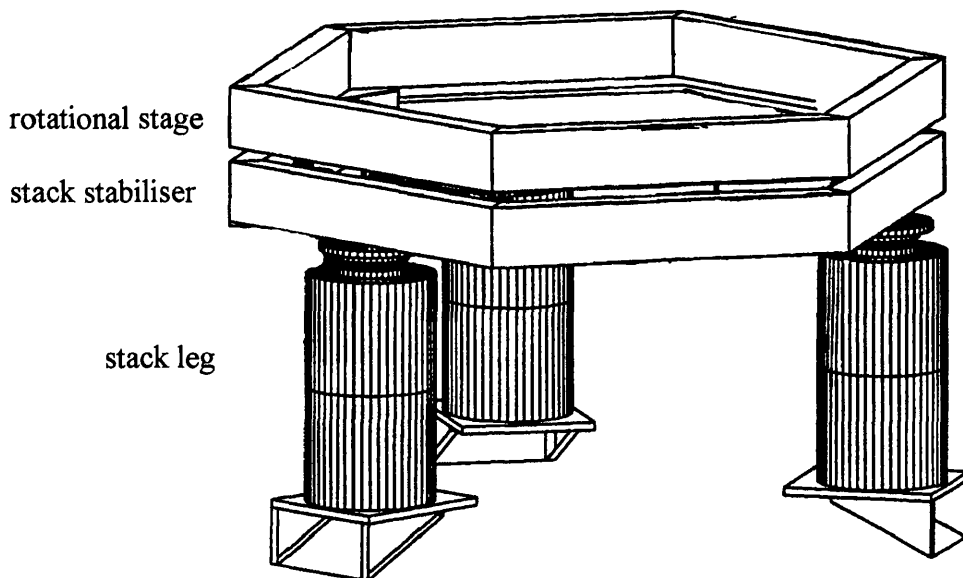
Figure (6.3): - *A schematic of the stack stabiliser and rotational stage. The figure also shows a schematic of the three stack legs.*

6.3.2 Finite element analysis

Finite element analysis of the design was carried out again using I–DEAS [72]. The boundary conditions which were implemented were that the co-ordinates of the points of attachment of the stacks were rigidly constrained in three dimensions.

The investigation of several designs was carried out, with the hexagonal box-section structure shown in figure (6.3) chosen as the optimum design. The box section has dimensions 40 mm broad by 80 mm deep with 2 mm thick walls. Sections of stainless steel box-section are welded together to form each structure. The steel has to be annealed, to relieve the stresses within the material and allow for ease of welding. The first flexural mode resonance was found to be at 480 Hz. The experimental resonance was also found for one of the structures. This was obtained by hanging the structure as a single pendulum, driving it with a vertical shaker, and measuring the resonances on an oscilloscope using an accelerometer. The first resonance was found to be at 400 Hz. This ties up fairly well with the I-DEAS [72] prediction as the structure used in the experiment also included steel clamps, used for attachment of cantilevers, which were not modelled, and which contributed to an extra 5 kg added to the original mass of 20 kg.

6.4 Design of Cantilever Blades

6.4.1 Introduction

The greater part of the work on cantilever blades in Glasgow [86] has been adapted from designs used by the VIRGO group.

As already mentioned, in order to enhance the vertical isolation, two vertical spring stages are included in the triple pendulum. Two blades are fixed onto the rotational stage and support the upper mass. Four blades then suspend a double pendulum from the upper mass. The blades are constructed from maraging (precipitation hardened) steel of the type Marval 18, which is low carbon steel with a high tensile stress.

There are three important parameters to consider when designing a cantilever spring stage in order to provide improved vertical isolation in the low frequency region (i.e. up to 50 Hz): -

1. The uncoupled vertical mode frequency, f_s [A] (associated with that particular spring stage).

2. The lowest flexural (internal) mode frequency, $f_{int.}$

3. The maximum permissible stress at the support point, $\sigma_{max.}$

All of these parameters are dependent on the width, length and thickness of the blade.

[A] The frequency observed for a spring in a particular stage supporting only the mass of that stage.

6.4.2 Manufacture
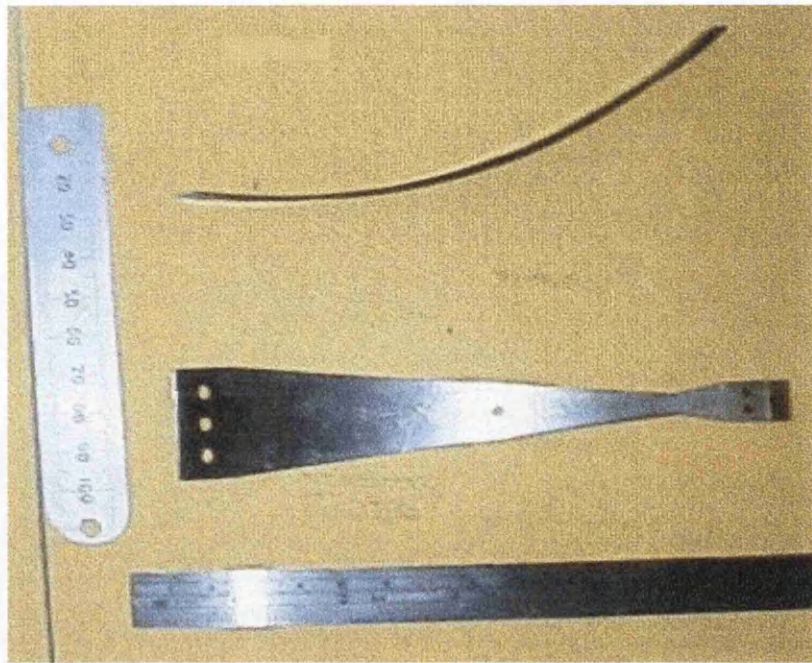
Figure (6.4): - *Geometry of the lower GEO 600 blades.*
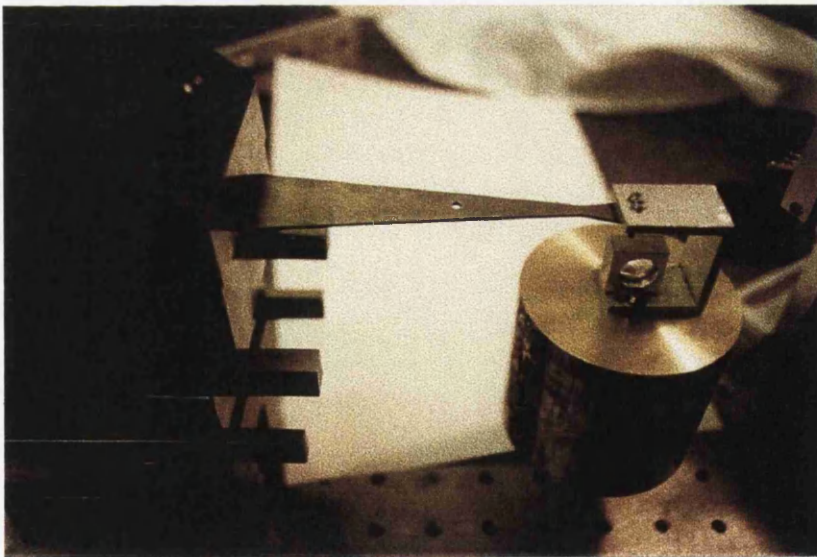
Figure (6.5): - *Photo of lower GEO 600 blades under load (JILA).*

Figure (6.4) above shows the GEO 600 lower blade geometry. A set of such blades was manufactured recently in JILA in Boulder, Colorado, with designs supplied by Dr. Mike Plissi. The manufacturing process starts with a section of steel being rolled into the correct radius of curvature. The pre-stressed steel is then cut to the desired shape, approximately trapezoidal. Finally the blade is aged for four hours at 480 ^{O}C. The blades become flat under load as shown in figure (6.5).

6.4.3 Blade specifications

Consider a blade pre-stressed into a curve, which becomes flat under load: -
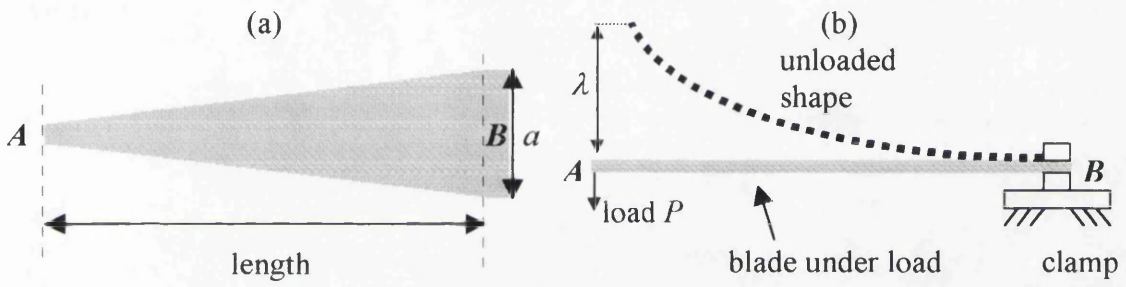
Figure (6.6): - *Blade before and after loading (a) above (b) side view.*

For a trapezoidal blade the maximum deflection at the support point, A, is given by: -

$$\lambda = \alpha \frac{P l_b^{3}}{3 E I_b} \quad [87]$$

(6.1)

where P is the load supported in Newtons, l_b is the length of the blade, E is the Young's Modulus (for Marval 18 steel $E = 186 \times 10^9$ Pa [86]), I_b is the cross-sectional moment of the blade, α is a factor related to the ratio between the width at the tip to the width at the base (and takes values between 1.0 and 1.5) [87].

The cross-sectional moment for a typical blade is given by: -

$$I_b = \frac{a h^3}{12} \quad [87]$$

(6.2)

where a is the width of the blade base (at the clamp), and h is the blade thickness

After substitution of equation (6.2) into (6.1) we obtain an expression for the maximal deflection: -

$$\lambda = 4 \frac{m_t g l_b^3 \alpha}{Eah^3}$$ (6.3)

where m_t is the total mass supported by the spring, which will include mass from the lower pendulum stages.

The spring constant of the blade is given by: -

$$k = \frac{m_t g}{\lambda} = \frac{Eah^3}{4l_b^3 \alpha}$$ (6.4)

Selecting the thickness, length and width for the blade we obtain an uncoupled vertical frequency, f_s, given by: -

$$f_s = \frac{1}{2\pi} \sqrt{\frac{k}{m_s}} = \frac{1}{2\pi} \sqrt{\frac{Eah^3}{4m_s l_b^3 \alpha}}$$ (6.5)

$$\Rightarrow \quad f_s \propto \left(\frac{h}{l}\right)^{3/2}$$ (6.6)

where m_s is the mass supported by the spring in that stage.

The maximum stress at the support point of a cantilever blade (clamped at one end) is given by the following expression

$$\sigma_{MAX} = \frac{6Pl_b}{ah^2} \qquad [87]$$ (6.7)

$$\Rightarrow \quad \sigma_{MAX} \propto \frac{l}{h^2}$$ (6.8)

The maximum permissible stress in the GEO design for the blade is set at approximately half of the elastic limit of the maraging steel to minimise the effect of long term creep. The blades are designed using the criteria outlined above. The choice of and testing of the blades is outlined in section 6.5.

6.5 Choice of Cantilever Blades

6.5.1 Introduction

The arrangements of the two stages of cantilever blades are shown in figure (6.7). The blades have the following parameters obtained using the equations outlined in section 6.4.
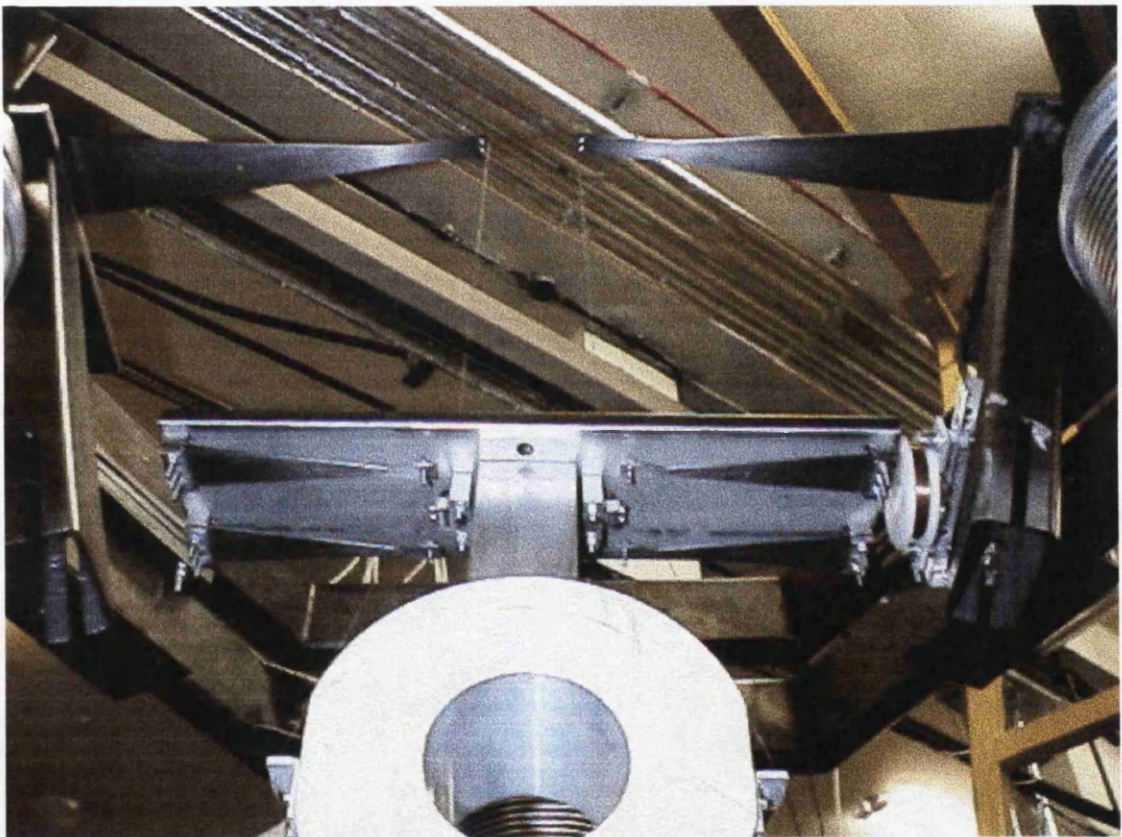
Figure (6.7): - *Photograph of the Glasgow prototype suspension from below (showing 2 blades supporting an upper mass and 4 shorter blades supporting the intermediate mass).*

6.5.2 Upper blades

In order to obtain an uncoupled vertical mode frequency, $f_s \sim 1.9$ Hz, a blade of length, $l_b = 37$ cm, thickness, $h = 2.0 \pm 0.05$ mm and width, $a = 8.2$ cm is required to support a mass, $m_s = 3.0$ kg.

After substitution of these parameters into equation (6.3), and with a total supported mass, $m_t \sim 9$ kg per blade, we obtain a blade deflection of ~ 200 mm. For the blade specification defined above this leads to a maximum stress of ~ 600 MPa. This is approximately 40% of the elastic limit for Marval 18 steel and is therefore acceptable.

6.5.3 Lower blades

The double pendulum will be suspended by a set of 4 cantilever blades. In order to obtain an uncoupled mode frequency, $f_s \sim 3.0$ Hz; a blade of $l_b = 124$ mm, $h = 1.0 \pm 0.05$ mm, and $a = 28$ mm is required to support a mass, $m_s = 1.5$ kg. Putting these parameters into equation (6.3), with $m_t \sim 3$ kg, gives a blade deflection of 49 mm and a maximum bending stress of ~ 700 MPa, from equation (6.6).

The uncoupled vertical mode frequencies and the maximum deflections of both types of blades have been verified experimentally.

The next section explains how these blades were used in a prototype pendulum suspension in Glasgow, in order to test the isolation performance of the blades.

6.5.4 Vertical transfer function

A vertical transfer function from the support to a single mass suspended from two blades was obtained, as shown in figure (6.8). A shaker constructed from piezoelectric elements drove the pendulum and the response was measured using accelerometers. The experimental trace is shown in figure (6.9). The flattening of the response above ~ 20 Hz is consistent with measurements carried out by the VIRGO group on similar blades [88]. This is discussed more fully in the next section. The

111

peak at 55 Hz corresponds to the first flexural (internal) mode of the upper blades. The theoretical response of the upper mass suspended from two cantilever blades was obtained using MATLAB [71], showing a $\frac{1}{f^2}$ fall off above the uncoupled frequency of the blade, as in figure (6.9). This simple model assumes that the blade acts as a massless spring.

A transfer function of the lower blades was also obtained using the same experimental set-up as that outlined for the upper blades, as shown in figure (6.10). An attenuation of ~ 55 dB at 50 Hz was measured, with the blades behaving ideally up to a frequency of ~ 80 Hz. The first internal mode of the lower blades was measured at 240 Hz. The peak at 50 Hz corresponds to electrical mains interference.
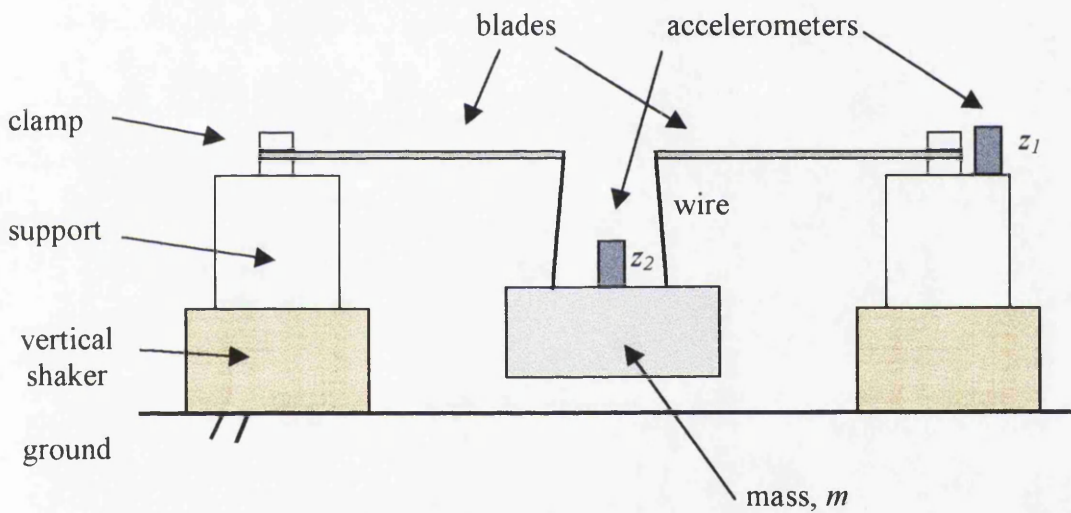
Figure (6.8): - *Schematic of set up for measuring the transfer function, $\frac{z_2}{z_1}$, of a blade.*
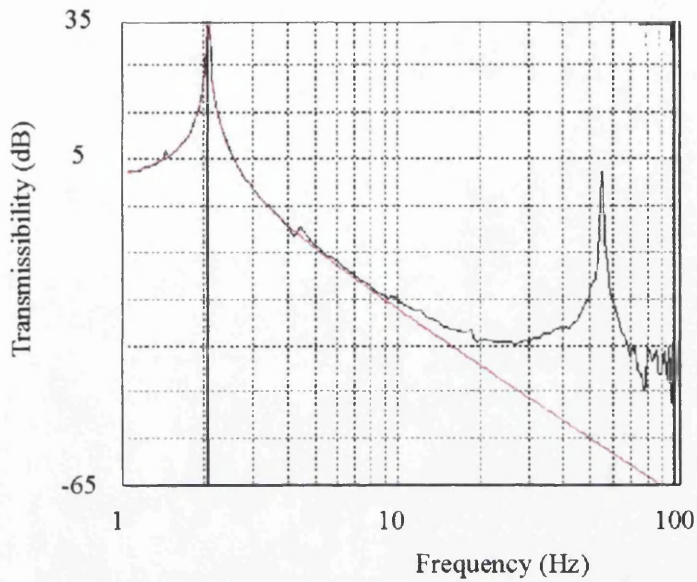
Figure (6.9): - *Vertical transfer function of upper cantilever blades from a single pendulum (ideal theoretical: - red, experimental: - black).*
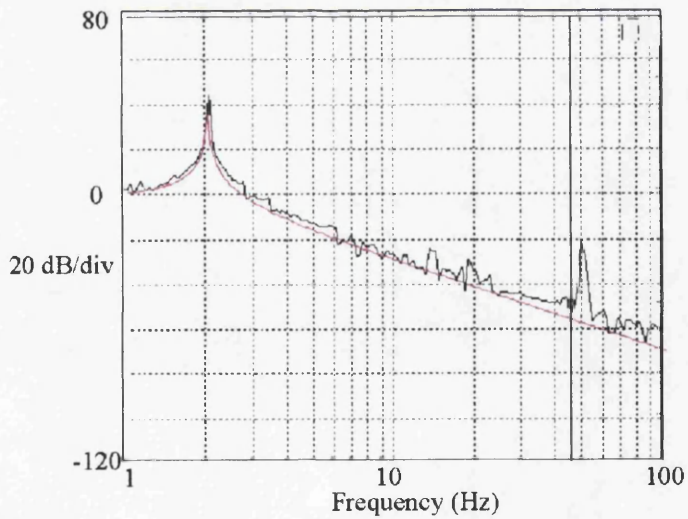
Figure (6.10): - *Horizontal transfer function of lower cantilever blades from a single pendulum (ideal theoretical: - red, experimental: - black).*

113

6.5.5 Conclusions

The transfer function of the cantilever blade is complicated by the fact that it is not a massless spring (i.e. the blades have a finite mass). The consequences of this are twofold. Firstly flexural (internal) mode resonances are seen and secondly the transfer function begins to flatten off, compromising the isolation achieved at a frequency typically approximately 1/3 that of the first flexural mode [88]. The isolation is degraded by the flexural mode frequency such that the modes will have to be damped using a resonant mode damper as outlined in section 6.5.8.

Since the lower blades have a first flexural mode at 240 Hz they therefore behave ideally up to a frequency of ~ 80 Hz and are therefore acceptable for the GEO 600 specification. However a redesign of the upper blades was necessary in order firstly to force the flexural mode resonance of the blade above ~ 100 Hz, where the overall attenuation of the stack and triple pendulum increases rapidly with frequency, and secondly to improve the isolation at 50 Hz. This therefore required a model to predict the flexural mode of the blade.

6.5.6 Modelling of the flexural (internal) mode of the blade
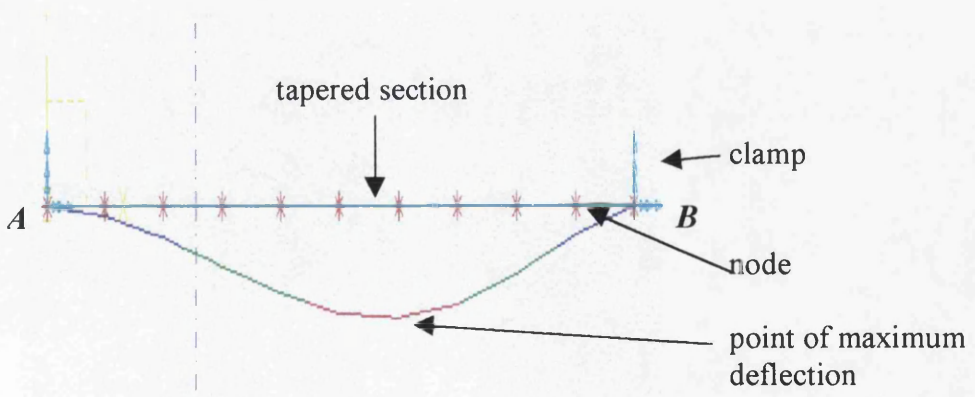
Figure (6.11): - *11 nodes & 10 tapered sections. The shape of the first internal mode of the blade and the point of maximum deflection is also shown.*

The flexural mode frequency, $f_{int.} \propto \dfrac{h}{l^2}$ was modelled using the engineering package I–DEAS [72]. The blade was modelled from 11 nodes, which were joined by 10 tapered beam sections forming a trapezoid, as shown in figure (6.11) and (6.12). Both ends were clamped such that they were constrained in three degrees of freedom. As an initial test the model was used to predict resonances for VIRGO blades for which experimental results were known [88]. The model gave values to within 10 %. The first flexural modes of the existing blades, outlined in section 6.5.2 and 6.5.3, were found to be 60 Hz and 270 Hz for the upper and lower blades respectively. This agrees well with what was seen experimentally as stated in section 6.5.4. For the new blades all three parameters outlined in section 6.4 were carefully considered.

tapered section
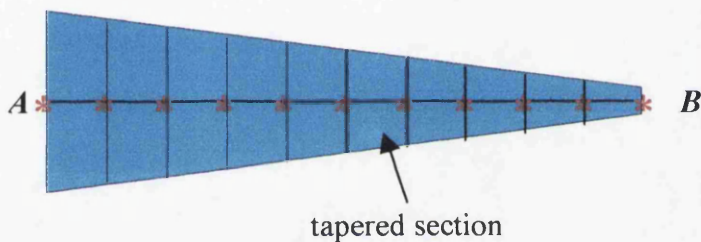
Figure (6.12): - *View of modelled blade from above.*

6.5.7 'NEW' upper blades

The new blades have been designed with an uncoupled vertical mode frequency, $f_s \sim 2.6$ Hz and an internal mode frequency of 120 Hz, as predicted using I–DEAS [72]. This corresponds to a blade of length, $l_b = 24$ cm, $h = 2.0$ mm and $a = 4$ cm, implying a blade deflection of ~ 110 mm and a maximum stress of ~ 800 MPa. A transfer function of the 'new' upper blades was obtained. An attenuation of ~ 40 dB at 50 Hz was measured as shown in figure (6.13). This was an acceptable value. The theoretical ideal transfer function is also shown in figure (6.13) in red. In addition a theoretical model [88] allowing for first order effects of the mass of the blade is shown in blue. The first internal mode of the blade was measured and

found to be 130 Hz. The feature at 40 Hz is a structural resonance related to the prototype experimental set-up. The peak at 50 Hz corresponds to electrical mains interference.
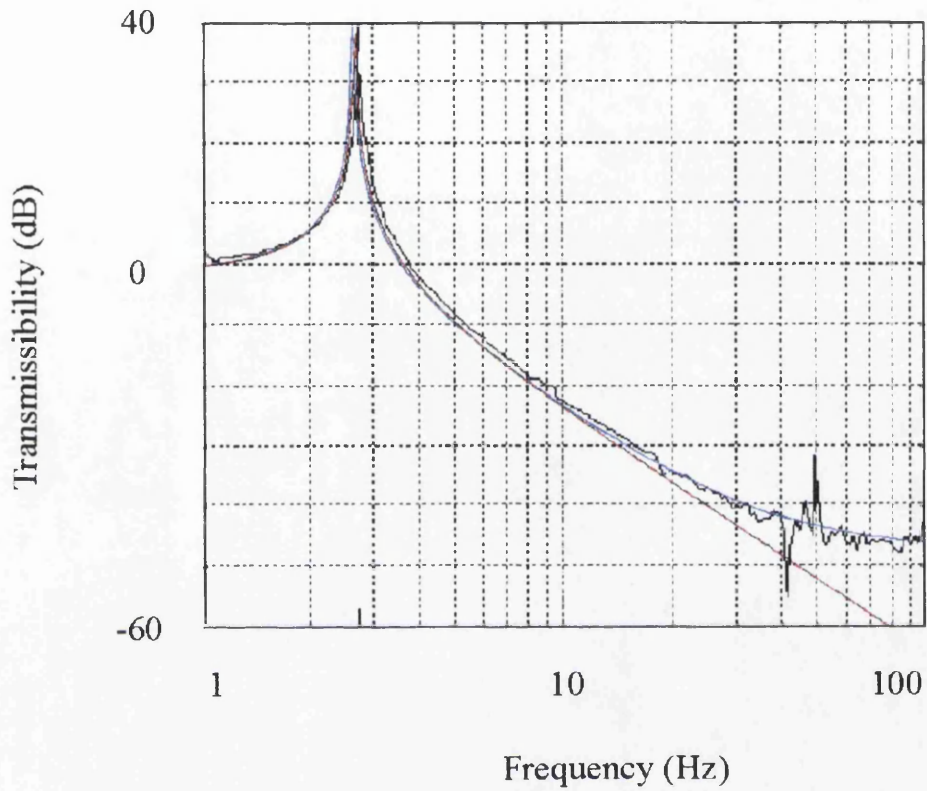
Figure (6.13): - *Vertical transfer function of new upper cantilever blades suspending a single mass (ideal: - red, experimental: - black, theoretical: - blue).*

6.5.8 Resonant mode damper
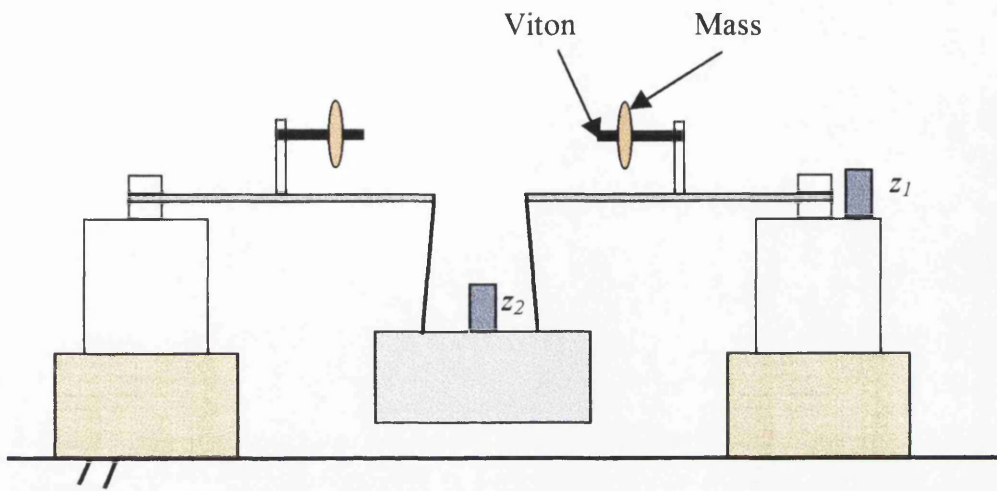
Figure (6.14): - *Schematic of blades and resonant dampers on the set-up used in section 6.5.4.*

As already mentioned in section 6.5.5, the flexural mode frequency of the blade requires to be damped using a resonant mode damper, as shown in figure (6.14) and (6.15).
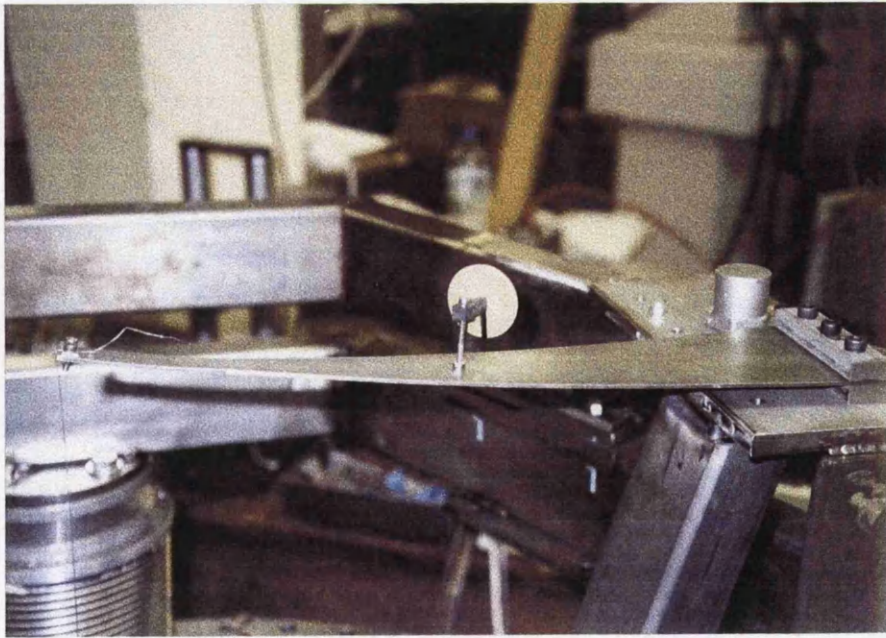
Figure (6.15): - *Photograph of the viton damper on the first set of upper blades, section 6.5.2.*

As stated earlier the first flexural mode of the first set of upper blades, section 6.5.2, has been measured at 55 Hz. The point of maximum deflection and shape of the first internal mode are shown in figure (6.11). Attaching a resonant damper at the point of maximum deflection of the blade allows this mode to be damped. The damper has been adapted from a design used by the VIRGO group [89]. The internal mode of the lower blades, measured at 240 Hz, will not be damped as the attenuation provided by the stack and triple pendulum is adequate at this frequency.

The damper consists of a viton rod (3cm long by 5mm diameter) with a mass of 20 g on it. The mass oscillates, in the vertical direction, on the viton rod with opposite phase to that of the blade's displacement. The damper can be tuned to the resonance of the blade by moving the mass along the viton rod. The dampers have been shown to reduce the transfer function by ~ 30 dB at the resonance as shown in figure (6.16) and (6.17). Figure (6.16) shows the case of one blade with and one blade without a damper compared to both without dampers and figure (6.17) shows the case of both blades with a damper against both without. Over this small frequency range it is possible to resolve the internal mode of each blade which is either due to the fact that the blades are slightly different or that the blades might not be loaded identically. The resonant damper also dampens the second internal mode of the blade, around 160 Hz, without affecting the rest of the transfer function of the blade, as shown in figure (6.18). The other peaks in the spectrum are probably due to acoustic interference since the experiment was carried out in air.

The vacuum specification for GEO 600 requires the partial pressure in the system to be below 5×10^{-8} mbar for H_2 and 10^{-9} mbar for the other gases and so if the viton was to be used for the resonant damper it would have to be encapsulated. Alternatively a material with better vacuum properties could be used (e.g. copper).
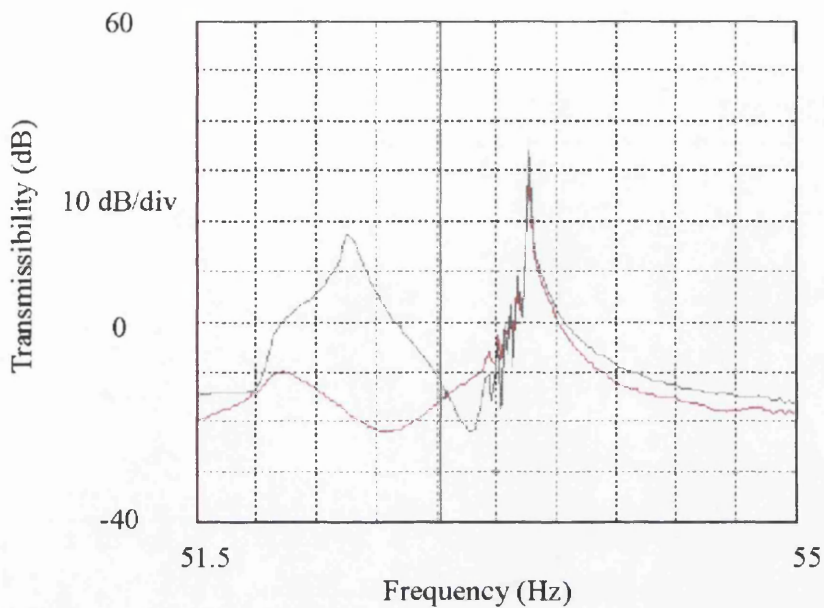
Figure (6.16): - *Transfer function of upper mass suspended from two cantilever blades, one with and one without damper (red) and both without the damper (black).*
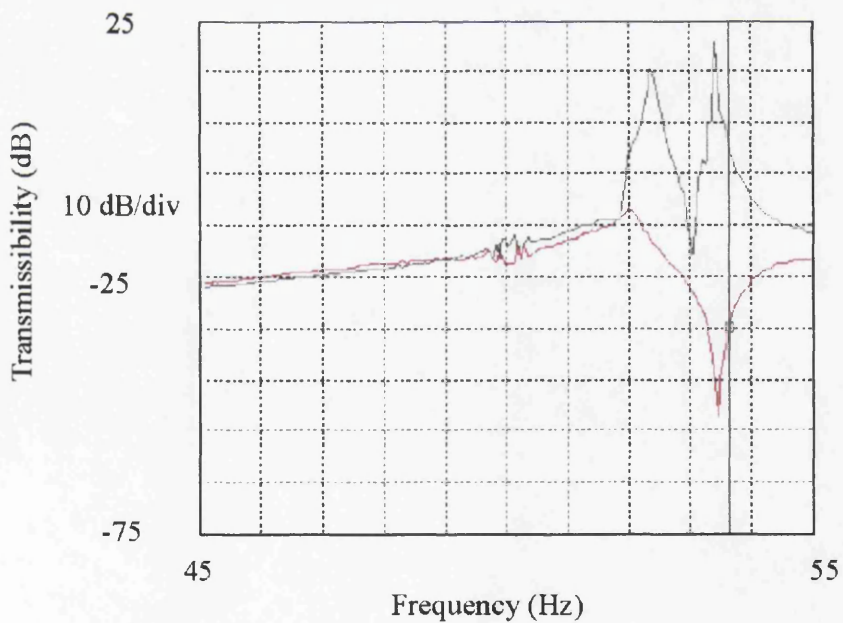
Figure (6.17): - *Transfer function of upper mass suspended from two cantilever blades with one damper on each blade (red) and without the dampers (black).*
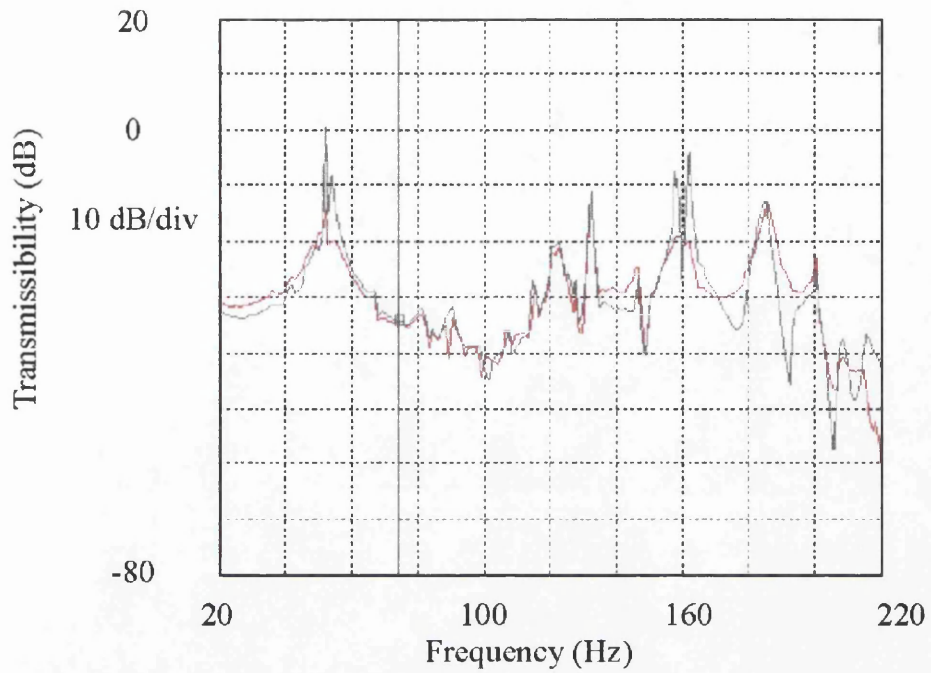
Figure (6.18): - *Transfer function of upper mass suspended from two cantilever blades with (red) and without (black) the resonant dampers. The figure shows the damping of the first two flexural modes at 55 and 160 Hz.*

6.6 Mode Frequencies

The resonant frequencies of the prototype triple pendulum were obtained by exciting the pendulum and measuring the response from an accelerometer attached to the upper mass, the signal from which was analysed using a spectrum analyser. Both the theoretical predictions and experimental results for the prototype triple pendulum are given in table (6.1). It can be seen that for those frequencies that have been observed there is good agreement with the theoretical predictions. The experimental values all have an error of ~ 0.1 Hz. A list of the pendulum parameters can be found in Appendix B.4.

	Theoretical	Experimental
Tilt / longitudinal	3.6, 2.7, 2.4 1.35, 0.5, 0.6	3.5, 2.6, 2.2 1.35, 0.6
Roll / sideways .	52, 3.3, 2.5 1.35, 0.9, 0.6	 1.37, 1.0, 0.6
Rotational	3.1, 1.6, 0.4	3.1, 1.55
Vertical	36, 3.8, 1.0	37, 3.7, 1.0

Table (6.1): - *Theoretical and experimental mode frequencies for the prototype triple pendulum.*

The frequencies can all be seen to be less than 5 Hz apart from the vertical and roll frequencies of the final stage, outlined in blue. As already mentioned in section 5.4.2, these modes couple weakly to the main interferometer signal. The mode frequencies in table (6.1) are different to those quoted in table (5.1) since the final stage of the prototype is on steel wires rather than fused silica.

6.7 Step Response

As discussed in section 5.4, the low frequency resonant modes of the triple pendulum are actively damped from the upper mass. Modelling of the local control servo indicates that all the modes can be damped with a Q value less than 5 except for the vertical and roll frequencies associated with the final stage. The theoretical step response of each mass for all six local control channels, are shown in figure (5.7).

Q values of $\sim$ 5 have been observed for the modes which are damped with the local control servo outlined in section 5.4. The step response of the longitudinal actuators is outlined below. The two longitudinal actuators act along the rear side of the upper mass, as outlined in section 5.4.3 and shown in figure (5.6). An step was applied to both of these longitudinal actuators using a signal generator and the response was measured using an oscilloscope. The theoretical and experimental responses of the two longitudinal actuators are shown in figure (6.19). The experimental plots fit closely with the theoretical prediction (dotted line). The disposition of the sensors/actuators with respect to the upper mass in the Glasgow prototype suspension is shown in figure (6.20).

122
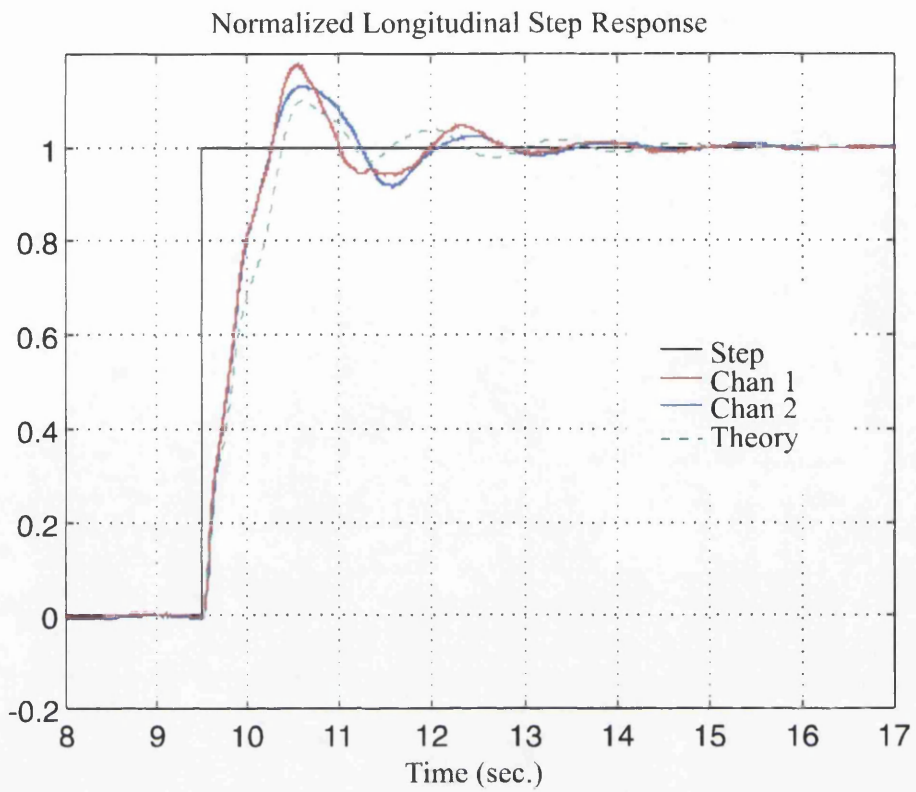
Figure (6.19): - *Longitudinal step response of the two longitudinal actuators. The red and blue bold lines are the experimental response, the dotted green line is the theoretical response and the black line is the step input.*
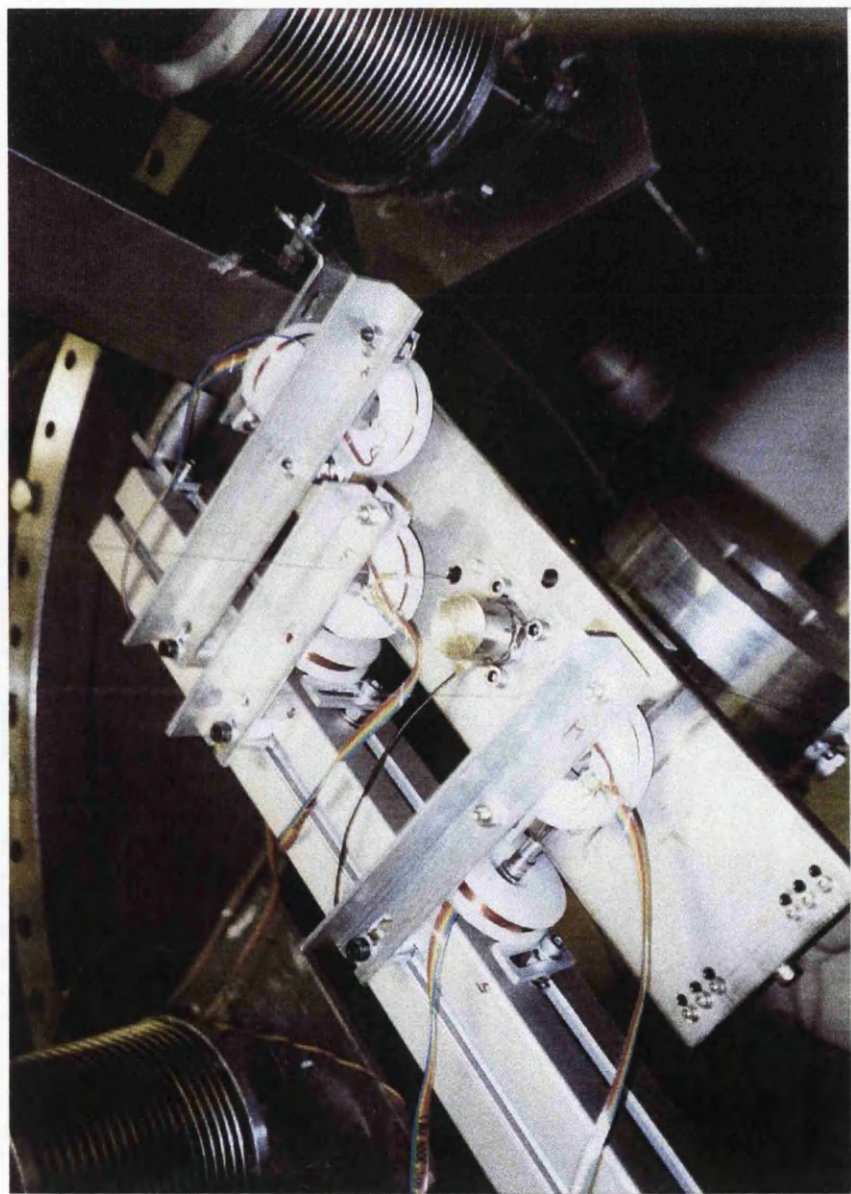
Figure (6.20): - Photograph of the upper mass and the six local control actuators. The actuators on the long rear side are for longitudinal and rotational damping, the one on the short side is for sideways damping and the ones for tilt and vertical damping are on the top of the upper mass.

124

6.8 Transfer Function

6.8.1 Introduction

It is possible to write an expression for both the vertical transmissibility, T_v, and horizontal transmissibility, T_h, of the entire suspension system above the highest resonant frequency, where the system consists of a one-layer passive isolation stack and a triple pendulum suspension incorporating two stages of vertical springs (assumed massless in the first instance).

6.8.2 Horizontal

In the horizontal dimension: -

$$T_h = \left[\frac{f_{sv}}{f}\right]^2 \left[\frac{f_{ph1}}{f}\right]^2 \left[\frac{f_{ph2}}{f}\right]^2 \left[\frac{f_{ph3}}{f}\right]^2$$

where f_{ph1} (0.54 Hz), f_{ph2} (1.3 Hz) and f_{ph3} (2.6 Hz) are the coupled pendulum frequencies. The stack frequency, f_{sv} (9 Hz) is a measured uncoupled frequency. This is a valid input since although the masses of the triple pendulum are all the same, $\sim$ 6 kg, and therefore well coupled, the dynamic mass loading on the stack is significantly greater. Therefore the stack can be taken to be uncoupled from the rest of the suspension.

Taking a ground noise spectrum of $\sim \left[\dfrac{10^{-7}}{f^2}\right]$ m$/\sqrt{\text{Hz}}$ we obtain a resulting test mass motion $dx \sim \left(2.8 \times 10^{-22}\,\text{m}\,/\sqrt{\text{Hz}}\right)_{50\,\text{Hz}}$, which is well within the design goal outlined in section 2.5.

6.8.3 Vertical

In the vertical direction: -

$$T_v = \left[\frac{f_{sv}}{f}\right]^2 \left[\frac{f_{cv1}}{f}\right]^2 \left[\frac{f_{cv2}}{f}\right]^2 \left[\frac{f_{pv}}{f}\right]^2 c \qquad (6.2)$$

where f_{sv} is the stack frequency (15 Hz), f_{cv1} and f_{cv2} are the cantilever spring frequencies of the upper and lower stages respectively (4.2 Hz and 1.3 Hz), f_{pv} is the frequency of the lower stage vertical mode (26 Hz) (all coupled frequencies) and c is the cross-coupling factor (0.1 %).

$\Rightarrow \qquad T_v = 9.6 \times 10^{-11}$ at $f = 50$ Hz.

With a ground noise spectrum of $\left[\dfrac{10^{-7}}{f^2}\right]$ m$/\sqrt{\text{Hz}}$ we obtain a resulting test mass

motion $dx \sim \left(3.8 \times 10^{-21} \text{m}/\sqrt{\text{Hz}}\right)_{50\text{Hz}}$.

However, as mentioned in section 6.5.4, the blades do not act as ideal isolators. The lower blades can be taken as ideal at 50 Hz. For the upper blades it is necessary to take the experimentally measured vertical isolation for the new upper blades at 50 Hz. This value is 10 dB higher than that due to an ideal spring, as shown in figure (6.13).

Furthermore due to the fact that the upper vertical mode, associated with the final stage of the pendulum, occurs at 26 Hz, the fall-off in transmissibility is not as high as expected at 50 Hz (i.e. it has not yet reached its asymptotic value of $\left[\dfrac{f_{pv}}{f}\right]^2$).

Taking all these factors into account, a value for the test mass motion, at 50 Hz, of $dx \sim \left(1.8 \times 10^{-20} \text{m}/\sqrt{\text{Hz}}\right)_{50\text{Hz}}$ is deduced.

This corresponds to a seismic noise level which is a factor of ~ 4 lower than the expected motion due to thermal noise associated with the internal modes.

It should be noted that these calculations do not apply above ~ 120 Hz due to internal modes of the isolation system and the presence of wire resonances. Nevertheless the overall attenuation of the stack and triple pendulum increases rapidly with frequency and therefore at these high frequencies the isolation will be more than adequate.

6.9 Conclusions

Various aspects of the design of the seismic isolation system for GEO 600 have been discussed. The design involves an isolation stack and a triple pendulum incorporating two sets of vertical cantilever blades. Experiments on the individual stages of the Glasgow prototype suspension indicate that a seismic noise level which is a factor of ~ 4 lower than the thermal noise level at 50 Hz should be achievable with the current design [86]. Although this does not meet the objective set out in section 2.5 it is still an acceptable seismic isolation performance. Thus we have shown that a design as outlined in section 2.6 is acceptable for use in GEO 600. Suspensions based on this work are, at the time of writing, under construction in Germany.

There are possibilities of further improving the isolation supplied by a triple pendulum. One of these would be to take advantage of the enhanced isolation obtained at the centre of percussion of a compound pendulum. A theoretical investigation of this idea is given in Appendix E.

Chapter 7

Conclusions

This thesis presents work done in modelling and testing of various suspension systems for isolating optical components for the GEO 600 gravitational waves detector.

The GEO 600 detector is designed to operate down to 50 Hz. The sensitivity limit at this frequency is set by the internal modes of the fused silica test masses. In order to minimise the thermal noise, the main mirror test masses and their suspensions are to be made from fused silica. The techniques for suspending the test masses have been developed in parallel to the work on seismic isolation in Glasgow. The design goal for seismic isolation was to achieve a noise level at each test mass a factor of 10 lower than the thermal noise level. This level of seismic isolation should be achieved with a triple pendulum incorporating two stages of cantilever blades, in order to enhance the vertical isolation, and a single passive isolation stack, providing isolation in both the horizontal and vertical directions.

The first suspension system considered was for the subsidiary mirrors that form the mode-cleaner cavities. The mode-cleaner optics has less stringent requirements for seismic isolation. The isolation is achieved using a double pendulum and a two-layer passive isolation stack. Experiments in Glasgow have shown that this combination more than adequately meets the noise specification.

The triple pendulum suspension for the main test mass mirrors, incorporating two stages of cantilever springs, is a simple but effective way of isolating the test mass suspension to the required level for GEO 600. A detailed dynamical model for a triple pendulum has been developed which enables the various parameters of a triple pendulum to be assigned. It can then be used to investigate, for example, the mode frequencies, transfer function or impulse response for all degrees of freedom. This is essential for the design of a well damped triple pendulum with good coupling between the various modes.

Experiments on the individual stages of a prototype suspension built in Glasgow have shown that a seismic noise level which is a factor of ~ 4 lower than the thermal noise level at 50 Hz can be achieved.

Current work at Glasgow includes the possibility of further improving the isolation supplied by a triple pendulum. One way would be to take advantage of the improved isolation offered by using the centre of percussion of a cantilever blade as the point of suspension for the underlying mass. Another possibility would be to use a quadruple pendulum rather than a triple pendulum. It is proposed that either a triple or a quadruple pendulum will be used as the basis of final stage of isolation for an advanced LIGO interferometer, which has to be sensitive down to 10 Hz [90]. A quadruple pendulum may be required for LIGO in order to meet requirements on local control noise. A triple pendulum has been modelled for a LIGO test mass of 30 kg, by Dr. Ken Strain using the author's dynamical model for a triple pendulum.

The various isolation stages for the mode-cleaner were installed at the GEO 600 site in the summer of 1999. At the time of writing the first main suspension systems were beginning to be installed into the GEO 600 vacuum system. All of the isolation stages including the initial optics with steel wire suspensions should be installed in the summer of 2000. The following summer the final optics with fused silica fibres will be installed and in the autumn of the same year the first data run is expected to take place.

APPENDIX A

Single Pendulum

A.1 Model of a single pendulum.

The file **mcsing.m** assembles the single pendulum model, the ABCD matrices for all degrees of freedom and returns the normal mode frequencies, for all six degrees of freedom, as outlined in chapter 4.

% mcsing.m

```
%*************************************************************
% all units are in S.I.
g       = 9.81;
                        % dimensions of TEST MASS
tx      = 0.15;          % thickness
tr      = 0.1245;        % radius
m       = 2700*pi*tr^2*tx;   % mass
Ix      = m*(tr^2/2);                % moment of inertia (sideways roll)
Iy      = m*(tr^2/4 + tx^2/12);      % moment of inertia (longitudinal tilt)
Iz      = m*(tr^2/4 + tx^2/12);      % moment of inertia (rotation)
l3      = 0.27;          % wire length
                        (NB: - length defined as l in figure (4.1))
d       = 0.001;        % height of lower suspension clamp above c. of m.
s       = 0.081/2;      % 1/2 separation of wires X direction
t1      = tr + 0.006;   % 1/2 separation of wires Y direction
t2      = tr + 0.006 + 0.006;
R       = 140e-6;           % radius of wire
Y       = 1.65e11;          % Young's Modulus of the wire
N       = 4;                % Number of wires (2 or 4)
k       = (N/2)*Y*pi*R^2/l3;    % spring constant of the wire
si      = (t2 – t1)/l3;         % sin(Ω)
co      = (l3^2 – (t2 – t1)^2)^0.5/l3;  % cos(Ω)

%*************************************************************
% LONGITUDINAL AND TILT FREQUENCIES (L, RT)

k11     = – m*g*d/Iy – 2*k*s^2*(co)^2/Iy – m*g*d^2/Iy/l3/(co)
          – m*g*s^2*(si)^2/Iy/l3/(co);
k12     = + m*g*d/Iy/l3/(co);
k21     = + g*d/l3/(co);
k22     = – g/l3/(co);
```

```
% matrix
A      = [    k11    k12
              k21    k22    ];
% calculation of the frequency
longitudinal and tilt frequency        = (sqrt(abs(eig[A])))/2/pi


%*****************************************************************
% SIDEWAYS AND ROLL FREQUENCIES (T, RL)

s11    = − m*g*d/Ix + m*g*t2*(si)/Ix/(co) + m*g*d/Ix*(t2*(si)/l3 − d*(co)/l3)
         − m*g*t2*(si)/Ix/(co)*(t2*si/l3 − d*(co)/l3) + 2*k*l3*(si)*t2/Ix*(t2*(si)/l3
         − d*(co)/l3) + 2*k*l3*d*(si)^2/Ix/(co)*(t2*(si)/l3 − d*(co)/l3) − 2*k*t2^2/Ix
         − 2*k*d*t2*(si)/Ix/(co);
s12    = + m*g*d*(co)/Ix/l3 − m*g*t2*(si)/Ix/l3 + 2*k*(si)*t2*(co)/Ix
         + 2*k*d*(si)^2/Ix;
s21    = − g*(t2*(si)/l3 − d*(co)/l3)
         − 2*k*(si)^2/m/co*(t2*(si) − d*(co)) + 2*k*t2*(si)/m/(co);
s22    = − g*(co)/l3 − 2*k*(si)^2/m;

% matrix
A      = [    s11    s12
              s21    s22    ];

% calculation of the frequency
sideways and roll frequencies =(sqrt(abs(eig[A])))/2/pi


%*****************************************************************
% ROTATIONAL FREQUENCY (RZ)
% wire break offs assumed to be at the Centre of Mass

ro     = − m*g/l3/(co)*(s^2*(co)^2 + t1*t2) − 2*k*s^2*(t2 − t1)^2/l3^2;
rot    = + ro/Iz;

% calculation of the frequency
rotational mode frequency      = (sqrt(abs(rot)))/2/pi


%*****************************************************************
% VERTICAL MODES (Z)

ver    = + 2*k*(co)^2 + m*g*(si)^2/l3/(co);
vert   = − ver / m;

% calculation of the frequency

vertical mode frequency        = (sqrt(abs(vert)))/2/pi
```

Appendix B

B.1 The parameters of a triple pendulum (side view).
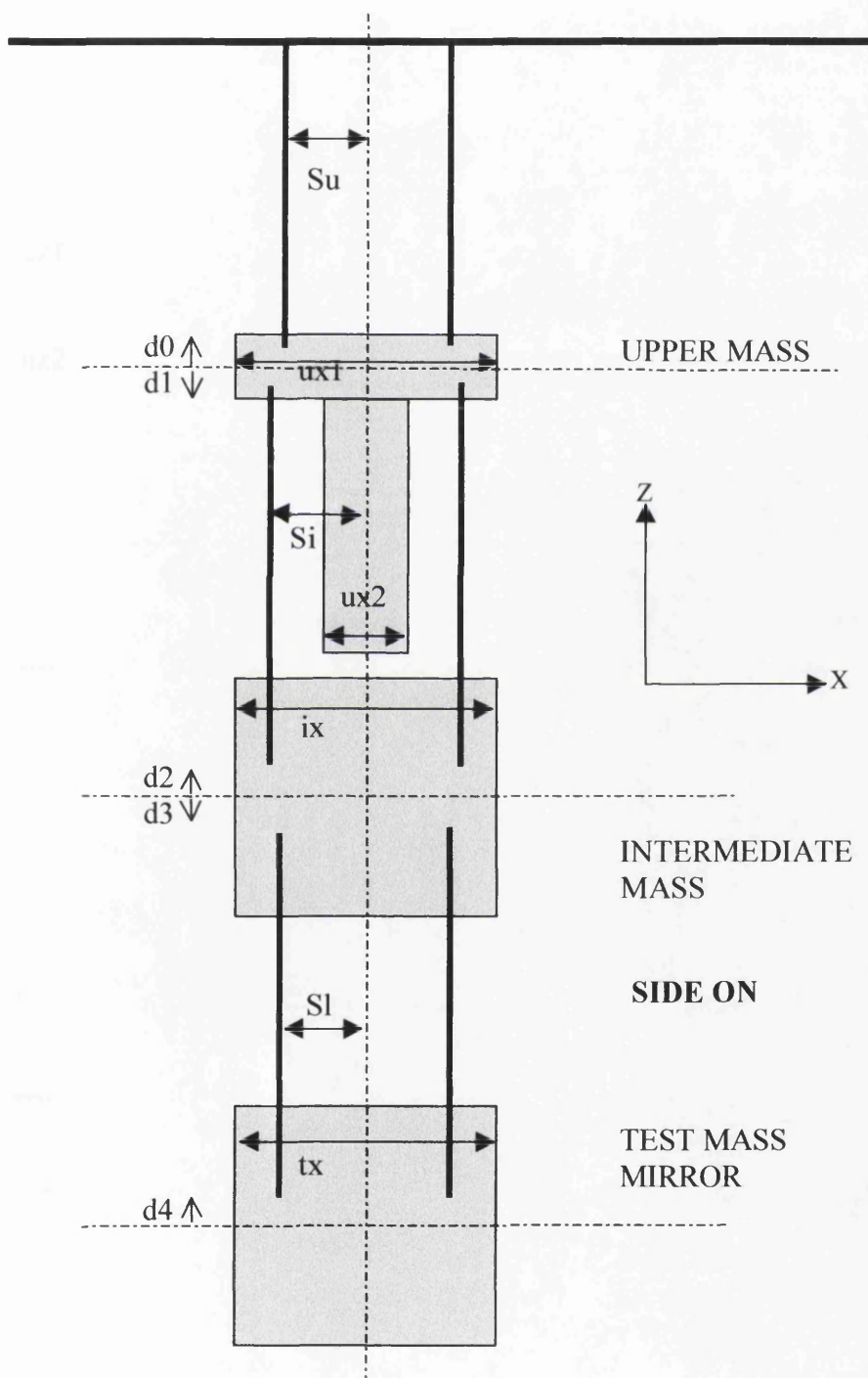
B.2 The parameters for a triple pendulum (face on view).
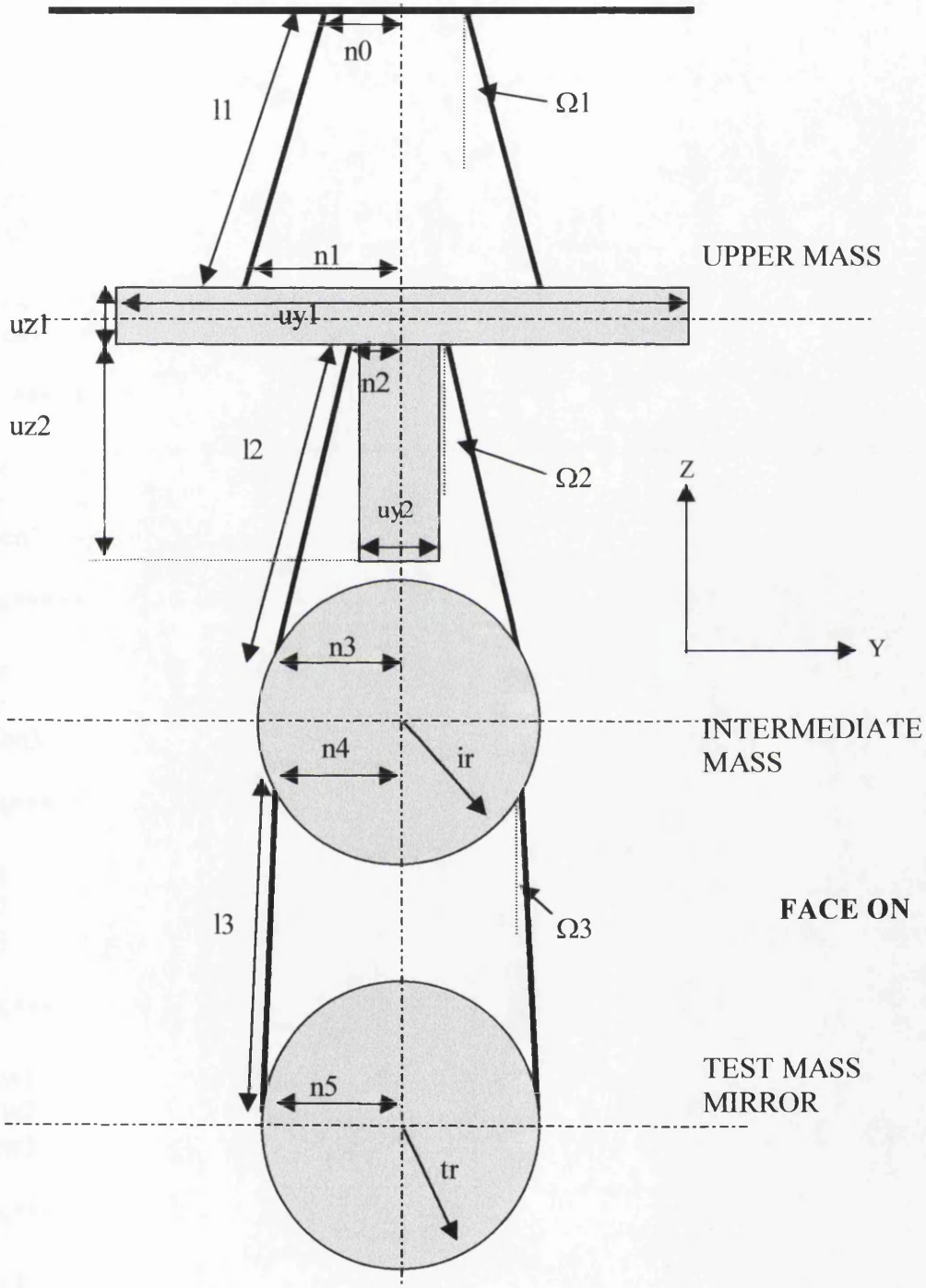
B.3 Parameters of main suspension triple pendulum for GEO 600 (jbr.m).

% refer to Appendix B.1 and B.2
% all units are in S.I.

%***

```
ux1     = 0.1;              % dimensions of UPPER MASS
uy1     = 0.37;
uz1     = 0.012;
ux2     = 0.05;            % not always used for modelling
uy2     = 0.05;
uz2     = 0.09;
den1    = 7800;            % density (stainless steel)
```

%***

```
ix      = 0.1;             % dimension of INTERMEDIATE MASS (cylinder)
ir      = 0.09;
den2    = 2202;            % density (fused silica)
```

%***

```
tx      = 0.1;             % dimensions of TEST MASS (cylinder)
tr      = 0.09;
den3    = 2202;            % density (fused silica)
```

%***

```
l1      = 0.42;            % upper wire length
l2      = 0.187;           % intermediate wire length
l3      = 0.28;            % lower wire length
```

%***

```
nw1     =2;                % number of wires per stage (2 or 4)
nw2     =4;
nw3     =4;
```

%***

```
nc1     =2;                % number of cantilever blades per stage (2,4 or 0)
nc2     =4;
nc3     =0;
```

%***

```
r1      =350e-6;        % radius of upper wire
r2      =175e-6;        % radius of intermediate wire
r3      =150e-6;        % radius of lower wire
```

%**

```
Y1      =1.65e11;              % Youngs Modulus of upper wire     (s/steel 302)
Y2      =1.65e11;              % Youngs Modulus of intermediate wire (s/steel 302)
Y3      =7e10;                 % Youngs Modulus of lower wire     (fused silica)
```

%**

```
ufc1    =2.6;   % uncoupled mode frequency of cantilever stage(=0 for no cantilevers)
ufc2    =3;
ufc3    =0;
% NB:- uncoupled mode frequency- the frequency observed for a cantilever in a
particular stage supporting only the mass of that stage
```

%**

```
d0      = 0.001;        % height of upper wire break-off (above c.of m. upper mass)
d1      = 0.001;        % height of int. wire break-off (below c.of m. upper mass)
d2      = 0.001;        % height of int. wire break-off (above c.of m. of int. mass)
d3      = 0.001;        % height of lower wire break-off (below c.of m. int. mass)
d4      = 0.001;        % height of lower wire break-off (above c.of m. test mass)
```

%**

```
% X direction separation
Su      = 0.00;         % 1/2 separation of upper wires
Si      = 0.03;         % 1/2 separation of intermediate wires
Sl      = 0.005;        % 1/2 separation of lower wires
```

%**

```
% Y direction separation
n0      = 0.03;             % 1/2 separation of upper wires at suspension point
n1      = 0.04;             % 1/2 separation of upper wires at upper mass
n2      =0.045;             % 1/2 separation of intermediate wires at upper mass
n3      =ir-0.0035+0.01;    % 1/2 separation of int. wires at intermediate mass
n4      =tr-0.0035+0.005;   % 1/2 separation of lower wires at intermediate mass
n5      =tr-0.0035+0.005;   % 1/2 separation of lower wires at test mass
```

%**

B.4 Parameters of triple pendulum for Glasgow prototype suspension.

% refer to Appendix B.1 and B.2
% all units are in S.I

%***

ux1	= 0.1;	% dimensions of UPPER MASS
uy1	= 0.37;	
uz1	= 0.012;	
ux2	= 0.05;	% not always used for modelling
uy2	= 0.05;	
uz2	= 0.09;	
den1	= 7800;	% density (stainless steel)

%***

ix	= 0.1;	% dimension of INTERMEDIATE MASS (cylinder)
ir	= 0.09;	
den2	= 2700;	% density (aluminium)

%***

tx	= 0.1;	% dimensions of TEST MASS (cylinder)
tr	= 0.09;	
den3	= 2700;	% density (aluminium)

%***

l1	= 0.38;	% upper wire length
l2	= 0.185;	% intermediate wire length
l3	= 0.28;	% lower wire length

%***

nw1	=2;	% number of wires per stage (2 or 4)
nw2	=4;	
nw3	=4;	

%***

nc1	=2;	% number of cantilever blades per stage (2,4 or 0)
nc2	=4;	
nc3	=0;	

%***

```
r1      =250e-6;        % radius of upper wire
r2      =175e-6;        % radius of intermediate wire
r3      =140e-6;        % radius of lower wire


%****************************************************************


Y1      =1.65e11;               % Youngs Modulus of upper wire (s/steel 302)
Y2      =1.65e11;               % Youngs Modulus of intermediate wire (s/steel 302)
Y3      =1.65e11;               % Youngs Modulus of lower wire (s/steel 302)


%****************************************************************


ufc1    =1.9;   % uncoupled mode frequency of cantilever stage(=0 for no cantilevers)
ufc2    =3;
ufc3    =0;
% NB:- uncoupled mode frequency- the frequency observed for a cantilever in a
% particular stage supporting only the mass of that stage


%****************************************************************


d0      = 0.001;        % height of upper wire break-off (above c.of m. upper mass)
d1      = 0.001;        % height of int. wire break-off (below c.of m. upper mass)
d2      = 0.001;        % height of int. wire break-off (above c.of m. of int. mass)
d3      = 0.001;        % height of lower wire break-off (below c.of m. int. mass)
d4      = 0.001;        % height of lower wire break-off (above c.of m. test mass)


%****************************************************************


% X direction separation
Su      = 0.00;         % 1/2 separation of upper wires
Si      = 0.03;         % 1/2 separation of intermediate wires
Sl      = 0.005;        % 1/2 separation of lower wires


%****************************************************************


% Y direction separation
n0      = 0.03;         % 1/2 separation of upper wires at suspension point
n1      = 0.04;         % 1/2 separation of upper wires at upper mass
n2      = 0.045;        % 1/2 separation of intermediate wires at upper mass
n3      = ir + 0.005;   % 1/2 separation of int. wires at intermediate mass
n4      = tr + 0.01;    % 1/2 separation of lower wires at intermediate mass
n5      = tr + 0.01;    % 1/2 separation of lower wires at test mass


%****************************************************************
```

APPENDIX C

Triple Pendulum

C.1 Input parameters (jbr.m)

The file **jbr.m** represents the input parameters for the triple pendulum for the main suspension for GEO 600. The various parameters are explained in Appendix B.1

% jbr.m

```
%********************************************************************g
        =9.81;
%******************************************************************
ux      = 0.1;                   % dimensions of UPPER MASS (square)
uy      = 0.3;
uz      = 0.07;
den1    = 2700;                  % density (aluminium)
m1      = den1*uy*uz*ux;         % mass
I1x     = m1*(uy^2+uz^2)/12;     % moment of inertia (sideways roll)
I1y     = m1*(uz^2+ux^2)/12;     % moment of inertia (longitudinal tilt)
I1z     = m1*(uy^2+ux^2)/12;     % moment of inertia (rotation)
%******************************************************************
ix      = 0.1;                   % dimension of INTERMEDIATE MASS (cylinder)
ir      = 0.09;
den2    = 2202;                  % density (fused silica)
m2      = den2*pi*ir^2*ix;       % intermediate mass
I2x     = m2*(ir^2/2);           % moment of inertia (sideways roll)
I2y     = m2*(ir^2/4+ix^2/12);   % moment of inertia (longitudinal tilt)
I2z     = m2*(ir^2/4+ix^2/12);   % moment of inertia (rotation)
%******************************************************************
tx      = 0.1;                   % dimensions of TEST MASS (cylinder)
tr      = 0.09;
den3    = 2202;                  % density (fused silica)
m3      = den3*pi*tr^2*tx;       % test mass
I3x     = m3*(tr^2/2);           % moment of inertia (sideways roll)
I3y     = m3*(tr^2/4+tx^2/12);   % moment of inertia (longitudinal tilt)
I3z     = m3*(tr^2/4+tx^2/12);   % moment of inertia (rotation)
%******************************************************************
l1      = 0.42;           % upper wire length
l2      = 0.187;          % intermediate wire length
l3      = 0.28;           % lower wire length
%******************************************************************

nw1     = 2;              % number of wires per stage (2 or 4)
```

138

```
nw2     = 4;                % = number of cantilevers (if fitted)
nw3     = 4;
%**********************************************************************
r1      = 350e-6;       % radius of upper wire
r2      = 175e-6;       % radius of intermediate wire
r3      = 154e-6;       % radius of lower wire
%**********************************************************************
Y1      = 1.65e11;          % Youngs Modulus of upper wire     (s/steel 302)
Y2      = 1.65e11;          % Youngs Modulus of intermediate wire (s/steel 302)
Y3      = 7e10;             % Youngs Modulus of lower wire      (fused silica)
%**********************************************************************
ufc1    = 2.57;% uncoupled mode frequency of cantilever stage(=0 for no cantilevers)
ufc2    = 3;
ufc3    = 0;
% NB:- uncoupled mode frequency- the frequency observed for a cantilever in a
% particular stage supporting only the mass of that stage
%**********************************************************************
d0      = 0.001; % height of upper wire break-off (above c.of m. upper mass)
d1      = 0.001; % height of intermediate wire break-off (below c.of m. upper mass)
d2      = 0.001; % height of intermediate wire break-off (above c.of m. of int. mass)
d3      = 0.001; % height of lower wire break-off (below c.of m. intermediate mass)
d4      = 0.001; %height of lower wire break-off (above c.of m.test mass)
%**********************************************************************
% X direction separation
su      = 0.00;         % 1/2 separation of upper wires
si      = 0.03;         % 1/2 separation of intermediate wires
sl      = 0.005;        % 1/2 separation of lower wires
%**********************************************************************
% Y direction separation
n0      = 0.03;         % 1/2 separation of upper wires at suspension point
n1      = 0.04;         % 1/2 separation of upper wires at upper mass
n2      = 0.045;            % 1/2 separation of intermediate wires at upper mass
n3      = ir-0.0035+0.01;   % 1/2 separation of int. wires at intermediate mass
n4      = tr-0.0035+0.005;  % 1/2 separation of lower wires at intermediate mass
n5      = tr-0.0035+0.005;  % 1/2 separation of lower wires at test mass
%NB:- i.e. n4 = (radius) - (flat) + (break-off bar)
%**********************************************************************
% local control units mechanical details
leverarmrt      = 0.03; % half spacing of coils acting on tilt, rt
leverarmrz      = 0.08; % half spacing of coils acting on rotation, rz
leverarmrl      = 0.08; % half spacing of coils acting on roll, rl
%local control gains
gain    = 0.4;
gainzrtrl       = gain; % vertical, z, tilt, rt, roll rl (coils on top of upper mass)
gaint   = gain.*2;      % sideways, t (coil on one end of upper mass)
gainlrz = gain;         % longitudinal, l, rotation, rz (coils on long rear side of mass)
%**********************************************************************

% represents small loss (so as not dividing by zero)
b1      = 0.03;b2=0.03;b3=0.03;b4=0.03; b5=0.03; b6=0.03;
```

```
%*******************************************************************
% END OF INPUT
%*******************************************************************
% CALCULATIONS
%*******************************************************************
% spring constants
kc1     = 1/2 * (2*pi*ufc1)^2*m1;
kc2     = 1/2 * (2*pi*ufc2)^2*m2;
kc3     = 1/2 * (2*pi*ufc3)^2*m3;
kw1     = Y1*pi*r1^2/l1*nw1/2;
kw2     = Y2*pi*r2^2/l2*nw2/2;
kw3     = Y3*pi*r3^2/l3*nw3/2;
if (kc1 == 0)
k1      = kw1;
else
k1      = kc1*kw1/(kc1+kw1);
end
if (kc2 == 0)
k2      = kw2;
else
k2      = kc2*kw2/(kc2+kw2);
end
if (kc3 == 0)
k3      = kw3;
else
k3      = kc3*kw3/(kc3+kw3);
end
%*******************************************************************
% in X-direction wires must be vertical
s0      = su;s1 = su;
s2      = si;s3 = si;
s4      = sl;s5 = sl;
%*******************************************************************
m13     = m1+m2+m3;m23    = m2+m3;
%*******************************************************************
% cosine and sine of the angle the wire makes with the vertical (z)
si1     = (n1-n0)/l1;              % sin(Ω1)
si2     = (n3-n2)/l2;              % sin(Ω2)
si3     = (n5-n4)/l3;              % sin(Ω3)
c1      = (l1^2-(n1-n0)^2)^0.5/l1; % cos(Ω1)
c2      = (l2^2-(n3-n2)^2)^0.5/l2; % cos(Ω2)
c3      = (l3^2-(n5-n4)^2)^0.5/l3; % cos(Ω3)
%*******************************************************************
```

C.2. Model and ABCD matrices (cit.m)

The file **cit.m** assembles the triple pendulum model and the ABCD matrices for all degrees of freedom, for the input file **jbr.m** (for example). The states are the translation of and rotation about the centre of mass of each mass.

% cit.m

```
%*******************************************************************
jbr;      % input parameters from jbr.m (for example)
%*******************************************************************
% LONGITUDINAL AND TILT FREQUENCIES

k11     = -m13*g*d0/I1y-2*k1*s0^2*c1^2/I1y-m23*g*d1/I1y-2*k2*s2^2*c2^2/I1y-
          m23*g*d1^2/I1y/l2/c2-m13*g*d0^2/I1y/l1/c1-m13*g*s0^2*si1^2/I1y/l1/c1-
          m23*g*s2^2*si2^2/I1y/l2/c2;
k12     = -m23*g*d1/I1y/l2/c2+m13*g*d0/I1y/l1/c1;
k13     = -m23*g*d1*d2/I1y/l2/c2+2*k2*s2^2*c2^2/I1y+
          m23*g*s2^2*si2^2/l2/c2/I1y;
k14     = +m23*g*d1/I1y/l2/c2;
k15     = 0;
k16     = 0;

k21     = +m13*g*d0/m1/l1/c1-m23*g*d1/m1/l2/c2;
k22     = -m13*g/m1/l1/c1-m23*g/m1/l2/c2;
k23     = -m23*g*d2/m1/l2/c2;
k24     = +m23*g/m1/l2/c2;
k25     = 0;
k26     = 0;

k31     = +2*k2*s2^2*c2^2/I2y-
          m23*g*d2*d1/I2y/l2/c2+m23*g*s2^2*si2^2/I2y/l2/c2;
k32     = -m23*g*d2/I2y/l2/c2 ;
k33     = -m23*g*d2/I2y-2*k2*s2^2*c2^2/I2y-m3*g*d3/I2y-2*k3*s4^2*c3^2/I2y-
          m23*g*d2^2/I2y/l2/c2-m3*g*d3^2/I2y/l3/c3-m23*g*s2^2*si2^2/l2/I2y/c2-
          m3*g*s4^2*si3^2/l3/I2y/c3;
k34     = +m23*g*d2/I2y/l2/c2-m3*g*d3/I2y/l3/c3;
k35     = -m3*g*d3*d4/I2y/l3/c3+2*k3*s4^2*c3^2/I2y+m3*g*s4^2*si3^2/l3/I2y/c3;
k36     = +m3*g*d3/I2y/l3/c3;

k41     = +m23*g*d1/m2/l2/c2;
k42     = +m23*g/m2/l2/c2;
k43     = +m23*g*d2/m2/l2/c2-d3*m3*g/m2/l3/c3;
k44     = -m23*g/m2/l2/c2-m3*g/m2/l3/c3;
k45     = -m3*g*d4/m2/l3/c3;
k46     = +m3*g/m2/l3/c3;

k51     = 0;
k52     = 0;
```

```
k53    = +2*k3*s4^2*c3^2/I3y-m3*g*d4*d3/l3/I3y/c3+m3*g*s4^2*si3^2/I3y/l3/c3;
k54    = -m3*g*d4/I3y/l3/c3;
k55    = -m3*g*d4/I3y-2*k3*s4^2*c3^2/I3y-m3*g*d4^2/I3y/l3/c3-
         m3*g*s4^2*si3^2/I3y/l3/c3;
k56    = +m3*g*d4/I3y/l3/c3;

k61    = 0;
k62    = 0;
k63    = +g*d3/l3/c3;
k64    = +g/l3/c3;
k65    = +g*d4/l3/c3;
k66    = -g/l3/c3;
%*****************************************************************
%state space matrices

% q1  xn    q2    xm    q3    x6    Q1    vn    Q2    vm    Q3    v6
A=[0   0     0     0     0     0     1     0     0     0     0     0
   0   0     0     0     0     0     0     1     0     0     0     0
   0   0     0     0     0     0     0     0     1     0     0     0
   0   0     0     0     0     0     0     0     0     1     0     0
   0   0     0     0     0     0     0     0     0     0     1     0
   0   0     0     0     0     0     0     0     0     0     0     1
   k11 k12   k13   k14   k15   k16   -b1   0     0     0     0     0
   k21 k22   k23   k24   k25   k26   0     -b2   0     0     0     0
   k31 k32   k33   k34   k35   k36   0     0     -b3   0     0     0
   k41 k42   k43   k44   k45   k46   0     0     0     -b4   0     
   k51 k52   k53   k54   k55   k56   0     0     0     0     -b5   0
   k61 k62   k63   k64   k65   k66   0     0     0     0     0     -b6];

XX =  -m13*g*d0/I1y/l1/c1;
YY =  +m13*g/m1/l1/c1;
ZZ =  -m13*g*d0/I1y/l1/c1;
VV =  +m13*g/m1/l1/c1;

B=[
0     0     0     0     0     0     XX    YY    0     0     0     0
0     0     0     0     0     0     1/I1y 0     0     0     0     0
0     0     0     0     0     0     0     1/m1  0     0     0     0
0     0     0     0     0     0     ZZ    0     0     0     0     0
0     0     0     0     0     0     0     VV    0     0     0     0 ]';

C=[
1     0     0     0     0     0     0     0     0     0     0     0
0     1     0     0     0     0     0     0     0     0     0     0
0     0     1     0     0     0     0     0     0     0     0     0
0     0     0     1     0     0     0     0     0     0     0     0
0     0     0     0     1     0     0     0     0     0     0     0
0     0     0     0     0     1     0     0     0     0     0     0];

D=[   0 0 0 0 0
```

```
          0 0 0 0 0
          0 0 0 0 0
          0 0 0 0 0
          0 0 0 0 0
          0 0 0 0 0];
```

%**
% SIDEWAYS AND ROLL FREQUENCIES

j11   = -m13*g*d0/I1x+m13*g*n1*si1/I1x/c1-2*k1*n1^2/I1x-
         2*k1*n1*d0*si1/I1x/c1-m23*g*d1/I1x-m23*g*n2*si2/I1x/c2-
         2*k2*n2^2/I1x+2*k2*n2*d1*si2/I1x/c2+m13*g*d0/I1x*(n1*si1/l1-
         d0*c1/l1)-m13*g*n1*si1/I1x/c1*(n1*si1/l1-
         d0*c1/l1)+2*k1*l1*si1*n1/I1x*(n1*si1/l1-
         d0*c1/l1)+2*k1*l1*d0*si1^2/I1x/c1*(n1*si1/l1-d0*c1/l1)+m23*g*d1/I1x*(-
         n2*si2/l2-d1*c2/l2)+m23*g*n2*si2/I1x/c2*(-n2*si2/l2-d1*c2/l2)-
         2*k2*l2*si2*n2/I1x*(-n2*si2/l2-d1*c2/l2)+2*k2*l2*d1*si2^2/I1x/c2*(-
         n2*si2/l2-d1*c2/l2);
j12   = -m23*g*d1*c2/I1x/l2-m23*g*n2*si2/I1x/l2+2*k2*si2*n2*c2/I1x-
         2*k2*d1*si2^2/I1x+m13*g*d0*c1/I1x/l1-
         m13*g*n1*si1/I1x/l1+2*k1*si1*n1*c1/I1x+2*k1*d0*si1^2/I1x;
j13   = m23*g*d1/I1x*(n3*si2/l2-d2*c2/l2)+m23*g*n2*si2/I1x/c2*(n3*si2/l2-
         d2*c2/l2)-2*k2*l2*si2*n2/I1x*(n3*si2/l2-
         d2*c2/l2)+2*k2*l2*d1*si2^2/I1x/c2*(n3*si2/l2-d2*c2/l2)+2*k2*n2*n3/I1x-
         2*k2*d1*si2*n3/I1x/c2;
j14   = +m23*g*d1*c2/I1x/l2+m23*g*n2*si2/I1x/l2-
         2*k2*si2*n2*c2/I1x+2*k2*d1*si2^2/I1x;
j15   = 0;
j16   = 0;

j21   = -m13*g/m1*(n1*si1/l1-d0*c1/l1)-2*k1*l1*si1^2/m1/c1*(n1*si1/l1-
         d0*c1/l1)+2*k1*n1*si1/m1/c1+m23*g/m1*(-n2*si2/l2-
         d1*c2/l2)+2*k2*l2*si2^2/m1/c2*(-n2*si2/l2-d1*c2/l2)+2*k2*n2*si2/m1/c2;
j22   = -m13*g*c1/m1/l1-m23*g*c2/m1/l2-2*k1*si1^2/m1-2*k2*si2^2/m1;
j23   = -2*k2*n3*si2/m1/c2+m23*g/m1*(n3*si2/l2-
         d2*c2/l2)+2*k2*l2*si2^2/m1/c2*(n3*si2/l2-d2*c2/l2);
j24   = +m23*g*c2/m1/l2+2*k2*si2^2/m1;
j25   = 0;
j26   = 0;

j31   =+m23*g*d2/I2x*(-n2*si2/l2-d1*c2/l2)-m23*g*n3*si2/I2x/c2*(-n2*si2/l2-
         d1*c2/l2)+2*k2*l2*si2*n3/I2x*(-n2*si2/l2-
         d1*c2/l2)+2*k2*l2*d2*si2^2/I2x/c2*(-n2*si2/l2-
         d1*c2/l2)+2*k2*n2*n3/I2x+2*k2*d2*n2*si2/I2x/c2;
j32   = -(+m23*g*d2*c2/I2x/l2-
         m23*g*n3*si2/I2x/l2+2*k2*si2*n3*c2/I2x+2*k2*d2*si2^2/I2x);
j33   = +m23*g*d2/I2x*(n3*si2/l2-d2*c2/l2)-m23*g*n3*si2/I2x/c2*(n3*si2/l2-
         d2*c2/l2)+2*k2*l2*si2*n3/I2x*(n3*si2/l2-
         d2*c2/l2)+2*k2*l2*d2*si2^2/I2x/c2*(n3*si2/l2-d2*c2/l2)-2*k2*n3*n3/I2x-
         2*k2*d2*n3*si2/I2x/c2-

$$m23*g*d2/I2x+m23*g*n3*si2/I2x/c2+m3*g*d3/I2x*(-n4*si3/l3-$$
$$d3*c3/l3)+m3*g*n4*si3/I2x/c3*(-n4*si3/l3-d3*c3/l3)-2*k3*l3*si3*n4/I2x*(-$$
$$n4*si3/l3-d3*c3/l3)+2*k3*l3*d3*si3^2/I3x/c3*(-n4*si3/l3-d3*c3/l3)-$$
$$2*k3*n4*n4/I2x+2*k3*d3*n4*si3/I2x/c3-m3*g*d3/I2x-m3*g*n4*si3/I2x/c3;$$

j34 $= -(+m3*g*d3*c3/I2x/l3+m3*g*n4*si3/I2x/l3-$
$$2*k3*si3*n4*c3/I2x+2*k3*d3*si3^2/I2x)+m23*g*d2*c2/I2x/l2-$$
$$m23*g*n3*si2/I2x/l2+2*k2*si2*n3*c2/I2x+2*k2*d2*si2^2/I2x;$$

j35 $=+m3*g*d3/I2x*(n5*si3/l3-d4*c3/l3)+m3*g*n4*si3/I2x/c3*(n5*si3/l3-$
$$d4*c3/l3)-2*k3*l3*si3*n4/I2x*(n5*si3/l3-$$
$$d4*c3/l3)+2*k3*l3*d3*si3^2/I2x/c3*(n5*si3/l3-d4*c3/l3)+2*k3*n4*n5/I2x-$$
$$2*k3*d3*n5*si3/I2x/c3;$$

j36 $=+m3*g*d3*c3/I2x/l3+m3*g*n4*si3/I2x/l3-$
$$2*k3*si3*n4*c3/I2x+2*k3*d3*si3^2/I2x;$$

j41 $= +m23*g*si2*n2/m2/l2+m23*c2*g*d1/m2/l2+2*k2*si2^3*n2/m2/c2+$
$$2*k2*si2^2*d1/m2-2*k2*n2*si2/m2/c2;$$

j42 $= +m23*g*c2/m2/l2+2*k2*si2^2/m2;$

j43 $= -m23*g*n3*si2/m2/l2+m23*g*d2*c2/m2/l2-$
$$2*k2*l2*si2^2/m2/c2*(n3*si2/l2-$$
$$d2*c2/l2)+2*k2*n3*si2/m2/c2+2*k3*l3*si3^2/m2/c3*(-n4*si3/l3-$$
$$d3*c3/l3)+m3*g/m2*(-n4*si3/l3-d3*c3/l3)+2*k3*n4*si3/m2/c3;$$

j44 $= -m23*g*c2/m2/l2-m3*g*c3/m2/l3-2*k2*si2^2/m2-2*k3*si3^2/m2;$

j45 $= -m3*g*d4*c3/m2/l3+m3*g*n5*si3/l3/m2-$
$$2*k3*n5*si3/m2/c3+2*k3*l3*si3^2/m2/c3*(n5*si3/l3-d4*c3/l3);$$

j46 $= +m3*g*c3/m2/l3+2*k3*si3^2/m2;$

j51 $= 0;$

j52 $= 0;$

j53 $=+m3*g*d4/I3x*(-n4*si3/l3-d3*c3/l3)-m3*g*n5*si3/I3x/c3*(-n4*si3/l3-$
$$d3*c3/l3)+2*k3*l3*si3*n5/I3x*(-n4*si3/l3-$$
$$d3*c3/l3)+2*k3*l3*d4*si3^2/I3x/c3*(-n4*si3/l3-$$
$$d3*c3/l3)+2*k3*n5*n4/I3x+2*k3*d4*n4*si3/I3x/c3;$$

j54 $= -(+m3*g*d4*c3/I3x/l3-$
$$m3*g*n5*si3/I3x/l3+2*k3*si3*n5*c3/I3x+2*k3*d4*si3^2/I3x);$$

j55 $=-m3*g*d4/I3x+m3*g*n5*si3/I3x/c3+m3*g*d4/I3x*(n5*si3/l3-d4*c3/l3)-$
$$m3*g*n5*si3/I3x/c3*(n5*si3/l3-d4*c3/l3)+2*k3*l3*si3*n5/I3x*(n5*si3/l3-$$
$$d4*c3/l3)+2*k3*l3*d4*si3^2/I3x/c3*(n5*si3/l3-d4*c3/l3)-2*k3*n5^2/I3x-$$
$$2*k3*d4*n5*si3/I3x/c3;$$

j56 $= +m3*g*d4*c3/I3x/l3-$
$$m3*g*n5*si3/I3x/l3+2*k3*si3*n5*c3/I3x+2*k3*d4*si3^2/I3x;$$

j61 $= 0;$

j62 $= 0;$

j63 $= -g*(-n4*si3/l3-d3*c3/l3)-2*k3*si3^2/m3/c3*(-n4*si3-d3*c3)-$
$$2*k3*n4*si3/m3/c3;$$

j64 $= +g*c3/l3+2*k3*si3^2/m3;$

j65 $= -g*(n5*si3/l3-d4*c3/l3)-2*k3*si3^2/m3/c3*(n5*si3-$
$$d4*c3)+2*k3*n5*si3/m3/c3;$$

j66 $= -g*c3/l3-2*k3*si3^2/m3;$

%**

144

%state space matrices

% q1	xn	q2	xm	q3	x6	Q1	vn	Q2	vm	Q3	v6
A=[0	0	0	0	0	0	1	0	0	0	0	0
0	0	0	0	0	0	0	1	0	0	0	0
0	0	0	0	0	0	0	0	1	0	0	0
0	0	0	0	0	0	0	0	0	1	0	0
0	0	0	0	0	0	0	0	0	0	1	0
0	0	0	0	0	0	0	0	0	0	0	1
j11	j12	j13	j14	j15	j16	-b1	0	0	0	0	0
j21	j22	j23	j24	j25	j26	0	-b2	0	0	0	0
j31	j32	j33	j34	j35	j36	0	0	-b3	0	0	0
j41	j42	j43	j44	j45	j46	0	0	0	-b4	0	0
j51	j52	j53	j54	j55	j56	0	0	0	0	-b5	0
j61	j62	j63	j64	j65	j66	0	0	0	0	0	-b6];

SS = -m13*g*d0*c1/I1x/l1+m13*g*n1*si1/I1x/l1-2*k1*si1*n1*c1/I1x-2*k1*d0*si1^2/I1x;
TT = +m13*g*c1/m1/l1+2*k1*si1^2/m1;
UU = -m13*g*d0*c1/I1x/l1+m13*g*n1*si1/I1x/l1-2*k1*si1*n1*c1/I1x-2*k1*d0*si1^2/I1x;
WW = +m13*g*c1/m1/l1+2*k1*si1^2/m1;

B=[											
0	0	0	0	0	0	SS	TT	0	0	0	0
0	0	0	0	0	0	1/I1x	0	0	0	0	0
0	0	0	0	0	0	0	1/m1	0	0	0	0
0	0	0	0	0	0	UU	0	0	0	0	0
0	0	0	0	0	0	0	WW	0	0	0	0]';

C=[											
1	0	0	0	0	0	0	0	0	0	0	0
0	1	0	0	0	0	0	0	0	0	0	0
0	0	1	0	0	0	0	0	0	0	0	0
0	0	0	1	0	0	0	0	0	0	0	0
0	0	0	0	1	0	0	0	0	0	0	0
0	0	0	0	0	1	0	0	0	0	0	0];

D=[0 0 0 0 0
     0 0 0 0 0
     0 0 0 0 0
     0 0 0 0 0
     0 0 0 0 0
     0 0 0 0 0];

%**
% ROTATIONAL FREQUENCY

AA = m13*g/l1/c1*(s0^2*c1^2+n0*n1)+2*k1*s0^2*(n1-n0)^2/l1^2;
BB = m23*g/l2/c2*(s2^2*c2^2+n2*n3)+2*k2*s2^2*(n3-n2)^2/l2^2;

CC   = m3*g/l3/c3*(s4^2*c3^2+n4*n5)+2*k3*s4^2*(n5-n4)^2/l3^2;

i11   = -AA/I1z-BB/I1z;
i12   = BB/I1z;
i21   = BB/I2z;
i22   = -BB/I2z-CC/I2z;
i23   = CC/I2z;
i32   = CC/I3z;
i33   = -CC/I3z;
%**
% state space matrices

%	Q1	Q2	Q3	q1	q2	q3
ar = [	0	0	0	1	0	0
	0	0	0	0	1	0
	0	0	0	0	0	1
	i11	i12	0	-b1	0	0
	i21	i22	i23	0	-b2	0
	0	i32	i33	0	0	-b3];

br = [	0	0	0	1	0	0	
	0	0	0	1/I1z	0	0	
	0	0	0	1	0	0	]';

cr = [	1	0	0	0	0	0	
	0	1	0	0	0	0	
	0	0	1	0	0	0];	

dr   = [0 0 0
               0 0 0
               0 0 0];

%**
% VERTICAL MODES

h1   = 2*k1*c1^2+m13*g*si1^2/l1/c1;
h2   = 2*k2*c2^2+m23*g*si2^2/l2/c2;
h3   = 2*k3*c3^2+m3*g*si3^2/l3/c3;

h11   = - h1/m1 - h2 /m1;
h12   = h2/m1 ;
h21   = h2 / m2;
h22   = - h2 / m2 - h3 / m2;
h23   = h3 / m2 ;
h32   = h3 / m3;
h33   = - h3 / m3;

%**
% state space matrices

146

%	x1	x2	x3	v1	v2	v3
av = [	0	0	0	1	0	0
	0	0	0	0	1	0
	0	0	0	0	0	1
	h11	h12	0	-b1	0	0
	h21	h22	h23	0	-b2	0
	0	h32	h33	0	0	-b3];

bv = [	0	0	0	h1 / m1	0	0
	0	0	0	1 / m1	0	0
	0	0	0	1 / m1	0	0
	0	0	0	h1 / m1	0	0]';

cv = [	1	0	0	0	0	0
	0	1	0	0	0	0
	0	0	1	0	0	0];

```
dv     = [    0 0 0
              0 0 0
              0 0 0];
```

%***

C.3 Mode frequencies

The file **modes.m** calculates the mode frequencies for all the degrees of freedom of a triple pendulum. The spring matrix components are called from **cit.m** and the input parameters are in turn called from **jbr.m.** (for example)

```
% modes.m

cit;     % input
% longitudinal and tilt matrx
A_LRT      = [   k11    k12    k13    k14    k15    k16
                 k21    k22    k23    k24    k25    k26
                 k31    k32    k33    k34    k35    k36
                 k41    k42    k43    k44    k45    k46
                 k51    k52    k53    k54    k55    k56
                 k61    k62    k63    k64    k65    k66];
% calculation of the freq.
p        = sqrt(abs(eig(A_LRT)));
longtilt          = p/2/pi
%*********************************************************
% sideways and roll matrix
A_TRL      = [   j11    j12    j13    j14    j15    j16
                 j21    j22    j23    j24    j25    j26
                 j31    j32    j33    j34    j35    j36
                 j41    j42    j43    j44    j45    j46
```

```
                    j51    j52    j53    j54    j55    j56
                    j61    j62    j63    j64    j65    j66];
% calculation of the freq.
p        = sqrt(abs(eig(A_TRL)));
sidewaysroll   = p/2/pi
%*********************************************************
% rotational matrix
A_RZ  = [     i11    i12    0
              i21    i22    i23
              0      i32    i33];
% calculation of the freq.
s        = sqrt(abs(eig(A_RZ)));
rotationalmodes       = s/2/pi
%*********************************************************
% vertical matrix
A_Z   = [     h11    h12    0
              h21    h22    h23
              0      h32    h33];
%calculation of the freq.
q        = sqrt(abs(eig(A_Z)));
vertical= q/2/pi()
%*********************************************************
```

C.4 Vertical transfer function

The file **vert.m** calculates the transfer function of a triple pendulum. The spring matrix components are called from **cit.m** and the input parameters are in turn called from **jbr.m.** (for example)

% vert.m.

```
% VERTICAL (Z)
clear all
% name of input file called
jbr;     % T.P.
%ajt;   % T.P. PROTOTYPE
%*****************************************************
% calculation of the freq.
eig(av);
q        = abs(eig(av));
vertical= q/2/pi
%*****************************************************
% calculation of the transfer function
% ** 1,2 or 3 single,double or triple input in the bv matrix
% *   1,2 or 3 single,double or triple output in the cv matrix
%                         **     *
[mag,phase]    = bode(av,bv(:,3),cv(3,:),0,1,w);
```

148

```
mag    = mag/mag(1); %normalises the gain
semilogx(v,20*log10(mag));
axis([1e-0,100,-70,30])
grid
```

C.5 Vertical bode analysis (scz2.m).

The file **scz2.m** calls the ABCD matrix from **cit.m** which in turn calls the input parameters from **jbr.m** (for example). The file adds the local control, outlined in section 5.5, to the pendulum and returns, for example, the closed loop transfer function and the impulse response of the triple pendulum.

% scz2.m

```
%*********************************************************
% vertical (z)
clear all
cit;              % input from cit.m
v        = logspace(-1,2,200);
w        = 2*pi*v
%***************************************************
% calculation of the freq.
eig(av);
q        = abs(eig(av));
vertical= q/2/pi
%***************************************************
% adding the local control
as       = [0];
bs       = [0];
cs       = [0];
ds       = [1];
coils    = 3;
[ac2,bc2,cc2,dc2]      = local(gainzrtrl*coils);
[acv,bcv,ccv,dcv]      = append(as,bs,cs,ds,ac2,bc2,cc2,dc2);
[acv,bcv,ccv,dcv]      = append(acv,bcv,ccv,dcv,as,bs,cs,ds);
[a,b,c,d]        = series(acv,bcv,ccv,dcv,av,bv,cv,dv);
% use this to close the loop (pendulum + control)
[a,b,c,d] = cloop(a,b,c,d,1,-2);
%***************************************************
% transfer function closed loop (vertical)
clf
[mag1,phase1]= bode(a,b,c,d,2,w);
subplot(2,1,1);
loglog(v,mag1(:,1),'r');
axis([min(v),max(v),0.01,100])
grid
subplot(2,1,2);
semilogx(v,phase1(:,1),'r')
axis([min(v),max(v),-180,180])
```

```
title('vert')
grid
pause
clf
%*********************************************
% impulse response vertical (each mass is shown)
t        = linspace(0,10,300);
imp      = impulse(a,b,c,d,1,t);
plot(t,imp(:,1),'r',t,imp(:,2),'b',t,imp(:,3),'w')
grid
%***********************************************************
```

C.6 Rotational bode analysis (scrz2.m).

The file **scrz2.m** calls the ABCD matrix from **cit.m** which in turn calls the input parameters from **jbr.m** (for example). The file adds the local control, outlined in section 5.5, to the pendulum and returns, for example, the closed loop transfer function and the impulse response of the triple pendulum.

% scrz2.m

```
%***********************************************************
% rotational (rz)
clear all
cit;             % input
v        = logspace(-1,2,200);
w        = 2*pi*v;
%***********************************************************
% calculation of the freq.
eig(ar);
s        = abs(eig(ar));
rotationalmodes       = s/2/pi
%***********************************************************
% adding the local control
as       = [0];
bs       = [0];
cs       = [0];
ds       = [1];
coils    = 2;
[ac1,bc1,cc1,dc1]      = local(gainlrz*leverarmrz.^2*coils);
[acr,bcr,ccr,dcr]      = append(ac1,bc1,cc1,dc1,as,bs,cs,ds);
[acr,bcr,ccr,dcr]      = append(as,bs,cs,ds,acr,bcr,ccr,dcr);
[a,b,c,d]       = series(acr,bcr,ccr,dcr,ar,br,cr,dr);
% use this to close the loop (pendulum + control)
[a,b,c,d]       = cloop(a,b,c,d,1,-2);
%***********************************************************
% transfer function
clf
```

```
[mag1,phase1] = bode(a,b,c,d,2,w);
subplot(2,1,1);
loglog(v,mag1(:,1),'r');
axis([min(v),max(v),0.01,100])
grid
subplot(2,1,2);
semilogx(v,phase1(:,1),'r')
axis([min(v),max(v),-180,180])
title('rz')
grid
pause
clf
%*****************************************************
% impulse response fo triple pendulum (each mass is shown)
t       = linspace(0,10,300);
imp     = impulse(a,b,c,d,1,t);
plot(t,imp(:,1),'r',t,imp(:,2),'b',t,imp(:,3),'w')
grid
%*****************************************************
```

C.7   Sideways, t and roll ,rl bode analysis (sctrl2.m).

The file **sctrl2.m** calls the ABCD matrix from **cit.m** which in turn calls the input parameters from **jbr.m** (for example). The file adds the local control, outlined in section 5.5, to the pendulum and returns, for example, the closed loop transfer function and the impulse response of the triple pendulum.

% sctrl2.m.

```
%***********************************************************************
clear all
jbr;
v       = logspace(-1,2,300);
w       = 2*pi*v;
%*********************************************************
% calculation of the freq.
eig(A);
p       = abs(eig(A));
sideroll= p/2/pi
%*********************************************************
% adding the local control
as      = [0];
bs      = [0];
cs      = [0];
ds      = [1];
% 1- roll
```

151

```
coils     = 3;
[ac1,bc1,cc1,dc1]     = local(gainzrtrl*leverarmrl.^2*coils);
% 2 - side
[ac2,bc2,cc2,dc2]     = local(gaint);
 [ac,bc,cc,dc]  = append(as,bs,cs,ds,ac1,bc1,cc1,dc1);
[a,b,c,d]          = append(ac,bc,cc,dc,ac2,bc2,cc2,dc2);
[a,b,c,d]          = append(a,b,c,d,as,bs,cs,ds);
[a,b,c,d]          = append(a,b,c,d,as,bs,cs,ds);
[a,b,c,d]          = series(a,b,c,d,A,B,C,D);
% use this to close loops
ops     = [ 1 2 ];
ips     = [ 2 3 ];
[a,b,c,d]          = cloop(a,b,c,d,ops,-ips);
[a,b,c,d]          = minreal(a,b,c,d);
%****************************************************
% bode analysis – open loop transfer function
clf
[mag,phase]     = bode(a,b,c,d,1,w);
subplot(2,1,1);
loglog(v,mag(:,1),'r', v,mag(:,2),'b',v,mag(:,3),'w',v,mag(:,4),'y',
        v,mag(:,5),'g',v,mag(:,6),'m');
axis([min(v),max(v),1e-4,1e2])
grid
hold
subplot(2,1,2);
semilogx(      v,phase(:,1),'r', v,phase(:,2),'b',v,phase(:,3),'w',v,phase(:,4),'y',
            v,phase(:,5),'g',v,phase(:,6),'m')
axis([min(v),max(v),-540,180])
grid
hold
pause
%****************************************************
% transfer function – closed loop (roll)
clf
[mag1,phase1]= bode(a,b,c,d,2,w);
subplot(2,1,1);
loglog(v,mag1(:,1),'r');
axis([min(v),max(v),0.01,100])
grid
subplot(2,1,2);
semilogx(v,phase1(:,1),'r')
axis([min(v),max(v),-180,180])
title('roll')
grid
pause
%****************************************************
% transfer function – closed loop (sideways)
clf
[mag2,phase2]= bode(a,b,c,d,3,w);
subplot(2,1,1);
```

```
loglog(v,mag2(:,2),'r');
axis([min(v),max(v),-0.01,100])
grid
subplot(2,1,2);
semilogx(v,phase2(:,2),'r')
axis([min(v),max(v),-180,180])
grid
title('side')
pause
%***********************************************
% impulse response
clg
t       = linspace(0,10,300);
imp     = impulse(a,b,c,d,1,t);
plot(   t,imp(:,1),'r',t,imp(:,2),'b',t,imp(:,3),'w',t,imp(:,4),'y',t,imp(:,5),'g',
        t,imp(:,6),'m')
grid
%*******************************************************************
```

C.8   Tilt, rt and longitudinal, l bode analysis (sclrt2.m).

The file **sclrt2.m** calls the ABCD matrix from **cit.m** which in turn calls the input parameters from **jbr.m** (for example). The file adds the local control, outlined in section 5.5, to the pendulum and returns, for example, the closed loop transfer function and the impulse response of the triple pendulum.

% sclrt2.m.

```
%***********************************************************************
clear all
jbr;            % input
v       = logspace(-1,2,500);
w       = 2*pi*v;
%**********************************************************
% calculation of the freq.
eig(A);
p       = abs(eig(A));
longtilt = p/2/pi
%***********************************************************************
% adding the local control
as      = [0];
bs      = [0];
cs = [0];
ds      = [1];
% 1 - tilt
coils   = 2;
[ac1,bc1,cc1,dc1]       = local(gainzrtrl*leverarmrt.^2*coils);
```

```
% 2 - longitudinal
[ac2,bc2,cc2,dc2]      = local(gainlrz*coils);
[ac,bc,cc,dc]   = append(as,bs,cs,ds,ac1,bc1,cc1,dc1);
[a,b,c,d]        = append(ac,bc,cc,dc,ac2,bc2,cc2,dc2);
[a,b,c,d]        = append(a,b,c,d,as,bs,cs,ds);
[a,b,c,d]        = append(a,b,c,d,as,bs,cs,ds);
[a,b,c,d]        = series(a,b,c,d,A,B,C,D);
% use this to close loops
ops    = [ 1 2 ];
ips    = [ 2 3 ];
[a,b,c,d]        = cloop(a,b,c,d,ops,-ips);
[a,b,c,d]        = minreal(a,b,c,d);
%************************************************
% bode analysis open loop transfer function
clf
[mag,phase]    = bode(a,b,c,d,1,w);
subplot(2,1,1);
loglog(        v,mag(:,1),'r', v,mag(:,2),'b',v,mag(:,3),'w',v,mag(:,4),'y',
               v,mag(:,5),'g',v,mag(:,6),'m');
axis([min(v),max(v),1e-4,1e2])
grid
hold
subplot(2,1,2);
semilogx(      v,phase(:,1),'r', v,phase(:,2),'b',v,phase(:,3),'w',v,phase(:,4),'y',
               v,phase(:,5),'g',v,phase(:,6),'m')
axis([min(v),max(v),-540,180])
grid
hold
pause
%************************************************
% transfer function closed loop (tilt)
clf
[mag1,phase1]= bode(a,b,c,d,2,w);
subplot(2,1,1);
loglog(v,mag1(:,1),'r');
grid
subplot(2,1,2);
semilogx(v,phase1(:,1),'r')
axis([min(v),max(v),-180,180])
title('tilt')
grid
pause
%************************************************
% transfer function closed loop (longitudinal)
clf
[mag2,phase2]= bode(a,b,c,d,3,w);
subplot(2,1,1);
loglog(v,mag2(:,2),'r');
grid
subplot(2,1,2);
```

```
semilogx(v,phase2(:,2),'r')
axis([min(v),max(v),-180,180])
grid
title('long')
pause
%************************************************
% shadow sensor noise
clg
loglog(v,3e-10.*mag1(:,6),'m',v,3e-10.*mag2(:,6),'g');
axis([min(v),max(v),1e-22,1e-12])
grid
title('shadow sensor noise with 3e-10m/sqrt(Hz) input')
pause
%************************************************
% coil driver noise
clg
[mag1,phase1]= bode(a,b,c,d,5,w);
loglog(v,0.707.*1e-3.*3e-10.*mag1(:,6),'g');
axis([min(v),max(v),1e-22,1e-12])
title('coil driver noise with 190db/Hz driver and 1 mm rms range')
grid
pause
%************************************************
% impulse response of triple pendulum
t       = linspace(0,10,300);
imp     = impulse(a,b,c,d,1,t);
plot(   t,imp(:,1),'r',t,imp(:,2),'b',t,imp(:,3),'w',t,imp(:,4),'y',t,imp(:,5),'g',
        t,imp(:,6),'m')
grid
%************************************************
```

APPENDIX D

Tutorial

Several examples to aid the use of the triple pendulum model for a triple pendulum outlined in Appendix C and in chapter 5

% EXAMPLE A: - obtain frequencies of GEO 600 triple pendulum.

1. View parameters of triple pendulum in **jbr.m** using an editor (also using Appendix B).
2. Run **modes.m** in MATLAB window to obtain frequencies. The spring matrix components are called from **cit.m**.

% EXAMPLE B: - input own triple pendulum.

1. Input parameters in **jbr.m** and save.

2. Run **modes.m** in MATLAB window to obtain frequencies.

NB: - Can also save input file, **jbr.m**, with a new name BUT would have to also change the line in **cit.m** calling this new input file.

% EXAMPLE C: - using this new triple pendulum to obtain transfer function.

1. Change the name of the input file called in **vert.m**.
2. Run **vert.m**. in MATLAB window.

% EXAMPLE D: - using this new triple pendulum to obtain the: -

- closed loop transfer function bode plots
- root locus and
- impulse response, looking at the different masses.

1. Change the name of the input file called in each of the 4 control files: -

- vertical   - **scz2.m**
- rotation   - **scrz2.m**
- longitudinal + tilt   - **sclrt2.m**
- sideways + roll   - **sctrl2.m**

2. Run each in MATLAB window. (NB: - Press return to move from one plot to the next).

3. It is also possible to obtain the open loop transfer function bode plot by commenting out the "cloop" command, using a "%" at the start of the line in each of the control files outlined above.

% EXAMPLE E: - Allows the input of own controller.

1. In **jbr.m** can change the positioning of the coils on the upper mass by altering the "'leverarms" i.e. the half spacing of the coils for a particular rotational degree of freedom. It is also possible to change the gain setting for the coils. Both of these are outlined in section 5.5

2. Run each of the control files in Example C with this new controller.

APPENDIX E   Centre of Percussion

The purpose of this theoretical work was to investigate the possibility of improved isolation in compound pendulums using the centre of percussion [91].

Compound pendulum

A compound pendulum is a rigid body suspended and free to swing about an axis that does not pass through the centre of mass, see figure (E.1). As outlined below, the transfer function of a compound pendulum taken between the point of suspension and the centre of percussion gives isolation proportional to $\dfrac{1}{\omega^2}$ at high frequencies, whereas the transfer function of a compound pendulum taken between the point of suspension and the centre of mass tends to a constant value at high frequencies [92].
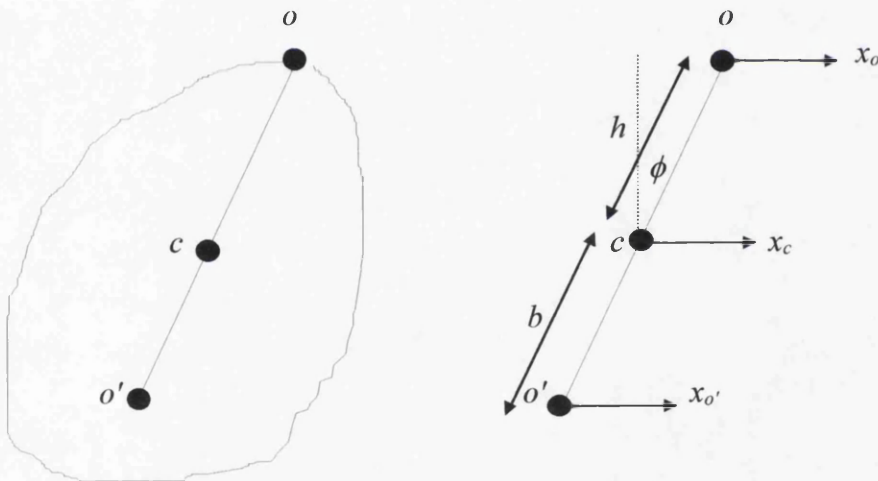

Figure (E.1): - *Compound pendulum.*

In the diagram o is the point of suspension,

        c is the centre of mass,

        o' is an arbitrary point a distance b from c,

        h is the distance between o and c and

        b is the distance between c and o'.

The horizontal transfer function of c with respect to o can be shown to be [93] [92]

$$\frac{x_c}{x_o} = \frac{mgh - I_c\omega^2}{mgh - I_o\omega^2} \tag{E.1}$$

where I_o, the moment of inertia about o, is given by

$$I_o = I_c + mh^2 \tag{E.2}$$

and I_c, the moment of inertia about c, is given by

$$I_c = mr_g^2 \tag{E.3}$$

where r_g is the radius of gyration and m is the mass.

As $\omega \to 0$; $\dfrac{x_c}{x_o} = 1$ and as $\omega \to \infty$; $\dfrac{x_c}{x_o} \to$ constant value, as shown in figure (E.2).

One can also consider the transfer function of o' with respect to o [92]. This is: -

$$\frac{x_{o'}}{x_o} = \frac{mgh - (I_c - mbh)\omega^2}{mgh - I_o\omega^2} \tag{E.4}$$

If b is set to the value $b = \dfrac{I_c}{mh} = \dfrac{r_g^2}{h}$ \hfill (E.5)

on substitution of equation (E.5) into (E.4) we get: -

$$\frac{x_{o'}}{x_o} = \frac{mgh}{mgh - I_o\omega^2} \tag{E.6}$$

As $\omega \to 0$; $\dfrac{x_{o'}}{x_o} = 1$ and as $\omega \to \infty$; $\dfrac{x_{o'}}{x_o} \to \dfrac{mgh}{I_o\omega^2}$.

The point o' is called the centre of oscillation of the pendulum with respect to the point of suspension, o, and it is the point where the compound pendulum transfer function is the same as a single pendulum of length, $l = \dfrac{I_o}{mh}$, as seen in equation (E.6) and shown in figure (E.2). Since the equation $r_g^2 = hb$ is symmetrical in h and b the point o is therefore the centre of oscillation with respect to the point o'. It can be shown that the centre of oscillation is the same as the centre of percussion [91]. The centre of percussion is the point on a rigid body where if the body is struck at this point, no impulse is felt at o. This problem is of interest to a cricketer who is trying to

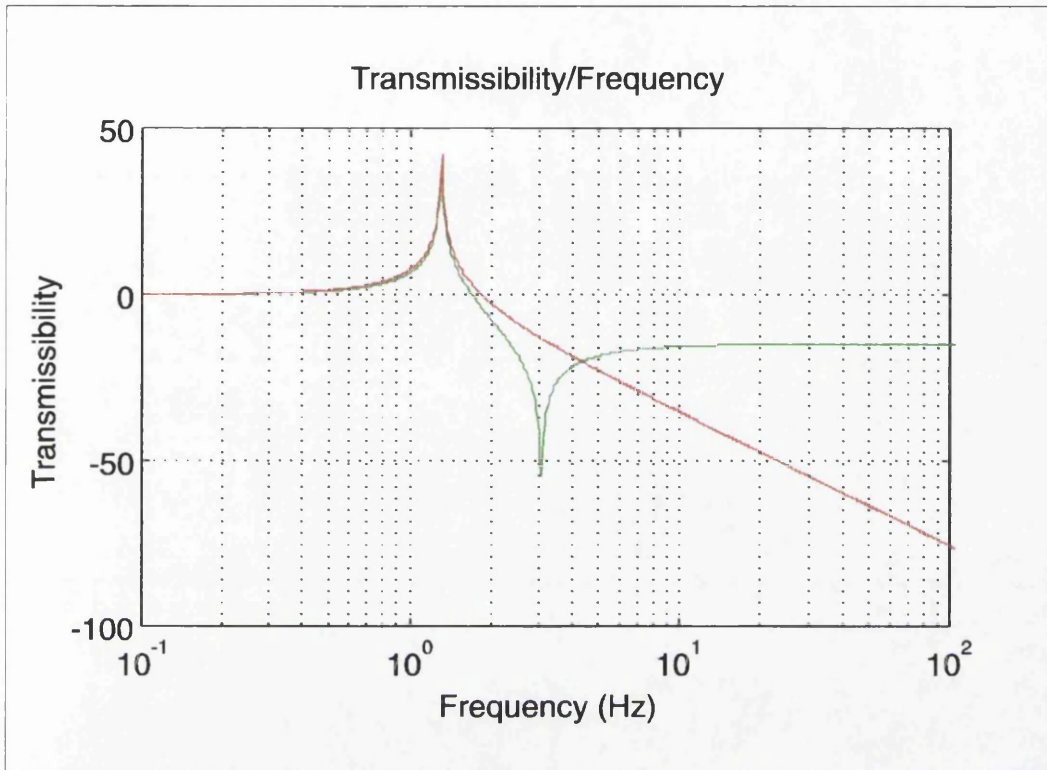hit a ball with his bat. He should hit the ball at the centre of percussion o' relative to his hands at o.

Figure (E.2): - *Transfer function against frequency for the centre of oscillation, $\dfrac{x_{o'}}{x_o}$ (red) and the centre of mass, $\dfrac{x_c}{x_o}$ (green) with respect to the point of suspension.*

Therefore we can conclude that good isolation can in principle be obtained at the centre of oscillation compared to the centre of mass.

In an isolation system there are several opportunities of taking advantage of this improved isolation. Firstly if you consider the test mass mirror as a compound pendulum then in principle an improvement in noise can be obtained by aiming the laser beam at the centre of percussion [92]. In practice if the laser beam is a finite size it is necessary to calculate the average motion over the diameter of the laser beam in order to investigate how much improvement in isolation is obtained. Secondly the argument for a compound pendulum can be applied to a cantilever blade where the restoring torque is provided by the springiness of the blade rather than the force due

to gravity. In this case for a horizontal blade the improved isolation is in the vertical direction. This is of particular interest to us and is discussed in more detail below.

Cantilever blade

Consider the upper cantilever blade, section 6.4, for the GEO 600 main suspension such that the clamp at point **B**, as shown in figure (E.3), is equivalent to the point of suspension. What we are interested in is the position of the centre of percussion.

Now the moment of inertia is $I_c = \frac{m\,l^2}{18}$, assuming a triangular blade where I_c is the moment of inertia in the direction perpendicular to the plane of the blade [94], and from equation (E.3) $I_c = mr_g^2$.

$$\Rightarrow \qquad mr_g^2 = \frac{ml^2}{18} \qquad\qquad\qquad (E.7)$$

For the upper blade the length, $l = 24$ cm

$$\Rightarrow \qquad\qquad r_g^2 = 0.00324 \ \text{m}^2$$

and from (E.5) $\qquad b = \frac{r_g^2}{h} \approx 4.0$ cm, where $h = \frac{l}{3} \sim 8$ cm. Therefore the centre of percussion of the blade is ~ 4.0 cm from the centre of mass, as shown in figure (E.3). One could in principle take advantage of the improved vertical isolation gained by attaching the suspension wire holding the mass below at the centre of percussion rather than at the end of the blade.
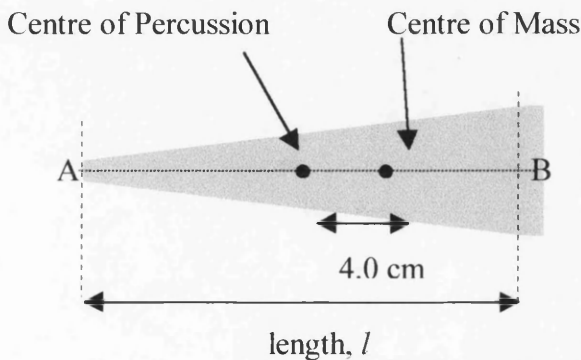

Figure (E.3): - *Schematic of cantilever blade showing centre of mass and centre of percussion.*

Adjusting the position of the centre of percussion

An interesting point to consider is the following. If you have, for example, the cantilever blade with fixed points of attachment at each end and you want to make one point the centre of percussion with respect to the other, how do you add mass to the blade to achieve this?

Consider for simplicity a simple bar that is clamped at the point o. The bar is treated as a compound pendulum and the symbols used are as defined before. Firstly the case of a bar of length, l, and mass, m, is considered, as in figure (E.4a). Secondly the case of extending the bar is considered, as in figure (E.4b) and figure (E.4c).
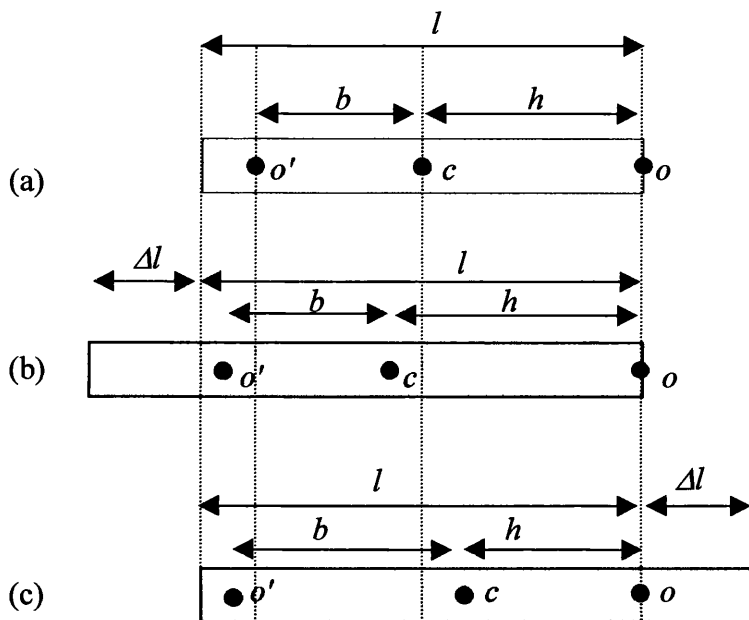
Figure (E.4): - *(a) shows the case of a simple bar, (b) with the bar extended on one side and (c) with the bar extended on the other side.*

(a)   The moment of inertia about c, in figure (E.4a), of a thin bar is: -

$$I_c = \frac{m\,l^2}{12} = mr_g^2 \text{ from equation (E.3) implying } r_g^2 = \frac{l^2}{12} \qquad \text{(E.8)}$$

From equation (E.5) the position of the centre of percussion of a compound pendulum was given by $b = \dfrac{r_g^2}{h}$.

Therefore the position of the centre of percussion of the bar in figure (E.4a) relative to o is given by $h + b$ where $h = \dfrac{l}{2}$ and $b = \dfrac{l^2/12}{l/2} = \dfrac{l}{6}$, on substituting for r_g^2 from equation (E.8). Therefore $b + h = \dfrac{l}{6} + \dfrac{l}{2} = \dfrac{2\,l}{3}$.

(b)   Now consider the case of extending the bar beyond o', as shown in figure (E.4b).

In this case $b = \dfrac{(l + \Delta l)^2/12}{(l + \Delta l)/2} = \dfrac{1}{6}(l + \Delta l)$ and $h = \dfrac{(l + \Delta l)}{2}$.

Therefore $b + h = \dfrac{2\,l}{3} + \dfrac{2\,\Delta\,l}{3}$ and is larger than in example (a).

$\Rightarrow o'$ is further along the bar i.e. further away from o, than in example (a).

(c)   Now consider the case of extending the bar above o, as shown in figure (E.4c).

This time $h = \dfrac{(l + \Delta l)}{2} - \Delta l = \dfrac{(l - \Delta l)}{2}$ and $b = \dfrac{(l + \Delta l)^2/12}{(l - \Delta l)/2} = \dfrac{1}{6}\dfrac{(l + \Delta l)^2}{(l - \Delta l)^2}$.

Therefore $b + h = \dfrac{(l + \Delta l)^2/12}{(l - \Delta l)/2} + \dfrac{(l - \Delta l)}{2}$.

Considering the following examples: -

$\Delta l = \dfrac{l}{2} \Rightarrow b + h = l$. This is larger than in example (a).

$\Delta l = \dfrac{l}{3} \Rightarrow b + h = l$. This is again larger.

This shows that o' is further away from o, than in example (a).

Therefore by the addition of mass either to one side, as in (b), or the other side, as in (c), the centre of percussion moves away from o.

For the case of the upper cantilever blades for GEO 600 it may be easier to add mass at one end rather than the other to adjust the position of centre of percussion and this is an area of possible investigation for improving the isolation.

Accuracy of the position of the centre of percussion

Another question that requires to be addressed is the following. How close to the position of the centre of percussion do you have to be to take advantage of the improved isolation? Figure (E.5) shows the simple transfer function of the cantilever blade, outlined above, for the centre of percussion and 1 mm and 0.1 mm away from the centre of percussion with respect to the point of suspension.

This shows that to obtain the isolation behaviour of a simple pendulum over a reasonable bandwidth, the attachment point has to be very close to the centre of percussion. Therefore careful tuning would have to be carried out to take full advantage of the centre of percussion.
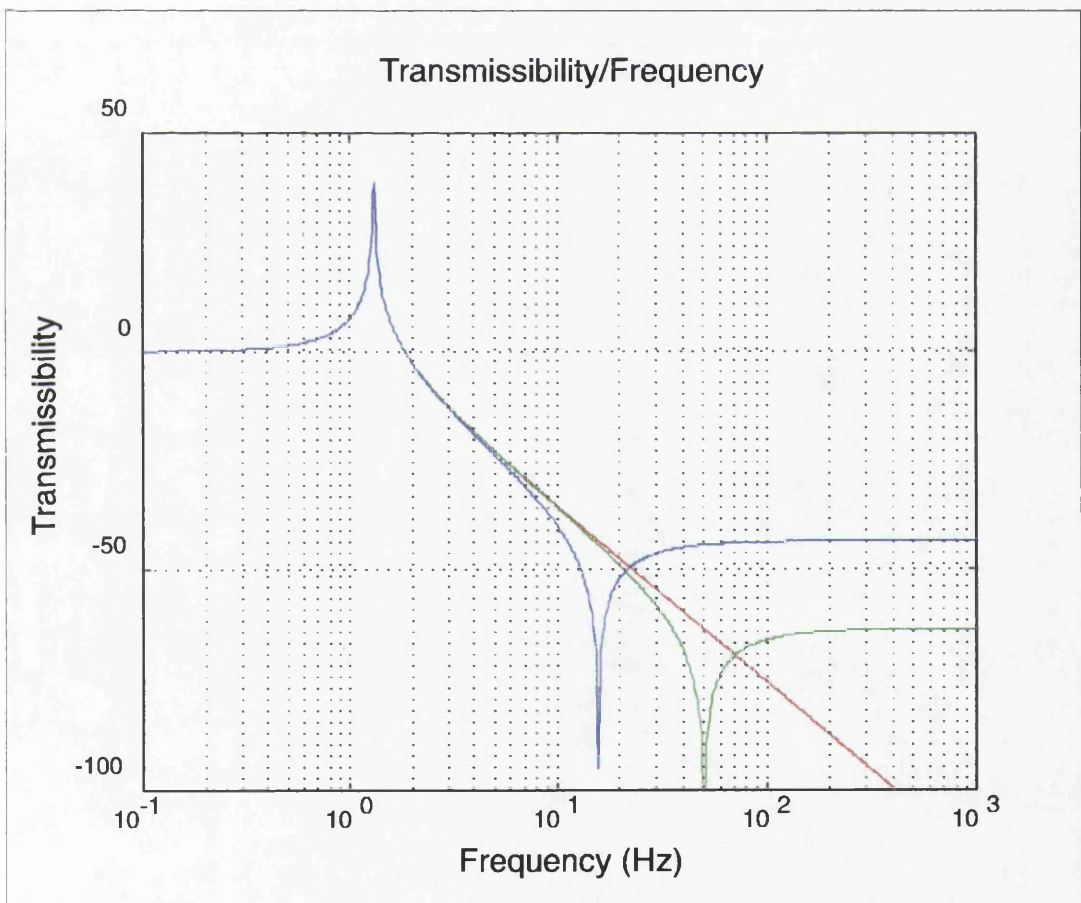

Figure (E.5): - *The graph of the transfer functions of (i) the centre of percussion (red) and (ii and iii) 1 mm and 0.1 mm from the centre of percussion (blue and green) with respect to the point of suspension.*

Bibliography

[1] J. Hough, H. Walther, B.F. Schutz, J. Ehlers, H. Welling, I.F. Corbett, V. Kose, et. al., *Proposal for a Joint German-British Interferometric Gravitational Wave Detector*, Max-Planck-Institut fur Quantenoptik Report 147 and GWD/137/JH(89), (1989).

[2] K. Danzmann et. al., *GEO 600: Proposal for a 600m laser interferometric gravitational wave antenna*, Max-Planck-Institut fur Quantenoptik Report 190, Garching, Germany, (1994).

[3] A. Einstein, *Die Grundlage der Algemeinen Relativitatstheorie*, Annalen der Physik, **49**, (1916), 769.

[4] J. Weber, Phys. Review **117**, (1960), 306.

[5] R.A. Hulse, J.H. Taylor, Astrophys. J., **195** (1975), L51.

[6] J.H. Taylor, Rev. of Mod. Phys., **66** (1994), 711.

[7] S. Bonnanzola, J.A. Marck, Annual Review of Nuclear and Particle Science, **45**, (1994), 655.

[8] B.F. Schutz, *The Detection of Gravitational Waves*, Proceedings of the 1995 Houches School on Astrophysical Sources of Gravitational Radiation, Ed. J.A. Marck, J.P. Lasota, Springer Berlin, (1996).

[9] J.A. Lobo, *Sources of Gravitational Waves*, in General Relativity, Proceedings of the 46th Scottish Universities Summer School in Physics, Aberdeen, Ed. G.S. Hall and J.R. Pulham, (1995), 203.

[10] B.F. Schutz, Nature, **323**, (1986), 310.

[11] V. Kalogera, *Compact Binary Mergers and Accretion-Induced Collapse: Event Rates and Mass and Spin Distributions*, Talk at 3rd Edoardo Amaldi Conference on Gravitational Waves, July 12 - 16, 1999 California Institute of Technology, Pasadena, California, USA.

[12] K.S. Thorne, *Gravitational Waves*, Proceedings of the 1994 Snowmass Summer Study on Particle and Nuclear Astrophysics and Cosmology, Ed. E.W. Kolb, R. Peccei, World Scientific, Singapore, (1995), 18.

[13] R.V. Wagoner, Astrophys. J., **278**, (1984), 345.

[14] L. Bildsten, Astrophys. J., **501**, (1998), L45.

[15] ref. [1], page 18.

[16] http://tmo.jpl.nasa.gov/tmo/progress_report/42-132/132G.pdf

[17] N.A. Robertson, *Detection of Gravitational Waves*, in General Relativity Proceedings of the 46th Scottish Universities Summer School in Physics, Aberdeen, Ed. G.S. Hall, J.R. Pulham, (1995), 223.

[18] G. V. Pallottino, *The Cryogenic Gravitational Wave Antennas Explorer and Nautilus*, Proc. of VIRGO 96, Cascina, World Scientific, (1996), 159.

[19] A. Abramovici, P. Bender, R. Drever, et.al., *Gravitational Waves*, Proceedings of the 1994 Snowmass Summer Study on Particle and Nuclear Astrophysics and Cosmology, Ed. E.W. Kolb, R. Peccei, World Scientific, Singapore, (1995), 398.

[20] http://www.lnf.infn.it/esperimenti/rog/NAUTILUS/current.html

[21] A. De Waard, *MiniGRAIL A small (60cm) Spherical Antenna*, Talk at 3rd Edoardo Amaldi Conference on Gravitational Waves, July 12 - 16, 1999 California Institute of Technology, Pasadena, California, USA.

[22] R.L. Forward, Phys. Rev. D, **17**, (1978), 379.

[23] R. Weiss, M.I.T. Quarterly Progress Report No. 105, (1972).

[24] P.R. Saulson, Fundamentals of Interferometric Gravitational Wave Detectors, World Scientific, Singapore, (1994).

[25] W. Winkler, *A Michelson Interferometer Using Delay Lines* in *The Detection of Gravitiational Waves* Ed. D.G. Blair, Cambridge University Press, Cambridge, (1991) 269.

[26] D. Shoemaker, R. Schilling, L. Schnupp, W. Winkler, K. Maischberger, A. Rudiger, Phys. Rev. D., **38**, (1988), 423.

[27] R.W.P. Drever, G.M. Ford, J. Hough, I.M. Kerr, A.J. Munley, J.R. Pugh, N.A. Robertson, H. Ward, *A Gravity-Wave Detector Using Optical Cavity Sensing*, Proceedings of the 9th International Conference on General Relativity and Gravitation, Jena 1980, Ed. E. Schmutzer, VEB Deutscher Verlag der Wissenschaften, Berlin, (1983), 306.

[28] D. Sigg, N. Mavalvala, J. Giaime, P. Fritschel, D. Shoemaker, Applied Optics, **37**. (1998), 5687.

[29] D.I. Robertson, E. Morrison, J. Hough, S. Killbourn, B.J. Meers, G.P. Newton, N.A. Robertson, K.A. Strain, H.Ward, *The Glasgow 10m prototype laser interferometric gravitational wave detector*, Rev. Sci. Instrum., **66**, (9), (1995), 4447.

[30] M.M. Casey, Ph.D. Thesis, University of Glasgow, (1999).

[31] R L Savage Jr, *Status of the LIGO 40-m Interferome*ter, Proceedings of the 7th Marcel Grossman Meeting Stanford, USA, Ed. R. Jantzen, G. MacKeiser, World Scientific Signapore, (1996), 1381.

[32] B.C. Barish in Gravitational Wave Detection, Ed. K. Tsubono, M.-K. Fujimto, and K. Kurodo, Universal Academy Press, Inc, Tokyo, (1997), 155.

[33] A. Brillet, B. Caron, A. Dominjon, C. Drezen, R. Flaminio, X. Grave, F. Marion, L. Massonet, C. Mehemel, R. Morand, B. Mours, V. Sannibale, M. Yvert, D. Babusci, S. Bellucci, S. Candusso, G Giordano, G. Matone, J.-M. Mackowski, L. Pinard, C. Boccara, P. Gleizes, V. Loriette, J.-P. Roger, P.G. Pelfer, R. Stanga, F. Barone, E. Calloni, L. Di Fiore, M. Flagiello, F. Garufi, A. Grado, M. Longo, M. Lops, L. Milano, S. Marono, S. Solimeno, M. Barsgulia, B. Bhawal, F. Bondu, V. Brisson, F. Cavalier, M. Davier, H. Heitmann, P.

Hello, P. Heusse, J.-M. Innocent, L. Latrach, F. Le Diberder, C. Nary Man, P. Marin, M. Pham-Tu, M. Taubman, E. Tournier, J.-Y. Vinet, G. Cagnoli, L. Gammaitoni, J. Kovalik, F. Machesoni, M. Punturo, M. Breccaria, M. Bernardini, S. Braccini, C. Bradaschia, C. Casciano, G. Cella, A. Ciampa, E. Cuoco, G. Curci, R. De Salvo, R. Del Fabbro, A. Di Virgilio, D. Enard, I. Ferrante, F. Fidecaro, A. Gaddi, A. Giazotto, G. Gorini, P. La Penna, G. Losurdo, S. Mancini, H.B. Pan, A. Pasqualetti, D. Passuello, R. Poggiani, P. Popolizio, F. Raffaelli, A. Vicere, Z. Zhang, F. Bronzini, V. Ferrari, E. Majorana, P. Puppo, P. Rapagnani, F. Ricci, L. Holloway in Gravitational Wave Detection, Ed. K. Tsubono, M.-K. Fujimto, and K. Kurodo, Universal Academy Press, Inc, Tokyo, (1997), 163.

[34] K. Tsubono and the TAMA collaboration, in Gravitational Wave Detection, eds. K. Tsubono, M.-K. Fujimto, and K. Kurodo, Universal Academy Press, Inc, Tokyo, (1997), 183.

[35] R.-T. Takahashi, *TAMA300 project: status*, Talk at Rencontres de Moriond Gravitational Waves and Experimental Gravity Les Arcs 1800, France, January 23-30 (1999).

[36] D. G. Blair, M. Notcutt, L. Ju, M. E. Tobar, Y. M. Yang, E. Wang, C. Taylor, J. Winterflood, J. F. Lui, M. Taniwaki, C. N. Zhao, D. McClelland, C. Harb, T.C. Ralph, H.-A. Bachor, J. Sandeman, D. Mudge, D. Ottaway, M. W. Hamilton, J. Munch and P. J. Veitch, in Gravitational Wave Detection, Ed. K. Tsubono, M.-K. Fujimto, and K. Kurodo, Universal Academy Press, Inc, Tokyo, (1997), 75.

[37] K. Danzman and the LISA Study team, in Gravitational Wave Detection, Ed. K. Tsubono, M.-K. Fujimto, and K. Kurodo, Universal Academy Press, Inc, Tokyo, (1997), 111.

[38] K. Danzmann, A. Rudiger, R. Schilling, W. Winkler, J. Hough, *et. al.*, Max-Planck-Institut für Quatenoptik Report MPQ 177, (1993).

[39] ref. [1] page 25.

[40] W. A. Edelstein, J. Hough, J.R. Pugh, W. Martin, J. Phys. E: Scientific Instruments, **11**, (1978), 710.

[41] N. A. Robertson, in Gravitation and Relativity: At the Turn of the Millennium Plenary lecture in Proceedings of GR-15 Conference, IUCAA, Pune India, December 1997, Ed. N. Dadhich and J. Narlikar, (1998), 199.

[42] M. Pickenpack, B. Willke, Private Communication, (1997).

[43] P. R. Saulson, Phys. Rev. D, **30**, (1984), 732.

[44] R. Spero, Science Underground, Proceedings of the Los Alamos Conf. 1982, Ed. M.M. Nieto et al., AIP, New York, (1983).

[45] J. Hough, R. Hutchins, J. E. Logan, A. McLaren, M. Plissi, N.A. Robertson, S. Rowan, K. A. Strain, S. M. Twyford, *Developments in isolation, suspension and thermal noise issues for GEO 600*, Proceedings of the VIRGO 96, Cascina, World Scientific, (1996), 124.

[46] J. Hough, G. P. Newton, N. A. Robertson, H. Ward, M. Plissi, D. Robertson, S. Rowan, K. D. Skeldon, K. A. Strain, M. Casey, P. McNamara, C. Torrie, S. M. Twyford, *et al, GEO 600: current status and some aspects of the design*, in Gravitational Wave Detection, Proceedings of TAMA Workshop, Saitama, Japan, Ed. K. Tsubono, M.-K.Fujimoto, K. Kuroda, Universal Academy Press, Tokyo, Japan, (1997), 175.

[47] K. D. Skeldon, K. A. Strain, A. I. Grant, J. Hough, Rev. Sci. Instrum., **67**, (1996), 2443.

[48] R.W.P. Drever, *Interferometric Detectors for Gravitational Radiation*, in Gravitational Radiation, Ed. N. Dereulle, T. Piran, North Holland Publishing Company, (1983), 331.

[49] B. J. Meers, Phys. Rev. D., **38**, (1998), pp.2317-2326.

[50] S. Rowan, S. M. Twyford, R. Hutchins, J. Kovalik, J. E. Logan, A. C. McLaren, N. A. Robertson, and J. Hough, Phys. lett. A, **233**, (1997), 303.

[51] S. Rowan, R. Hutchins, A. C. McLaren, N. A. Robertson, S. M. Twyford and J. Hough, Phys. Lett. A, **227**, (1997), 153.

[52] S. Rowan, *GEO 600 Specifications Thermal Noise*, Proccedings of the 9th GEO 600 Workshop, Glasgow, September 18-21, (1998).

[53] V. B. Braginskii, V. P. Mitrofanov, and S. P. Vyatchanin, Rev. Sci. Instrum. **64**, (12), (1994), 3771.

[54] J. Kovalik and P. R. Saulson, Rev. Sci. Instrum. **64**, (1993), 2942.

[55] S. Rowan and G. Cagnoli, Private Communication (1999).

[56] S. Rowan, S. M. Twyford, J. Hough, D.-H. Gwo and R. Route, *Mechanical losses associated with the technique of hydroxide-catalysis bonding of fused silica*, Phys. Lett. A, **246**, (1998), 471.

[57] K. Tsubono, A. Araya, K. Kawabe, S. Moriwaki and N. Mio, *Triple-pendulum vibration isolation system for a laser interferometer*, Rev. Sci. Instrum. **64** (8), (1993), 2237.

[58] M. V. Plissi, Private Communication, (1999).

[59] S. D. Killbourn, Ph.D. thesis University of Glasgow (1998).

[60] M. Husman, C. Torrie *et al*, *Modelling of the GEO 600 triple pendulum*, in preparation.

[61] C. Torrie, G. Cagnoli, J. Hough, M. Husman, S. McIntosh, D. Palmer, M. Plissi, N. Robertson, S. Rowan, P. Sneddon, K. A. Strain, H. Ward, *Suspension System for the Main Optics for GEO 600*, Proccedings of the Rencontres de Moriond in Gravitational Waves and Experimental Gravity, Les Arcs 1800, France, (1999), in press.

[62] K. A. Strain, Private Communication, (1999).

[63] A. Brillet for the VIRGO collaboration, *VIRGO – Status Report*, Proceedings of the 2nd Edoardo Amaldi Conference on Gravitational Wave Experiments,

CERN, Geneva, eds. E. Coccia, G. Veneziano, G. Pizzella, World Scientific, (1998), 86.

[64] S. Braccini C. Bradaschina, R. Del Fabbro, A. Di Virgilio, I. Ferrante, F. Fidecaro, R. Flaminio, A. Gennai, A. Giassi, A. Giazotto, G. Gorini, G. Losurdo, F. Palla, A. Pasqualetti, D. Passuello, R. Poggiani, G. Torelli and Z. Zhang, *Seismic vibrations: mechanical filters for the gravitational wave detector Virgo*, Rev. Sci. Intrum., **67**, (1996), 2899.

[65] S. Braccini, C. Bradaschina, M. Cobal, R. Del Fabbro, A. Di Virgilio, R. Flaminio, A. Giazotto, H. Kautzky, M. Morganti and D. Passuello, *An improvement in the VIRGO Super Attenuator for interferometric detection of gravitational waves: The use of a magnetic antispring*, Rev. Sci. Intrum., **64**, (2), (1993), 310.

[66] D. Tatsumi, M. A Barton, T. Uchiyama and K. Kuroda, Rev Sci. Instrum, **70**, (2), (1999), 1561.

[67] J. Winterflood and G. Blair, Phys. lett. A, **243**, (1998), 1.

[68] R.W.P. Drever, in Gravitational Wave Detection, Ed. K.Tsubono, M.-K Fujimoto and K. Kurodo, Universal Academy Press, Inc, Tokyo, (1997), 299.

[69] D. Newell, S. Richman, P. G. Nelson, R. T. Stebbins, P. L. Bender and J. Faller, *An ultra-low-noise, low-frequency, six degrees of freedom active vibration isolator*, Rev. Sci. Intrum., **68**, (1997), 3211.

[70] M. Plissi, K. Strain, C. I. Torrie, N. Robertson, S. Rowan, S. Twyford, H. Ward, K. Skeldon, J. Hough, *Aspects of the suspension system for GEO 600*, Rev. Sci. Instrum. **69**, (1998), 3055.

[71] MATLAB for Windows, copyright 1984-1994, The Mathworks Inc. version 4.2b (1994).

[72] I-DEAS Structural Dynamics Research Corporation, Milford, Ohio, (1994).

[73] I-DEAS Student Guide Structural Dynamics Research Corporation, Milford, Ohio, (1994).

[74] K. A. Strain, GEO 600 Internal Report, (1998).

[75] N. W. McLachlan, Theory of Vibrations, New York (1951), 109.

[76] D. A. Low, Mechanical Engineering Pocket Handbook, Longmans, (1942), 212.

[77] P. Aufmuth, Private Communication, (1998).

[78] D. DeBra, Private Communication, (1997).

[79] C. F. Beards, Structural Vibration Analysis, Ellis Horwood series in Eng. Science, Ed. Ellis Horwood, (1983), 103.

[80] J. T. Broch, Mechanical Vibration and Shock Measurements, Bruel & Kjaer, Ed. (1972), 166.

[81] D. Palmer, Private Communication, (1998).

[82] M. E. Husman, Ph.D Thesis, University of Glasgow, (in preparation).

[83] www.goodfellow.com, properties of steel wire AISI-302.

[84] N. S. Nise, Control Systems Engineering, Ed. Benjamin Cummings, (1995), 124.

[85] K. A. Strain, GEO 600 Local Control Summary, Internal report, (1998).

[86] M. Plissi, C. I. Torrie, M. E. Husman, K. Strain, N. Robertson, H. Ward, and J. Hough, *GEO 600 Triple Pendulum Suspension System: Seismic Isolation and Control*, in preparation.

[87] R. Poggiani, Private Communication, (1997).

[88] G. Cella, A. Viceré, *Super Attenuator vertical performance beyond the low frequency range*, VIRGO internal report – VIR-NOT-PIS-1390-91, (1997).

[89] S. Braccini, *Design of the superattenuators for the VIRGO construction*, VIRGO internal report – VIR-TRE-PIS-4600-134, (1997).

[90] K. A. Strain, *Isolation, control and design aspects of the adaptation of a GEO suspension design to LIGO*, Internal Report, (1999).

[91] K. R. Symon, *Mechanics*, 3rd edition 5th printing, Ed. Addison-Wesley, (1978), 215.

[92] L. Ju, D. G. Blair, *Compound Pendulum Test Mass Systems for Laser Interferometer Gravitational Wave Detectors*, Measurement Science and Technology, Vol. 5, No. 9, (1994), 1053.

[93] N. A. Robertson and J. Hough, Private Communication, (1993).

[94] M. V. Plissi, Private Communication, (1999).